The Pennsylvania State University

The Graduate School

Department of Electrical Engineering

MODELING AND CONTROL OF A HIGH-SPEED SOLID-ROTOR SYNCHRONOUS RELUCTANCE FLYWHEEL MOTOR/GENERATOR

A Thesis in

Electrical Engineering

by

Jae-Do Park

Submitted in Partial Fulfillment
of the Requirements
for the Degree of

Doctor of Philosophy

May 2007

The thesis of Jae-Do Park was reviewed and approved* by the following:

Heath F. Hofmann
Associate Professor of Electrical Engineering
Thesis Adviser
Chair of Committee

Kwang Y. Lee
Professor of Electrical Engineering

Jeffrey S. Mayer
Associate Professor of Electrical Engineering

Charles E. Bakis
Professor of Engineering Science and Mechanics

W. Kenneth Jenkins
Professor of Electrical Engineering
Head of the Department of Electrical Engineering

*Signatures on file in the Graduate School.

Abstract

This thesis presents a control system for a high-speed solid-rotor synchronous reluctance flywheel motor/generator. The objective of this research is to derive a model for a solid-rotor synchronous reluctance machine and provide a control scheme based on the model which has stable performance at high speed. The control system should be robust with respect to parameter deviation caused by phenomena such as nonlinear magnetics, rotor temperature variation, and inaccurate measurement. This project also includes the development of an LC filter design to improve the thermal performance of the system.

A dynamic model for a synchronous reluctance machine with a conducting rotor has been developed and an open-loop current regulator for high-speed operation has been designed based upon this model. The machine dynamic model is similar to an induction machine model, yet includes a magnetic saliency of the rotor. The model is then used to calculate command voltages for a desired current in an open-loop current regulator. Techniques for parameter extraction and discrete-time models for digital implementation are presented. Experimental results consisting of a 120kW discharge of a flywheel energy storage system validates the performance of the controller.

The feedforward controller includes machine parameters, and the performance inherently relies on the correctness of these values. However, inductance and resistance parameters will vary due to flux saturation and temperature, respectively. Although a feedforward control scheme is simple, fast and effective, a direct influence which deteriorates control performance

can be seen on the controller's output if the parameters are varied. Hence, a feedback compensation method has been investigated to handle the possible deviation of the parameters, and to improve the feedforward controller's robustness. A systematic approach to designing a feedback compensator for the feedforward controller is presented. Also, a stability analysis for the feedback-compensated system has been performed. Improved current tracking performance can be seen in the experimental results.

The flux-linkage/current relationships of the machine are one of the major nonlinearities to be handled in a machine controller. A more precise modeling of nonlinear magnetics becomes essential for control purposes and for understanding the limitations imposed by them. The feedforward controller can handle more diverse operating conditions by incorporating a better model of the machine dynamics. Therefore, a more accurate model to represent the nonlinear magnetics for the feedforward controller has been developed. The performance improvement by the modified model has been shown through the experimental results.

Although synchronous reluctance machines with solid rotor construction have advantages in certain high-speed applications such as flywheel energy storage systems, the solid rotor allows the flow of eddy currents, which results in heat generation. A three-phase LC filter can reduce rotor losses due to the switching harmonics. The design and control of a high-speed synchronous reluctance drive with a three-phase LC filter has been investigated. A two-phase dynamic model of the drive which incorporates the LC filter dynamics is presented. The model is used to predict rotor losses due to switching harmonics generated by the three-phase inverter using phasor analysis. A feedforward current regulator is utilized, which is modified to include the effects of the LC filter. Experimental results validate the proposed approach.

Table of Contents

List of Tables

List of Figures

Nomenclature

$[L_r]$ Rotor inductance matrix in rotor reference frame

$[L_s]$ Stator inductance matrix in rotor reference frame

$[M]$ Mutual inductance matrix in rotor reference frame

$[R_r]$ Rotor resistance matrix in rotor reference frame

$\Delta\vec{\lambda}_a^r$ Flux linkage estimation error vector in rotor reference frame

$\Delta\vec{i}_s^r$ Current error vector

$\Delta\vec{v}_s^r$ Voltage command error vector in rotor reference frame

$\mathbf{I}$ Identity matrix $\begin{bmatrix} 1 & 0 \\ 0 & 1 \end{bmatrix}$

$\mathbf{J}$ Rotation matrix $\begin{bmatrix} 0 & -1 \\ 1 & 0 \end{bmatrix}$

ω_{re} Electrical rotor angular velocity

ω_r Mechanical rotor angular velocity

$\mathbf{A}$ Synchronous reluctance machine's full-order system matrix

$\mathbf{L}_r\left(\theta_{re}\right)$ Rotor inductance matrix in stator reference frame

$\mathbf{L}_s\left(\theta_{re}\right)$ Stator inductance matrix in stator reference frame

$\mathbf{M}(\theta_{re})$ Mutual inductance matrix in stator reference frame

θ_{re} Electrical rotor position

$\vec{\bar{x}}, \vec{\bar{X}}$ Complex vector

$\vec{\lambda}_r^r$ Rotor flux linkage vector in rotor reference frame

$\vec{\lambda}_s^r$ Stator flux linkage vector in rotor reference frame

$\vec{\lambda}_r^s$ Rotor flux linkage vector in stator reference frame

$\vec{\lambda}_s^s$ Stator flux linkage vector in stator reference frame

$\vec{\bar{i}}_s^r$ Stator current command vector in rotor reference frame

$\vec{\bar{i}}_s^s$ Stator current command vector in stator reference frame

$\vec{\bar{v}}_s^s$ Stator voltage command vector in stator reference frame

$\vec{\bar{v}}_s^r$ Stator voltage command vector in rotor reference frame

$\vec{i}_i^r$ Inductor current vector in rotor reference frame

$\vec{i}_r^r$ Rotor current vector in rotor reference frame

$\vec{i}_s^r$ Stator current vector in rotor reference frame

$\vec{i}_r^s$ Rotor current vector in stator reference frame

$\vec{i}_s^s$ Stator current vector in stator reference frame

$\vec{v}_s^s$ Stator voltage vector in stator reference frame

$\vec{v}_\ell^r$ Inductor voltage vector in rotor reference frame

$\vec{v}_c^r$	Capacitor voltage vector in rotor reference frame
$\vec{v}_i^r$	Inverter output voltage vector in rotor reference frame
$\vec{v}_s^r$	Stator voltage vector in rotor reference frame
$\vec{x}$	Machine state vector
C_f	Filter capacitance
i_{cx}	Three-phase filter capacitor current, *x=a,b,c*
i_{ix}	Three-phase inverter output current, *x=a,b,c*
i_{spk}	Peak stator current command in stator reference frame
i_{sx}	Three-phase machine stator current, *x=a,b,c*
K_i	Integral gain in feedback compensator
K_p	Proportional gain in feedback compensator
L_f	Filter inductance
$L_{\ell s}$	Stator leakage inductance
P	Pole number of the machine
R_s	Stator resistance
t_d	Dead or blanking time
T_s	Inverter switching period
V_{bus}	DC bus voltage

v_{cx} Three-phase filter capacitor voltage, *x=a,b,c*

v_{ix} Three-phase inverter output voltage, *x=a,b,c*

Acknowledgments

It is delightful to recall the times at Penn State, an adventurous chapter of my life. Woven with challenges, endeavors, bitters, and sweets, it has been really enjoyable and fruitful. I give my sincere thanks to God for this rich blessing bestowed upon me, I would never be grateful enough. I would like to thank my advisor, Heath, for the great opportunities and helpful advice he gave me. It has been a pleasure working with him. I would also like to thank Claude Kalev of Pentadyne Power Corporation for giving me a job and supporting my research. For their heartfelt prayers and encouragements, I appreciate my parents, my parents-in-law, all of my extended family in Korea, and friends in State College, Los Angeles, and Korea. Thanks to my committee for their careful review of my thesis. Finally, a special thanks goes to my wife, HyunJung, and my daughters, JiWoo and JiYoon, for tolerating their always-busy husband/dad and yielding him to his work. None of this work would have been possible without their love and support.

I can do everything through him who gives me strength.
Philippians 4:13

And as in the Olympic Games it is not the most beautiful and the strongest that are crowned but those who compete (for it is some of these that are victorious), so those who act win, and rightly win, the noble and good things in life. Their life is also in itself pleasant.
Nicomachean Ethics, Aristotle

I did not know. I was fully aware of what would be destroyed. I did not know what would be built out of the ruins. No one can know that with any degree of certainty, I thought. The old world is tangible, solid, we live in it and are struggling with it every moment-it exists. The world of the future is not yet born, it is elusive, fluid, made of the light from which dreams are woven; it is a cloud buffered by violent winds-love, hate, imagination, luck, God.
Zorba the Greek, Nikos Kazantzakis

To My Other Half, HyunJung

Chapter 1

Introduction

1.1 Energy Storage Systems

Electrical energy is very flexible and easy to convert to other forms of energy. With the aid of various conversion devices, it has been utilized almost everywhere in human society. Along with its popularity, the quality of electric power has become an important issue. Among many events on electric power grids that can damage or disrupt sensitive loads, voltage disturbances such as interruptions and sags are one of the most serious concerns. Even a very short period of interruption or sag can cause enormous damage in facilities such as continuous process plants, data centers, and hospitals.

Uninterruptible power supply (UPS) systems have been utilized for mitigating these voltage disturbances. UPS takes its power from the supply and charges its energy storage device during normal operation. For an interruption or a sag, the UPS controls the voltage and supports the load using its stored energy. Typically, UPS systems are required to support the full load power for about 15 minutes, which is determined by the historical time requirement for the systems being protected to come to an orderly shutdown for an extended period of power outage [1].

The main energy storage device for UPS systems has historically been lead-acid batteries. Although batteries have disadvantages such as weight and high costs, they have been used because of their high degree of modularity, low standby losses, and wide-spread availability. However, it has been reported that the vast majority of power sags are less than 5 seconds [1, 2].

This creates a great interest to find alternatives that provide power for this short time interval, as lead-acid batteries are not cost-effective for applications that require less than one minute of high-power storage [2]. Furthermore, lead acid batteries have environmental problems due to their toxic materials.

A number of storage methods have been investigated recently as alternatives to lead-acid batteries. Storage devices such as superconducting coils, supercapacitors, and flywheels have been taken into consideration.

1.1.1 Superconducting Coils

A superconductive electromagnetic energy storage (SMES) system stores energy in a magnetic field generated by current flowing in a superconducting wire. Once the superconducting coil is charged, the current will not decay and the magnetic energy can be stored indefinitely. A common design of a SMES system would consist of a coil of superconducting wire buried underground, with power conditioning equipment connecting the coil to the electricity distribution grid. Although there is no reason why SMES could not be used on a very small scale in place of conventional batteries in principle, in practice the relatively low energy density, exacting cryogenic cooling requirements, and high cost mean that near-term applications are likely to be limited to power grid applications.

1.1.2 Supercapacitors

Capacitors store electricity as it is without requiring any conversion, whereas batteries store electricity by converting it to chemical energy. Supercapacitors whose energy capacity is very large have been developed, such as electric double layer capacitors (EDLC). There are a

few different types of electrode materials suitable for the supercapacitor, but EDLC is the least costly to manufacture and is the most common. It stores the energy in the double layer formed near a carbon electrode surface. However, supercapacitors are still expensive due to current low volume manufacturing, and their energy density is low [2].

1.1.3 Flywheels

Flywheels have been utilized for thousands of years to store energy. Flywheels store energy in a simple kinetic form. From the potter's wheel to internal combustion engines, the flywheel is used to smooth mechanical rotations. Energy is stored by causing a disk or rotor to spin on its axis. The stored kinetic energy is proportional to the flywheel's moment of inertia and the square of its rotational speed. Thus, a more massive flywheel or a higher speed flywheel is more desirable to increase the storage capacity. A cylindrical flywheel has a number of distinct advantages: it maximizes energy per unit mass, keeps critical resonance modes outside the normal operating frequencies, and provides ample space [3].

Advances in power electronics, magnetic bearings and flywheel materials have resulted in flywheel energy storage systems that can be used as a substitute or supplement for lead-acid batteries in UPS systems. Flywheel energy storage systems can be more reliable than batteries, so applicability is mostly an issue of cost-effectiveness. Batteries will usually have a lower initial cost than flywheels, but suffer from a significantly shorter lifetime and higher operation and maintenance expenses. Thus, flywheels will look especially attractive in operating environments that are detrimental to battery life, such as frequent cycling stemming from main power supply problems and high operating temperatures associated with non-air-conditioned space. Flywheels can have a much higher power density than batteries, typically by a factor of 5 to 10 [1].

High-power flywheels provide backup power for periods in seconds, which is typically about 15 seconds [1]. This is enough time to allow the flywheel to handle the majority of power disruptions that last for 5 seconds or less and still have time to cover slightly longer outages until a backup system can cover the full load. However, a flywheel alone will not provide backup power for a period long enough to allow an orderly process shutdown in most cases. Therefore, flywheels are usually used in conjunction with batteries or a fuel-driven generator.

Flywheels-and-batteries configuration can benefit the performance of the UPS system and the battery life. Due to flywheel-based energy storage's faster response time than batteries, "whiplash" effect associated with battery discharge can be mitigated [4]. This improves the battery reliability and preserves the battery capacity for a longer disturbances. Also, flywheels can reduce the number of short charge/discharge cycles of the batteries, which greatly extends the life of the batteries.

Flywheels can be classified by their rotational speed. Generally, flywheel systems fall into one of two categories: low- or high-speed. The former operate at thousands of rpm, while the latter runs at tens or hundreds of thousands of rpm. As mentioned above, doubling the speed quadruples the stored energy, so increasing speed significantly increases the energy density of a flywheel. However, the design procedure for high-speed flywheel systems is much more complex than low-speed systems. While low-speed flywheels are usually made from steel, high-speed flywheels typically use carbon- or carbon- and fiberglass-composite materials that will withstand the stresses associated with higher rotational speed. Higher speed also creates greater concern with friction losses from bearings and air drag. As a result, high-speed flywheels universally employ magnetic bearings and vacuum enclosures to reduce or eliminate these two sources of friction. Magnetic bearings allow the flywheel to levitate, essentially eliminating friction losses

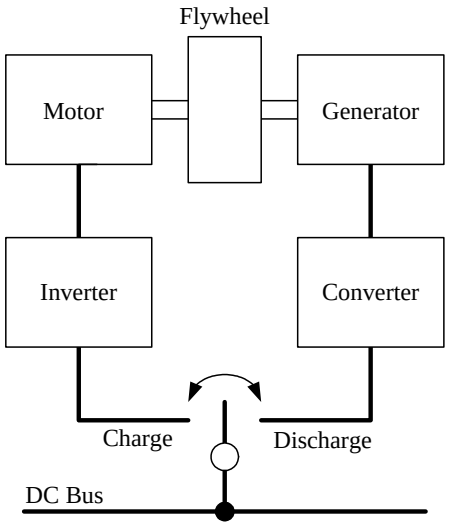

Fig. 1.1. Conceptual diagram of flywheel motor/generator system

associated with conventional bearings. While some low-speed flywheels use only conventional mechanical bearings, most flywheels use a combination of the two bearing types. Vacuums are also employed in some low-speed flywheels [1].

A conceptual diagram of a flywheel system to support a DC bus, which uses a separate motor and generator, is shown in Fig. 1.1. If a machine can operate both as motor and generator, the system will become much more simplified and compact.

1.2 Flywheel Motor/Generator System

Important design considerations for a motor/generator for flywheel systems for UPS applications are as follows;

- High power capacity (> 100 kW),
- High power density,

- Negligible spinning loss,
- High reliability,
- High efficiency,
- Cost effectiveness, and
- Low rotor loss.

To meet the above requirements, several machine types have been explored: permanent magnet (PM) machines, synchronous homopolar machines, Rice-Lundell alternators, switched and synchronous reluctance machines. Induction machines are ruled out because of generally poor power factor and high rotor loss, even though they can have a simple and rugged rotor structure. Among these disadvantages, rotor loss could be the most important factor to take into consideration when it comes to a high-speed flywheel system. Generally high-speed flywheels levitate in a vacuum enclosure, thus black-body radiation is the only way to remove heat in the rotor. As well as decreasing efficiency, rotor losses could make the system inoperable if the rotor temperature becomes too high.

1.2.1 Permanent Magnet Machines

Permanent magnet, or PM machines are one of the popular choices for a flywheel motor/generator [5–8]. PM machines are capable of having significantly lower rotor losses than other non-PM machines, due to no loss related with machine excitation. Their high power factor, efficiency and high power density are other advantages. However, high-power rare earth magnets are costly and the magnets in the rotor may be demagnetized, rendering the motor/generator

unusable, if there is excessive armature reaction or they are overheated [9, 10]. The mechanical structure of permanent magnets is relatively weak for high-speed operation. If it is not an ironless design, PM machines have the inherent disadvantage of spinning losses. However, an ironless stator lowers the torque density and requires significant PM material with very high coercive forces, which increases cost and complicates structural design [11].

The Halbach magnet machine has been extensively studied [12, 13] and investigated for electro-mechanical battery applications [6, 8]. This type of machine has an inherently sinusoidal airgap field and back-EMF. Hence, low harmonic distortion can be achieved and cogging torque is negligible. However, low Nm/kg and high cost per kW are disadvantages of this design [6].

1.2.2 Synchronous Homopolar Machine

Although not widely used in practice, synchronous homopolar machines have been researched for a variety of applications [14–16]. The means of generating the rotor's magnetic field is the difference between this type and other synchronous machines. The operating principle is identical, but the field-generation means is fixed to the stator, generally encircling the rotor rather than being placed on it. This makes it practically possible to construct the rotor from a single piece of steel. The advantage of having the field windings on the stator is a very attractive one for high-speed flywheel applications. Due to this feature, rotor and flywheel can be integrated into a single piece of steel, which improves the volume/weight ratio of the system. However, the utilization of the magnetic circuit is lower than that of heteropolar machines [14].

1.2.3 Rice-Lundell Alternator

The Rice-Lundell alternator is often used as the power source for aircraft and automobiles [17, 18]. The structural feature of this machine is that the rotor poles are shaped in the shape of ”claws” and the flux follows a three-dimensional path. The field windings are placed concentrically around a cylindrical rotor core in the original version [18] or on the stator in a modified version for high-speed operation [17, 19], which is either similar with the synchronous homopolar machine stator or excited by permanent magnets.

Rice-Lundell alternators have simple rotor structure and relatively larger field winding space for larger flux density. However, due to their structure, applying conventional analysis techniques such as equivalent circuit and Park's transformation are very limited. Furthermore, larger harmonics are generated by the rotor geometry and non-sinusoidal winding distribution. Although they are widely used for low-power generators, application at high power levels ($>$100 kW) has not yet been reported.

1.2.4 Switched Reluctance Machine

Switched reluctance machines (SRM), also known as variable reluctance machines, have existed since the 1970s, and now this type of machine can offer quite improved power to weight ratios and efficiencies [20]. SRMs have been investigated for various applications [21]. Most of them have a doubly salient structure which has been proven experimentally to match and frequently exceed the torque per frame size achievable with an induction motor [22].

The advantages of SRM are the absence of permanent magnets and field windings in the rotor, the magnetic and electric independence of their phases, and the mechanical integrity of their rotors. However, their stator/rotor structure and the drive techniques are different than

those of other rotating AC machines. A higher fundamental frequency is required due to the higher pole/phase numbers, and larger harmonics are generated because of the square-wave current. Furthermore, the requirements of a laminated rotor structure and its resulting effect on the structural dynamics of the flywheel rotor are significant problems for flywheel applications.

1.2.5 Synchronous Reluctance Machine

The synchronous reluctance machine (SynRM) was developed in the 1960's as a line-start synchronous AC machine for applications where several motors are operated synchronously from a single voltage-source inverter. However, it has not been widely used because of the difficulty of start-up from the utility grid, poor efficiency and low power factor. Also, it was replaced by PM machines in some cases because PM machines had better performance and allowed more machines to run from a single inverter because SynRMs needed reactive power from the inverter to be magnetized [23].

In last two decades, the development of power electronics devices and circuits, such as pulse-width-modulated (PWM) inverter, and field-oriented "vector" control techniques have changed the paradigm of industrial drives. Use of an inverter for a single machine has been increased, and rugged AC drives have obtained popularity due to matching performance and competitive cost with respect to DC drives. Although induction machines have been most commonly used in AC drives, PM synchronous machines have been used as well.

When using a variable frequency drive for a single machine, a rotor cage for line start-up is not required. With removal of the rotor cage, the synchronous reluctance machine has become an alternative to induction machines and PM machines. Since the reluctance machine is singly-excited, and can possess good structural integrity of its rotor without any windings or permanent

magnets, the reluctance machine can be a relatively simple, low-cost configuration compared with other types of machines. Furthermore, the stator and the inverter power circuit are identical to those of induction and PM machines.

The most important factor for SynRM's performance will be its anisotropy ratio, which is the ratio between the inductance of the direct and quadrature axes. This anisotropy has a crucial influence on torque per volume, power factor, and kVA rating of the inverter. The ratio of the conventionally laminated rotor is less than 10. But with an axially-laminated anisotropy (ALA) rotor, the ratio can be increased up to 20 [24]. The ALA rotor saliency can be created by alternating layers of magnetic and nonmagnetic metals connected by a high-strength bonding process, such as brazing, and is therefore able to possess excellent structural integrity. The performance of SynRMs has become competitive to other types of machines with this high saliency ratio [25].

SynRMs have attractive features for motor/generators in flywheel applications. They ideally have no spinning loss because there are no permanent magnets and no excitation for zero torque. Furthermore, ideally they do not generate rotor losses in steady-state, although in practice some rotor loss exists. The SynRM's stator is the same as that of other AC machines, and well known field-oriented control techniques are applicable. It has been shown that the SynRMs are well suited for a high-performance and high-speed drive [25, 26] and have been successfully applied to flywheel systems [27].

However, the brazed rotor is a solid piece of steel, and therefore eddy currents can flow freely in the rotor. Unlike the laminated rotor, the analysis of this type of synchronous reluctance rotor cannot ignore the effect of the rotor current, because the rotor flux dynamics due to rotor currents affects the machine's performance. This has not been investigated elsewhere, and hence represents a key contribution of the thesis.

1.3 Overview of Thesis

This thesis presents a control system for a high-speed solid-rotor synchronous reluctance flywheel motor/generator. The objective of this research is to derive a model for a solid-rotor machine and provide a control scheme which has stable performance at high speed based on the derived model. The control system should be robust with respect to parameter deviation caused by practical factors such as nonlinear magnetics, rotor temperature variation and inaccurate measurement. This project also includes the filter design to improve the thermal performance of the system.

Chapter 2 represents an introduction to synchronous reluctance machine theory. Chapter 3 derives a dynamic model for a solid-rotor synchronous reluctance machine, including rotor flux linkage dynamics, and develops a feedforward controller based on the proposed model. Chapter 4 presents a modified model which takes into account nonlinear magnetics. Chapter 5 discusses feedback compensation for the feedforward controller to handle the possible deviation of the parameters. In Chapter 6, a three-phase LC filter design is investigated to reduce the rotor loss caused by voltage harmonics. Chapters 3 through 6 include experimental results to validate the theory. Finally, conclusions are presented in Chapter 7.

The contribution of this thesis is the derivation of a model for solid-rotor synchronous reluctance machine and design of a flywheel motor/generator controller based on the model. Additionally, this research includes solutions for practical difficulties such as nonlinear magnetics, parameter inaccuracy, and time-harmonic losses.

Chapter 2

Synchronous Reluctance Machine

2.1 Introduction

The synchronous reluctance machine's stator is identical to that of the induction machine, which ideally has a smoothly rotating magnetic field. The synchronous reluctance rotor, which has salient rotor poles without field coils, is one of the oldest types of electric machines. Even though there have been numerous studies on the shape of the synchronous reluctance rotor, the main idea is that the magnetic flux produced by the stator has a shortest path through the rotor, which means the smallest magnetic reluctance. The "reluctance torque" is developed on account of this phenomenon, even without any excitation on the rotor. When a load torque is applied, the minimum reluctance path of the rotor begins to lag the rotating field, creating a misalignment (although the rotor still rotates in synchronism with the magnetic field). An electromagnetic torque is then developed which counteracts this load torque. Reluctance machines, synchronous or switched, rely on this reluctance torque rather than the reaction torque to operate.

The fundamental structure of a single-phase, two-pole reluctance machine is shown in Fig. 2.1. The rotor will attempt to achieve the position of minimum reluctance, corresponding to the minimum stored energy in the system under constant flux excitation. In other words, the torque in a reluctance machine is developed by virtue of a change in the reluctance with the rotor position. The reluctance of the rotor as seen by the stator can be changed by rotating the field.

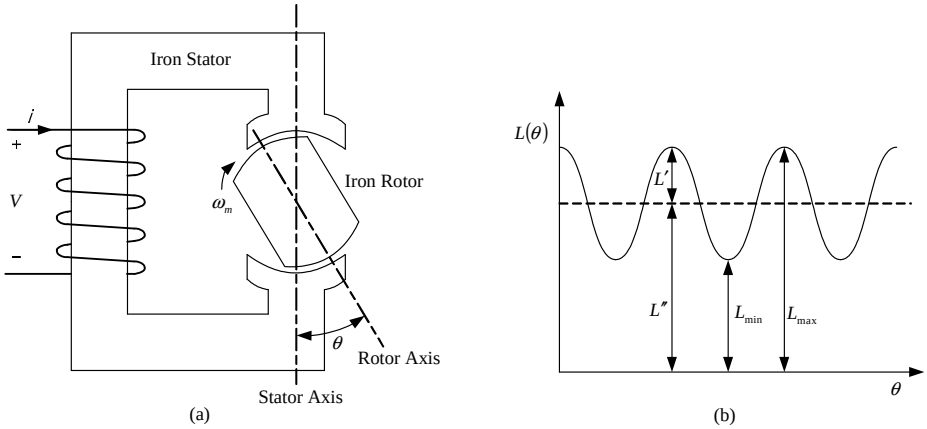

Fig. 2.1. (a) Conceptual diagram of reluctance machine (b) Inductance variation with respect to the rotor position

2.2 Conventional Model

2.2.1 Conceptual Single-phase Machine Model

The inductance of the single-phase machine which is varying according to the rotor position can be expressed as follows. The inductance is shown in Fig. 2.1 (b).

$$L(\theta) = \frac{1}{2}(L_{max} - L_{min})\cos 2\theta + \frac{1}{2}(L_{max} - L_{min}) + L_{min} \tag{2.1}$$

Then the coenergy and instantaneous torque will be given as

$$W'_{fld} = \frac{1}{2}L(\theta)i^2 \tag{2.2}$$

$$\tau_{inst}(\theta) = \frac{\partial W'_{fld}}{\partial \theta} \tag{2.3}$$

$$= -\frac{i^2}{2}(L_{max} - L_{min})\sin 2\theta \tag{2.4}$$

where,

$$i = I_m \sin \omega t \tag{2.5}$$

It is assumed that the rotor is rotating at an angular velocity ω_m, where δ is an initial rotor position at $t = 0$. Then the instantaneous position is given as,

$$\theta = \omega_m t - \delta \tag{2.6}$$

The average torque is non-zero only when the $\omega = \omega_m$, which is known as the synchronous speed. The average torque can be derived as follows.

$$\tau_{ave} = \frac{1}{T} \int_0^T \tau_{inst}(\theta) dt \tag{2.7}$$

$$= \frac{1}{8} I_m^2 \left(L_{max} - L_{min}\right) \sin 2\delta \tag{2.8}$$

Eqs. (2.3), (2.8) clearly show the influence of the saliency ratio L_{max}/L_{min} on torque. The torque is called the reluctance torque, which will be zero if $L_{max} = L_{min}$. The torque varies sinusoidally with the angle δ, which is called the ”torque angle”.

2.2.2 Phase Conversion

Three-phase machines, as shown in Fig. 2.2 (a), are most commonly utilized in industrial applications, whereas the two-phase machine model in Fig. 2.2 (b) is conceptually simpler. As the three-phase machine is balanced, an equivalent two-phase or *d-q* model of a three-phase

machine is normally used for dynamic modeling. In a two-phase model, the variables and parameters are expressed in orthogonal or mutually decoupled direct- (*d*-) and quadrature- (*q*-) axis. The two-phase equivalent of a three-phase machine can be obtained by using following conversion matrix, which is known as three-two phase conversion.

$$\begin{bmatrix} i^s_{sd} \\ i^s_{sq} \\ i^s_{s0} \end{bmatrix} = \begin{bmatrix} 2/3 & -1/3 & -1/3 \\ 0 & \sqrt{3}/3 & -\sqrt{3}/3 \\ 1/3 & 1/3 & 1/3 \end{bmatrix} \begin{bmatrix} i_{sa} \\ i_{sb} \\ i_{sc} \end{bmatrix}$$
$$= \mathbf{T}_{23} \begin{bmatrix} i_{sa} \\ i_{sb} \\ i_{sc} \end{bmatrix} \tag{2.9}$$

The two-three phase conversion, which is the inverse of the three-two phase conversion, can be given as follows:

$$\begin{bmatrix} i_{sa} \\ i_{sb} \\ i_{sc} \end{bmatrix} = \begin{bmatrix} 1 & 0 & 1 \\ -1/2 & \sqrt{3}/2 & 1 \\ -1/2 & -\sqrt{3}/2 & 1 \end{bmatrix} \begin{bmatrix} i^s_{sd} \\ i^s_{sq} \\ i^s_{s0} \end{bmatrix}$$
$$= \mathbf{T}_{32} \begin{bmatrix} i^s_{sd} \\ i^s_{sq} \\ i^s_{s0} \end{bmatrix} \tag{2.10}$$

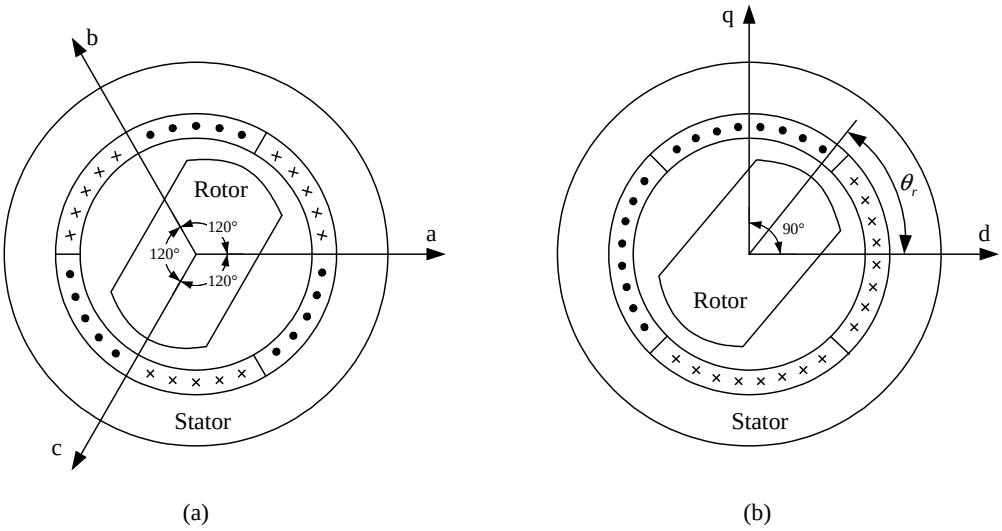

Fig. 2.2. Three-phase and two-phase two-pole smooth-airgap machines

The subscripts '*d*' and '*q*' represent direct- and quadrature-axis values respectively, and the superscript '*s*' represents the stator reference frame, which will be discussed in the following section.

2.2.3 Reference Frame Transformation

While the two-phase modeling results in a compact form, the essential sinusoidal coupling between the stator and rotor circuits with rotor position θ_r still remains. As θ_r is a function of time, this rotational movement of the rotor complicates the analysis. However, referring the rotor and stator equations to a synchronously rotating reference frame, which is called the "rotor" reference frame, can eliminate this complexity. The non-rotating reference frame which is associated with the stator is termed the "stator" or "stationary" reference frame. Axes of these reference frames are shown in Fig. 2.3.

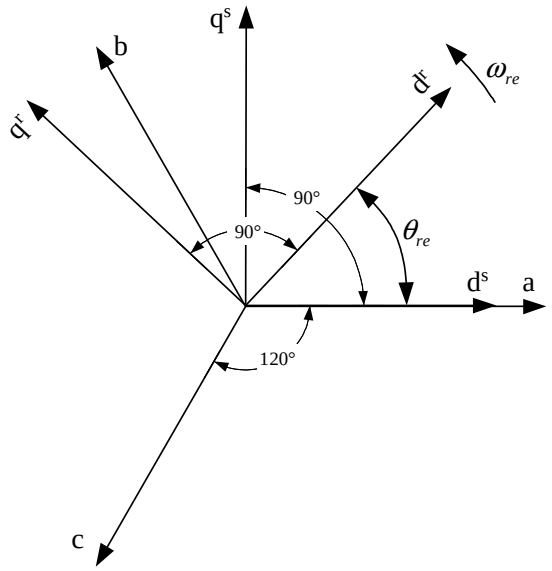

Fig. 2.3. Rotor reference frame *d-q* axes related to the stator reference frame *d-q* and *abc* axes

The conversion matrix for stator to rotor reference frame is given as

$$\begin{bmatrix} i^r_{sd} \\ i^r_{sq} \end{bmatrix} = \begin{bmatrix} \cos\theta_{re} & \sin\theta_{re} \\ -\sin\theta_{re} & \cos\theta_{re} \end{bmatrix} \begin{bmatrix} i^s_{sd} \\ i^s_{sq} \end{bmatrix}$$
$$= \mathbf{T}_{s2r} \begin{bmatrix} i^s_{sd} \\ i^s_{sq} \end{bmatrix} \tag{2.11}$$

The inverse conversion from rotor to stator reference frame is given as follows:

$$\begin{bmatrix} i^s_{sd} \\ i^s_{sq} \end{bmatrix} = \begin{bmatrix} \cos\theta_{re} & -\sin\theta_{re} \\ \sin\theta_{re} & \cos\theta_{re} \end{bmatrix} \begin{bmatrix} i^r_{sd} \\ i^r_{sq} \end{bmatrix}$$
$$= \mathbf{T}_{r2s} \begin{bmatrix} i^r_{sd} \\ i^r_{sq} \end{bmatrix} \tag{2.12}$$

2.2.4 Three-phase Machine Model

As can be seen in Fig. 2.1 (b), the self-inductance of one phase of the stator windings varies sinusoidally from a maximum value to a minimum value. As a 180° rotation of the rotor results in the same inductance seen by a phase winding, the inductance therefore varies sinusoidally with twice the rotor angle. Hence, the self-inductance of phase *a* of the three-phase synchronous reluctance machine in Fig. 2.4 is given as:

$$L_{aa} = L_{\ell s} + L'' + L' \cos(2\theta_r) \tag{2.13}$$

where $L_{\ell s}$ is leakage inductance.

The mutual inductance between two phases is given by the gap inductance phase-shifted by $\pm 120^\circ$:

$$\begin{aligned} L_{ab} &= L'' \cos(120^\circ) + L' \cos\{2(\theta_r + 120^\circ)\} \\ &= -\frac{1}{2} L'' + L' \cos(2\theta_r - 120^\circ) \end{aligned} \tag{2.14}$$

Therefore, the total flux-linkage/current relationships for a three-phase machine are as follows:

$$\begin{aligned}\begin{bmatrix} \lambda_{sa} \\ \lambda_{sb} \\ \lambda_{sc} \end{bmatrix} &= \begin{bmatrix} L_{aa}(\theta_r) & L_{ab}(\theta_r) & L_{ac}(\theta_r) \\ L_{ab}(\theta_r) & L_{bb}(\theta_r) & L_{bc}(\theta_r) \\ L_{ac}(\theta_r) & L_{cb}(\theta_r) & L_{cc}(\theta_r) \end{bmatrix} \begin{bmatrix} i_{sa} \\ i_{sb} \\ i_{sc} \end{bmatrix} \\ &= \mathbf{L}_{abc}(\theta_r) \begin{bmatrix} i_{sa} \\ i_{sb} \\ i_{sc} \end{bmatrix} \end{aligned} \tag{2.15}$$

where

$$\begin{aligned} L_{aa}(\theta_r) &= L_{\ell s} + L'' + L' \cos(2\theta_r), \\ L_{ab}(\theta_r) &= -\frac{1}{2}L'' + L' \cos(2\theta_r - 120^\circ), \\ L_{ac}(\theta_r) &= -\frac{1}{2}L'' + L' \cos(2\theta_r + 120^\circ), \\ L_{bb}(\theta_r) &= L_{\ell s} + L'' + L' \cos(2\theta_r + 120^\circ), \\ L_{bc}(\theta_r) &= -\frac{1}{2}L'' + L' \cos(2\theta_r), \\ L_{cc}(\theta_r) &= L_{\ell s} + L'' + L' \cos(2\theta_r - 120^\circ). \end{aligned} \tag{2.16}$$

The relationships become as follows in two-phase equivalent form:

$$\begin{bmatrix} \lambda^s_{sd} \\ \lambda^s_{sq} \\ \lambda^s_{s0} \end{bmatrix} = \mathbf{T}_{23}\mathbf{L}_{abc}(\theta_r)\mathbf{T}_{32} \begin{bmatrix} i^s_{sd} \\ i^s_{sq} \\ i^s_{s0} \end{bmatrix} \tag{2.17}$$

$$= \begin{bmatrix} \frac{3}{2}\{L'' + L'\cos(2\theta_r)\} + L_{\ell s} & \frac{3}{2}L'\sin(2\theta_r) & 0 \\ \frac{3}{2}L'\sin(2\theta_r) & \frac{3}{2}\{L'' + L'\cos(2\theta_r)\} + L_{\ell s} & 0 \\ 0 & 0 & L_{\ell s} \end{bmatrix} \begin{bmatrix} i^s_{sd} \\ i^s_{sq} \\ i^s_{s0} \end{bmatrix}$$

Hereby the maximum self-inductance as the "direct" inductance L_{sd} and the minimum self-inductance as the "quadrature" inductance L_{sq} can be defined as follows.

$$L_{sd} = \frac{3}{2}\{L'' + L'\} + L_{\ell s} \tag{2.18}$$

$$L_{sq} = \frac{3}{2}\{L'' - L'\} + L_{\ell s} \tag{2.19}$$

Under balanced conditions, the zero-sequence components will be all zero. Hence, rewriting (2.20) yields:

$$\begin{bmatrix} \lambda^s_{sd} \\ \lambda^s_{sq} \end{bmatrix} = \mathbf{L}_{dq}(\theta_r) \begin{bmatrix} i^s_{sd} \\ i^s_{sq} \end{bmatrix} \tag{2.20}$$

where

$$\mathbf{L}_{dq}(\theta_r) = \begin{bmatrix} \frac{1}{2}\{(L_{sd}+L_{sq}) + (L_{sd}-L_{sq})\cos(2\theta_r)\} & \frac{1}{2}(L_{sd}-L_{sq})\sin(2\theta_r) \\ \frac{1}{2}(L_{sd}-L_{sq})\sin(2\theta_r) & \frac{1}{2}\{(L_{sd}+L_{sq}) - (L_{sd}-L_{sq})\cos(2\theta_r)\} \end{bmatrix} \tag{2.21}$$

For further simpler representation of the machine, a stator reference frame model is transformed to the rotor reference frame as follows:

$$\begin{bmatrix} \lambda^r_{sd} \\ \lambda^r_{sq} \end{bmatrix} = \mathbf{T}_{s2r} \begin{bmatrix} \lambda^s_{sd} \\ \lambda^s_{sq} \end{bmatrix} \tag{2.22}$$

$$= \mathbf{T}_{s2r}\mathbf{L}_{dq}(\theta_r)\mathbf{T}_{r2s} \begin{bmatrix} i^r_{sd} \\ i^r_{sq} \end{bmatrix} \tag{2.23}$$

$$= \begin{bmatrix} L_{sd} & 0 \\ 0 & L_{sq} \end{bmatrix} \begin{bmatrix} i^r_{sd} \\ i^r_{sq} \end{bmatrix} \tag{2.24}$$

The co-energy of this equivalent two-phase machine is given as follows:

$$W'_{fld}(\theta_r) = \int_0^{i^s_{sd}} \lambda_d(i^{s\prime}_d, 0)di^{s\prime}_d + \int_0^{i^s_{sq}} \lambda_q(i^s_{sd}, i^{s\prime}_{dq})di^{s\prime}_q \tag{2.25}$$

$$\begin{aligned} &= \int_0^{i^s_{sd}} \frac{1}{2}\left\{(L_{sd}+L_{sq}) + (L_{sd}-L_{sq})\cos(2\theta_r)\right\} i^{s\prime}_d di^{s\prime}_d \\ &\quad + \int_0^{i^s_{sq}} \left[\frac{1}{2}(L_{sd}-L_{sq})\sin(2\theta_r)i^s_{sd} + \frac{1}{2}\left\{(L_{sd}+L_{sq}) - (L_{sd}-L_{sq})\cos(2\theta_r)\right\} i^{s\prime}_q\right] di^{s\prime}_q \\ &= \frac{1}{4}\left\{(L_{sd}+L_{sq}) + (L_{sd}-L_{sq})\cos(2\theta_r)\right\}(i^{s2}_d - i^{s2}_q) + \frac{1}{2}(L_{sd}-L_{sq})\sin(2\theta_r)i^s_{sd}i^s_{sq} \end{aligned} \tag{2.26}$$

Two-phase torque is therefore derived from the co-energy.

$$\tau_{2ph} = \frac{\partial W'_{fld}(\theta_r)}{\partial \theta_r} \tag{2.27}$$

$$= \frac{\partial}{\partial \theta_r}\left[\frac{1}{4}\left\{(L_{sd}+L_{sq})+(L_{sd}-L_{sq})\cos(2\theta_r)\right\}(i_d^{s2}-i_q^{s2})+\frac{1}{2}(L_{sd}-L_{sq})\sin(2\theta_r)(i_{sd}^{s}i_{sq}^{s})\right]$$

$$= -\frac{1}{2}(L_{sd}-L_{sq})\sin(2\theta_r)(i_d^{s2}-i_q^{s2})+(L_{sd}-L_{sq})\cos(2\theta_r)i_{sd}^{s}i_{sq}^{s}$$

$$= (L_{sd}-L_{sq})\left[-\frac{1}{2}\cdot 2\sin\theta_r\cos\theta_r(i_d^{s2}-i_q^{s2})+(\cos^2\theta_r-\sin^2\theta_r)i_{sd}^{s}i_{sq}^{s}\right]$$

$$= (L_{sd}-L_{sq})(i_{sd}^{s}\cos\theta_r+i_q^{s}\cos\theta_r)(i_{sq}^{s}\cos\theta_r-i_d^{s}\cos\theta_r)$$

$$= (L_{sd}-L_{sq})i_{sd}^{r}i_{sq}^{r} \tag{2.28}$$

Hence the torque of three-phase P-pole machine will be given as

$$\tau_{3ph} = \frac{3}{2}\frac{P}{2}\tau_{2ph}$$

$$= \frac{3P}{4}(L_{sd}-L_{sq})i_{sd}^{r}i_{sq}^{r} \tag{2.29}$$

The equivalent circuit in the rotor reference frame of an ideal three-phase synchronous reluctance machine is shown in Fig. 2.4, and the stator voltage/current equation and flux linkage

in vector notation are shown below.

$$\vec{v}_s^r = R_s\vec{i}_s^r + \mathbf{J}\omega_{re}\vec{\lambda}_s^r + \frac{d\vec{\lambda}_s^r}{dt}, \tag{2.30}$$

$$\vec{\lambda}_s^r = [L_s]\vec{i}_s^r, \tag{2.31}$$

$$\begin{aligned}\tau &= \frac{3P}{4}\left\{\vec{\lambda}_s^r \times \vec{i}_s^r\right\} \\ &= \frac{3P}{4}(L_{sd} - L_{sq})i_{sd}^r i_{sq}^r,\end{aligned} \tag{2.32}$$

where P represents the pole number of the machine, $\omega_{re} = \frac{P}{2}\omega_r$ is the electrical rotor speed, and

$$\vec{x} = \begin{bmatrix} x_d \\ \\ x_q \end{bmatrix}, \quad [Y] = \begin{bmatrix} Y_d & 0 \\ \\ 0 & Y_q \end{bmatrix}, \quad \mathbf{J} = \begin{bmatrix} 0 & -1 \\ \\ 1 & 0 \end{bmatrix} \quad . \tag{2.33}$$

Eqs. (2.30)-(2.32) represent the ”conventional” model of synchronous reluctance machine, which assumes no rotor currents.

2.3 Operating Points

The steady-state torque of a three-phase synchronous reluctance machine has been given in terms of its equivalent two-phase parameters as follows:

$$\tau_{3ph} = \frac{3P}{4}\left(L_d - L_q\right) i_{sd}^r i_{sq}^r$$

For a given torque, there are a number of different combinations of i_{sd}^r and i_{sq}^r that can be used to achieve that torque. Typical operating points are as follows [28]:

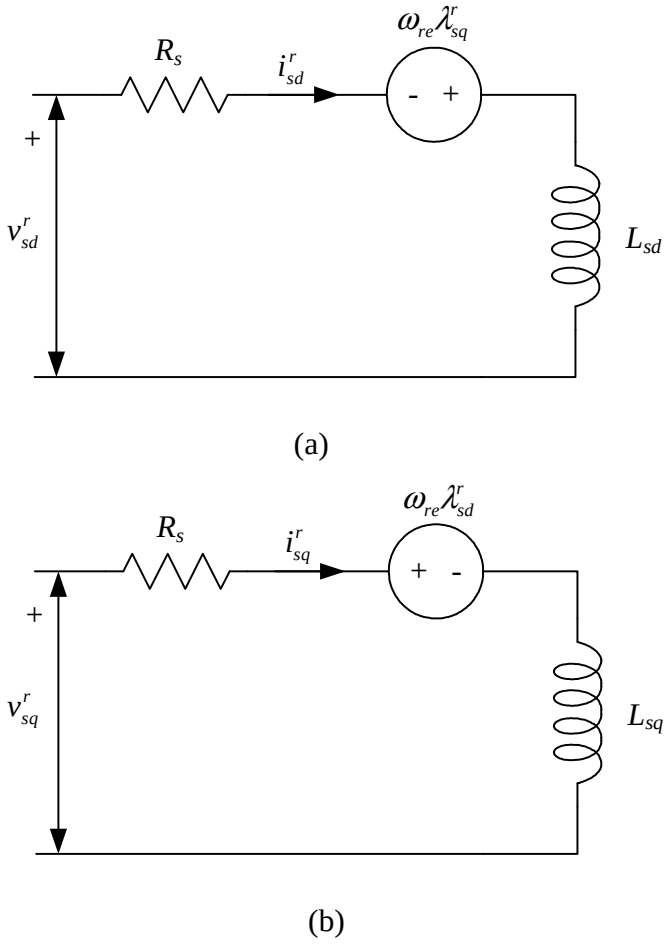

Fig. 2.4. Rotor reference frame equivalent circuits of ideal synchronous reluctance machine

2.3.1 Minimum Current Operating Point

For a given torque, the peak current:

$$i_{spk} = \sqrt{i_{sd}^{r\,2} + i_{sq}^{r\,2}} \tag{2.34}$$

can be minimized by choosing i_{sd}^{r} and i_{sq}^{r} to be equal:

$$i_{sd}^{r} = i_{sq}^{r} = \sqrt{\frac{\tau_{3ph}}{\frac{3P}{4}\left(L_d - L_q\right)}} \tag{2.35}$$

This is a desirable operating point if one wishes to minimize resistive losses in the machine, or if one is limited by the output current capability of the inverter.

2.3.2 Minimum Flux-Linkage Operating Point

Likewise, the peak flux linkage

$$\lambda_{spk} = \sqrt{\lambda_{sd}^{r\,2} + \lambda_{sq}^{r\,2}} \tag{2.36}$$

can be minimized by choosing λ_{sd}^{r} and λ_{sq}^{r} to be equal. In terms of current, this results in the following relationship between i_{sd}^{r} and i_{sq}^{r}:

$$i_{sd}^{r} = \frac{L_q}{L_d} i_{sq}^{r} = \sqrt{\frac{\tau_{3ph} L_q}{\frac{3P}{4} L_{sd}\left(L_d - L_q\right)}} \tag{2.37}$$

This operating point is desirable if one wishes to minimize core losses, which are proportional to the square of flux-linkage, or if one wishes to minimize flux levels to avoid saturation of the machine or to remain within voltage limitations of the inverter driving the machine.

2.3.3 Maximum Power Factor Operating Point

The third possible operating point is one which maximizes the displacement power factor, neglecting stator resistive drop. It can be shown that this operating point is achieved when

$$i_{sd}^{r} = \sqrt{\frac{L_q}{L_d}}\, i_{sq}^{r} = \sqrt{\frac{\tau_{3ph}}{\frac{3P}{4}\sqrt{\frac{L_q}{L_d}}\left(L_d - L_q\right)}}. \tag{2.38}$$

This operating point is desirable if one is limited by both voltage and current constraints, as it generates the most torque for a given voltage-current product. It is also a reasonably efficient operating point. Other operating points than these can, of course, be chosen to achieve certain criteria, such as the maximization of efficiency [29].

2.4 Conventional Controllers

2.4.1 Scalar Controllers

A scalar controller of an AC machine only controls the magnitude of the control variables. Voltage can be used to control the flux, and frequency can be used to control the torque. However, flux and torque are functions of frequency and voltage, respectively but they cannot be controlled individually in scalar control. By contrast, vector control involves the variation of both the magnitude and phase of the control variables, thereby allowing independent control of flux and torque.

Volt/hertz control is one of the scalar control schemes, and it has been usually used for speed control of induction machines. Assuming negligible stator resistance and symmetrical sinusoidal stator voltages, the main flux can be maintained constant if the stator voltage and its frequency are controlled to keep a constant ratio.

$$\begin{aligned} \lambda &= \int V \sin \omega t dt \\ &= -\frac{V}{\omega} \cos \omega t \end{aligned} \tag{2.39}$$

As long as the same air-gap flux is maintained, same torque will be produced with a certain amount of current regardless of the rotating speed.

A load will determine the torque, because generated torque will be proportional to the load angle for synchronous machines or slip frequency for induction machines. Although the speed of the machine can be controlled by the applied frequency of the voltage without any feedback from the machine, the performance is quite inferior because torque cannot be controlled with any degree of accuracy. Hence, it is difficult to operate with full torque at low speed or standstill. However, a simple open-loop control scheme can be an advantage for applications that do not require high levels of accuracy or precision, such as fans and pumps. Also, a closed speed control loop can be implemented for scalar controller to improve the performance.

A phasor diagram of an induction machine is shown in Fig. 2.5. The primary current will be divided into the magnetizing current i_M and the secondary current i_2. When the load increases, the slip and the secondary current increases as well. Point A will move on the circle to point A' as $X_2 i_2$ increases. Since the produced torque will be proportional to the area of OAD,

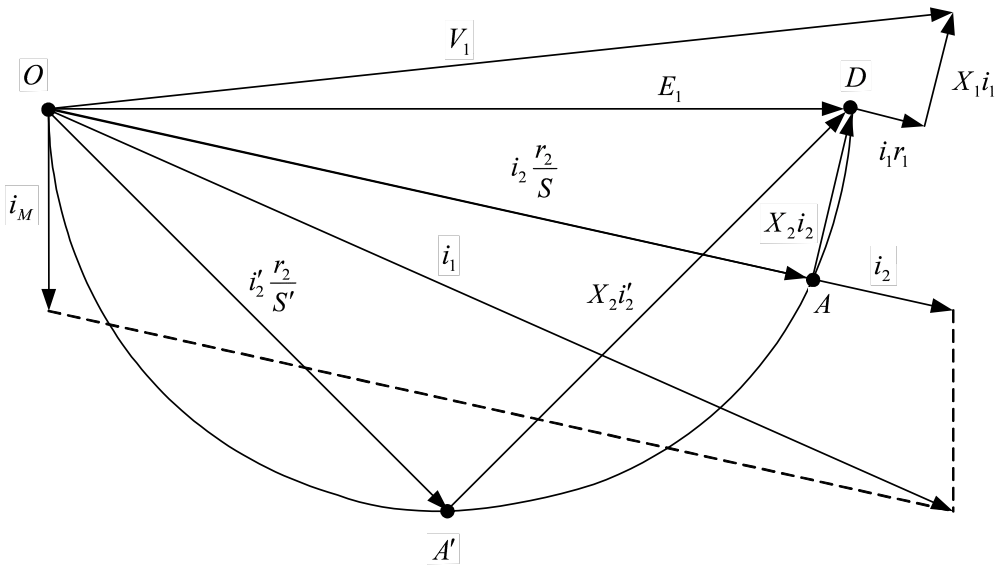

Fig. 2.5. Steady-state vector diagrams of induction machine

the torque will be the maximum when point A reaches point A'. While the secondary current keeps increasing for larger slip than point A', the torque decreases.

When a separately excited synchronous motor runs under load, rotor rotates still in synchronism but mechanically falls behind the stator poles. This produces an electrical phase shift δ between applied voltage phasor $\hat{E}_1$ and induced voltage phasor $\hat{E}_2$, which can be seen in the Fig. 2.6 (a). The phase shift produces a phasor current over the impedance $Z = R + jX$ as follows.

$$\hat{I} = \frac{\hat{E}_1 - \hat{E}_2}{Z} \tag{2.40}$$

$$= \frac{E_1}{|Z|}\angle(\delta - \phi_z) - \frac{E_2}{|Z|}\angle -\phi_z \tag{2.41}$$

where, $\phi_z =$ angle of impedance Z.

Then the power supplied and delivered are given as

$$P_1 = \frac{E_1 E_2}{|Z|}\sin(\delta - \phi_1) + \frac{E_1^2 R}{|Z|^2} \tag{2.42}$$

$$P_2 = \frac{E_1 E_2}{|Z|}\sin(\delta + \phi_1) - \frac{E_2^2 R}{|Z|^2} \tag{2.43}$$

where,

$$\phi_1 = \frac{\pi}{2} - \phi_z. \tag{2.44}$$

If we neglect the resistance, then

$$P_1 = P_2 = \frac{E_1 E_2}{X}\sin\delta \tag{2.45}$$

The generated torque can be given as

$$\tau = \frac{P_2}{\omega_r} \tag{2.46}$$

The phasor diagram is shown in Fig. 2.6 (b).

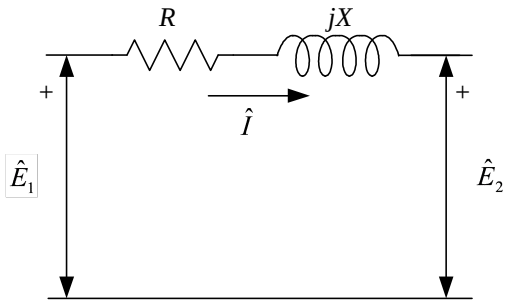

(a)

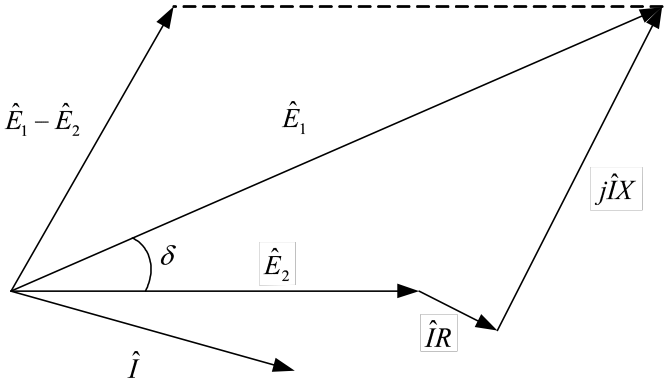

(b)

Fig. 2.6. (a) Equivalent circuit of a separately excited synchronous machine (b) Phasor diagram of a synchronous machine under load

2.4.2 Field Oriented Controllers

A DC machine is much easier to control in high-performance application than the singly excited AC machine, because the main flux and armature current distribution are physically fixed in space and can be controlled independently. The torque in a DC machine is given by:

$$T_e = K_t I_a I_f \tag{2.47}$$

where I_a is the armature or torque current and I_f is the field or flux current. In normal operation, the field current is set to maintain the rated field flux, and torque is changed by the armature current.

AC machines are much more complex to control because the flux and current of each phase are strongly coupled and changing with respect to the stator and rotor. Moreover, the secondary current cannot be measured for cage-type rotors, unlike the DC machines. These factors made the torque control of AC machines difficult, and prohibited their use in high-performance drive applications.

However, this DC machine-like control mode has been extensively investigated and applied to various AC machine control systems since the field-oriented controller was introduced in 1960s. The idea is that the sinusoidal variables of AC machine can be expressed as DC quantities in steady-state by rotating the reference frame in synchronism with a magnetic flux vector. The two orthogonal vector components of the stator current vector in this reference frame can represent magnetizing current vector and torque current vector if the synchronously rotating reference frame is correctly oriented. Generally the axes are called direct- and quadrature-axis for magnetizing and torque current, respectively. Zero steady-state error and high dynamic performance

can be achieved with PI regulators because each component is DC in the rotating reference frame.

Compared to scalar controllers such as the volt/hertz controller, field-oriented controllers are also generally referred to as vector controllers because they control both the amplitude and phase of the spatial orientation of the electromagnetic fields in the machine. With a vector controller, an AC machine can be controlled like a separately excited DC machine. This is equally valid for synchronous and induction machines [30, 31].

Usually for non-PM based machines, the rotor flux, which is supplied from the stator, can be made constant by maintaining the flux component of stator current constant, and torque can be increased almost instantly by increasing the torque component. However, the response of direct-axis current can be sluggish because of the large time constant to make the torque response slow, especially for a fast rising torque command.

The regulation of the stator current by means of a fast switching inverter makes it feasible to implement torque control with independent quadrature- and direct-axis current. A fundamental requirement for synchronous machines is the rotor angle information to convert the current command or feedback between the stator reference frame and rotor reference frame.

$$\vec{i}_s^{\,s} = e^{\mathbf{J}\theta_{re}} \vec{i}_s^{\,r} \tag{2.48}$$

The angle information should include the exact rotor position for synchronous machines, while it is not necessary for asynchronous machines. The phase conversion and axis transformation presented in the previous section have to be implemented in the controller to achieve vector control. The voltage equations are illustrated in Fig. 2.7 in the direct- and quadrature-axis.

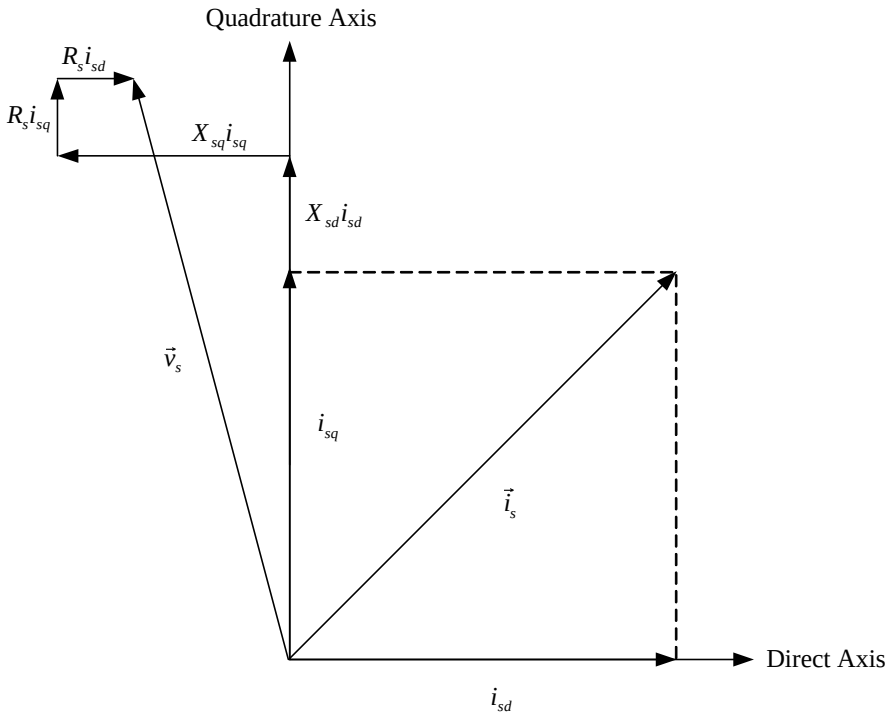

Fig. 2.7. Steady-state vector diagrams of salient pole synchronous machine. X_{sd} and X_{sq} is the direct- and quadrature-axis synchronous reactance, respectively.

In the two-phase model of a synchronous reluctance machine derived in previous section, the electromagnetic torque applied on the rotor shaft has been given as follows in (2.32).

$$\tau = \frac{3P}{4}(L_{sd} - L_{sq}) i^r_{sd} i^r_{sq}$$

Although they are not functioning exactly the same, it can be easily seen that the equation is represented in the form of DC machine's torque expression (2.47), where i^r_{sd} corresponds to the field current I_f and i^r_{sq} to the armature current I_a. Hence a field-oriented vector controller can readily be designed based on this model.

2.4.3 Feedback Controllers

A feedback controller, by definition, utilizes feedback information such as control states or system outputs from the dynamic system. For inverter-fed machine drive systems, the controller is generally placed between the error of the motor current from the command current, and the input of the PWM inverter. It has advantages over open-loop controller such as better disturbance rejection, robustness for uncertainties, and low sensitivity to parameter variations. For high-performance machine drives, various kinds of feedback controllers are investigated and implemented for AC machines as well as DC machines [31–33].

For the torque control of an inverter-fed machine, feedback controllers with PI regulators have been implemented in the stator and the rotor reference frame. Although stator frame regulators have the advantage of simplicity, there are disadvantages in high-speed applications, such as steady-state current error, phase delay, and bandwidth limitations. Therefore, closed-loop control of direct- and quadrature-axis currents in the rotor reference frame has been widely used for AC machine control because the steady-state currents become DC in the rotor reference frame, and a simple PI controller will result in zero steady-state error. A typical system diagram for a synchronous current regulator is shown in Fig. 2.8.

However, the rotor reference frame regulator has speed-dependent cross-coupling between the direct- and quadrature-axes, and the need to transform the signals between the stator and the rotor reference frames makes the implementation of a rotor reference frame regulator complex [31].

Also, in some applications, where the ratio of the sampling to the fundamental frequency is insufficient, it can be seen that the synchronous regulator loses its stability as the excitation

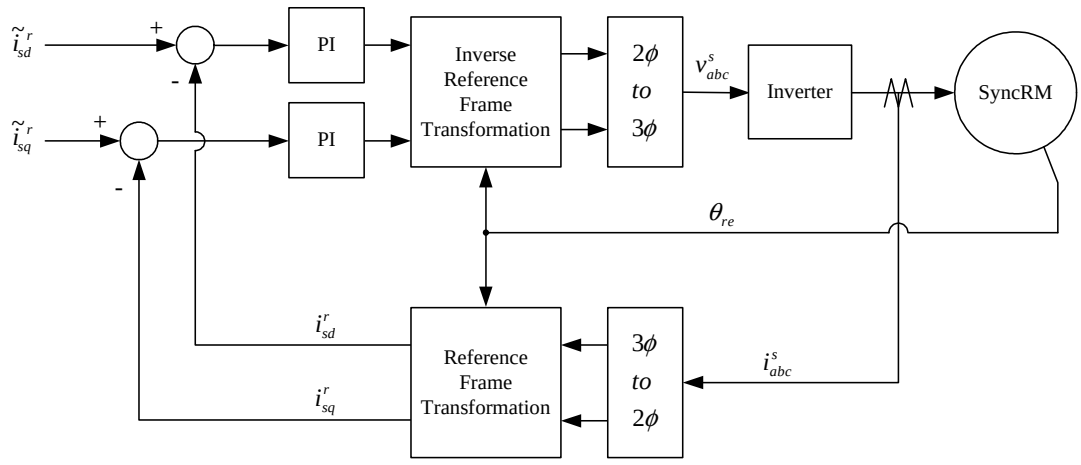

Fig. 2.8. Conventional feedback current control system in rotor reference frame using PI regulators

frequency increases due to the errors caused by the rotation of the reference frame during the time delay. Synchronous regulators implemented in the discrete-time domain have several sources for time delay, which have to be compensated for stable high-speed operation.

The frequency-domain transfer function of the rotor reference frame PI regulators can be expressed in the stator reference frame as follows [34]. The transfer function between current error and voltage commands in the stator reference frame is shown in (2.49). Transformation to and from the rotor reference frame are included.

$$\begin{bmatrix} v_{sd}^s \\ \\ v_{sq}^s \end{bmatrix} = \begin{bmatrix} K_P + \dfrac{K_I s}{s^2+\omega_{re}^2} & \dfrac{K_I \omega_{re}}{s^2+\omega_{re}^2} \\ \\ -\dfrac{K_I \omega_{re}}{s^2+\omega_{re}^2} & K_P + \dfrac{K_I s}{s^2+\omega_{re}^2} \end{bmatrix} \begin{bmatrix} \Delta i_{sd}^s \\ \\ \Delta i_{sq}^s \end{bmatrix} \tag{2.49}$$

$$= \{K_p\,\mathbf{I} + \frac{K_I}{s^2+\omega_{re}^2}\,(s\mathbf{I} - \omega_{re}\mathbf{J})\}\Delta\vec{i}_s^s \tag{2.50}$$

As can be seen in (2.49), the poles associated with the integral term of the controller are centered around the synchronous frequency ω_{re}. Hence, it will have infinite gain at ω_{re}, which means infinite DC gain in the rotor reference frame, and achieves zero steady-state error. However, this is under the assumption of balanced three-phase currents. Thus, if there exists some offsets in the stator reference frame, the rotor reference frame PI regulator no longer regulates this offset to zero because the controller gain is finite at stationary DC.

Moreover, the dynamic behavior of the machine changes as a function of rotor speed in the rotor reference frame. From (2.30), the voltage/current dynamic relationship in the rotor reference frame can be given as follows:

$$\begin{aligned} \frac{d}{dt}\vec{i}_s^r &= [L_s]^{-1}\left(\vec{v}_s^r - R_s\vec{i}_s^r - \omega_{re}\mathbf{J}[L_s]\vec{i}_s^r\right) \\ &= -[L_s]^{-1}\left(R_s + \omega_{re}\mathbf{J}[L_s]\right)\vec{i}_s^r + [L_s]^{-1}\vec{v}_s^r \end{aligned} \tag{2.51}$$

The complex poles of the system become more imaginary with increasing rotational speed ω_{re}. This creates challenges in ensuring stability of operation while maintaining high performance over the entire speed range of the machine.

The field-oriented vector control of currents in the rotor reference frame can be considered as a mature technique in rotating AC machine control. However, although simple and intuitive, the direct- and quadrature-axis current feedback control based on this ideal model has some drawbacks, which are related in particular to high-speed, high-load or flux-weakened conditions, due to the losses in stator/rotor and nonlinearity such as flux saturation [35, 36].

2.4.4 Feedforward Controllers

A feedforward controller computes its output using only the model of the system. It does not use feedback information, nor observe the output of the system. Feedforward control is useful for well-defined systems where the relationship between input and the output can be modeled by mathematical equations. For the case of a current regulator, if a machine model (like the one in Section 2.2) and all of the machine parameters are accurately known, it is possible to regulate the stator currents without any current feedback by the feedforward controller because the controller is the exact inverse of the machine transfer function. Thus feedforward control is a different type of open-loop control than the volt/hertz controller in the previous section in the sense that it controls the torque based on the machine model.

For good performance of a feedforward controller, the following will be required:

- The disturbance must be measurable,
- The processing time of the controller must be fast enough to implement the control algorithm,
- A reasonably accurate model is required for the entire operating range, and
- system parameter variations should be within an acceptable range.

If these conditions are met, feedforward control can be a very effective alternative with its advantages of simplicity and low cost. Feedforward control can respond more quickly to known and measurable kinds of disturbances, and it does not have the stability problems that feedback controllers can have. With the development of fast and affordable digital processors, the feedforward controller has become a viable alternative. An example of a feedforward control system in the rotor reference frame is shown in Fig. 2.9.

It is also possible to use a feedforward controller in parallel with a feedback controller. Generally for this configuration, the feedforward portion provides a rough estimate of the control output based on the model. This makes the overall system response faster, and the feedback controller can have a reduced gain so that it can be less sensitive to noise or random errors, and have less of an impact on the stability of the system. For a machine current regulator, a feedforward compensator can estimate quantities such as back-emf, and hence voltage drop, across the machine impedances [31, 37, 38]. A hybrid system of a feedforward/feedback controller is shown in Fig. 2.10.

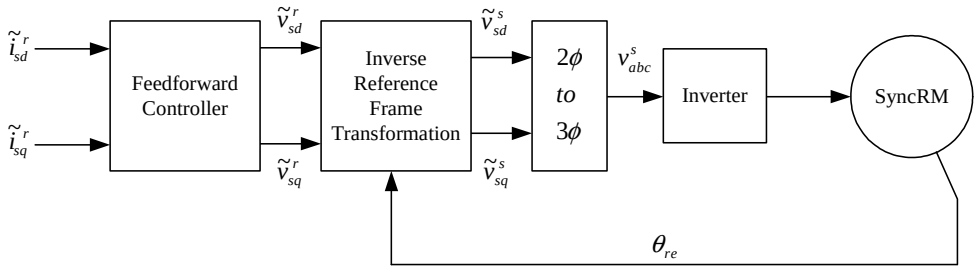

Fig. 2.9. Feedforward current control system in rotor reference frame

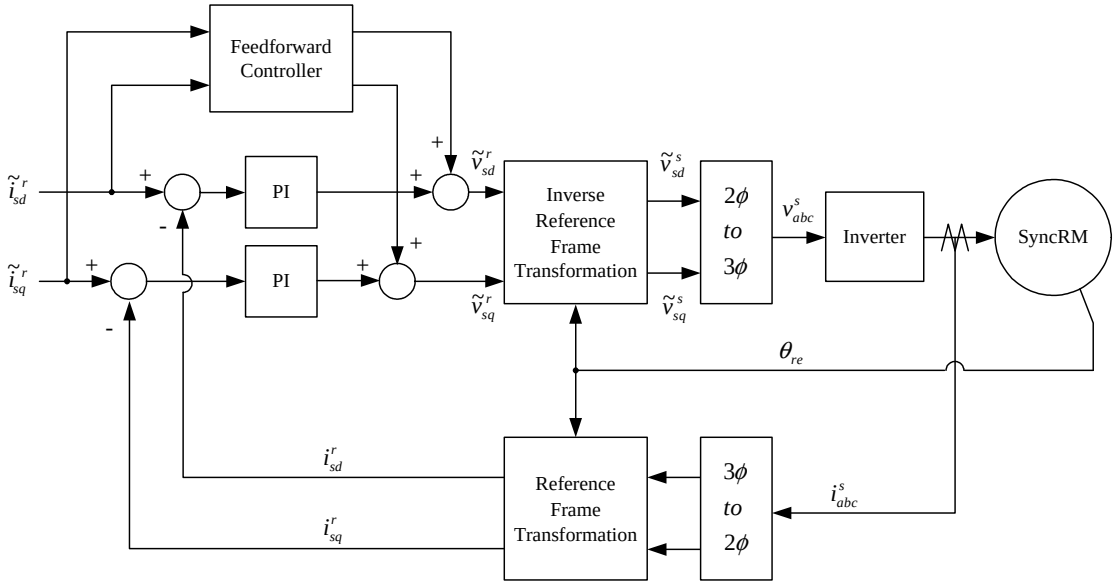

Fig. 2.10. Hybrid current control system in rotor reference frame

Chapter 3

Modeling and Control Considering Rotor Flux Dynamics

3.1 Introduction

The synchronous reluctance machine has received renewed attention with the development of field-oriented control theory and power electronics technology. A singly-excited synchronous reluctance machine can be a relatively simple, low-cost configuration compared with other types of machines due to the non-existence of windings or permanent magnets on the rotor. Especially, it has advantages in certain high-speed applications such as flywheel energy storage systems [27]. This machine has zero ”spinning” losses ideally when no torque is being generated by the machine, as opposed to permanent magnet machines with a stator iron. Furthermore, rotor materials can be chosen which have good structural properties. The rotor of a synchronous reluctance machine design can possess excellent structural integrity if the rotor saliency is created by alternating layers of magnetic and nonmagnetic metals connected by a high-strength bonding process, such as brazing.

However, the solid synchronous reluctance rotor is difficult to laminate, and therefore eddy currents can flow freely in the rotor. The rotor currents in synchronous reluctance machines have been omitted in recent equivalent-circuit-based models [39–42]. Therefore, existing models for synchronous reluctance machines are inadequate if the machine has a solid type rotor, as it does not account for the resulting flux-linkage dynamics associated with a conducting rotor. In particular, when attempting a torque step from zero to full torque, the error associated

with neglecting the rotor flux dynamics is significant, as the rate of change of the flux-linkage is determined by the rotor time constants. The conventional synchronous reluctance machine model can therefore create a current overshoot during transients, as the predicted back-emf is much higher than the actual back-emf of the machine.

A model for synchronous reluctance machines with solid conducting rotors is presented in this chapter. The developed model takes the rotor flux-linkage dynamics into consideration, which are similar to those of an induction machine model, yet include a magnetic saliency of the rotor. First, the dynamic model of a solid-rotor synchronous reluctance machine is presented. Techniques for parameter extraction and discrete-time models for digital implementation of the model are then discussed. Based upon the proposed model, a current regulator is developed and implemented.

The proposed model yields an improved performance for fast-changing torque command compared to the conventional model when utilized in a current regulator. The current regulator based on the proposed model is used in conjunction with a feedback voltage controller to regulate the DC bus voltage of a flywheel energy storage system, which supplies the current regulation setpoint. Experimental results of such a system are presented and discussed.

3.2 Full-Order Model with Rotor Flux Dynamics

3.2.1 Stator Reference Frame Model

Although an electrically-conducting solid rotor of a synchronous reluctance machine is technically a continuum system [43], it can be simply modeled in the rotor reference frame

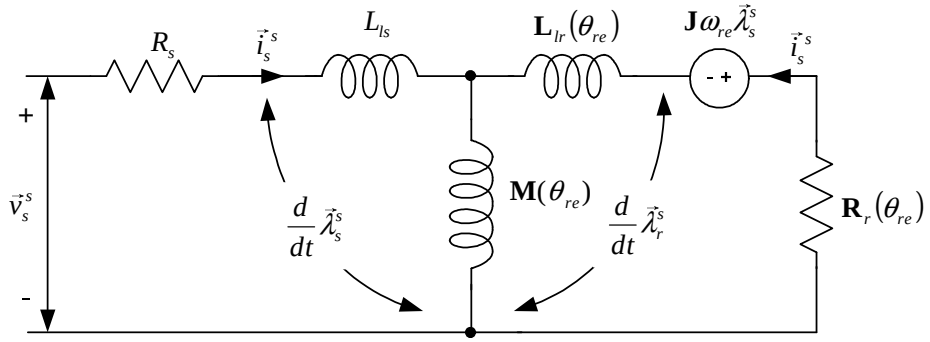

Fig. 3.1. Stator reference frame model of synchronous reluctance machine

through conceptual, shorted direct and quadrature windings on the rotor, similar to what is typically done with squirrel-cage induction machines. Fig. 3.1 presents an equivalent circuit model of a synchronous reluctance machine in the stator reference frame. The superscript 's' represents the stator reference frame.

The voltage equations in the stator reference frame are given as

$$\vec{v}_s^s = R_s\vec{i}_s^s + \frac{d}{dt}\vec{\lambda}_s^s, \tag{3.1}$$

$$\mathbf{0} = \mathbf{R}_r(\theta_{re})\vec{i}_r^s + \frac{d}{dt}\vec{\lambda}_r^s - \omega_{re}\mathbf{J}\vec{\lambda}_r^s, \tag{3.2}$$

where,

$$\vec{\lambda}_s^s = \mathbf{L}_s(\theta_{re})\vec{i}_s^s + \mathbf{M}(\theta_{re})\vec{i}_r^s, \tag{3.3}$$

$$\vec{\lambda}_r^s = \mathbf{L}_r(\theta_{re})\vec{i}_r^s + \mathbf{M}(\theta_{re})\vec{i}_s^s, \tag{3.4}$$

and

$$\vec{x} = \begin{bmatrix} x_d \\ \\ x_q \end{bmatrix}, \quad \mathbf{Y} = \begin{bmatrix} Y_{11} & Y_{12} \\ \\ Y_{21} & Y_{22} \end{bmatrix}. \tag{3.5}$$

The '*d*' and '*q*' subscripts represent direct and quadrature values, respectively.

The inductances and rotor resistance of the synchronous reluctance machine in the stator reference frame are sinusoidally varying according to the rotor position, unlike induction machines, and this makes it difficult to analyze the machine in the stator reference frame. However, it becomes much simpler if the model is transformed into the rotor reference frame. Sinusoidal or position dependent variables in the stator reference frame, such as $\vec{v}_x^s, \vec{i}_x^s, \vec{\lambda}_x^s, \mathbf{L}_s, \mathbf{L}_r, \mathbf{M}$, are converted to DC variables in steady-state in the rotor reference frame.

3.2.2 Rotor Reference Frame Model

The equivalent circuit in Fig. 3.1 can be converted to one based on a rotating reference frame with angular velocity ω_x. Generally the rotating frequency of the spatial flux ω_{re} is selected for ω_x and conversion matrices or complex conversion methods are utilized. The superscript '*r*' represents the rotor reference frame.

$$\vec{x}^r = e^{-\mathbf{J}\theta_{re}} \vec{x}^s, \tag{3.6}$$

where,

$$\theta_{re} = \omega_{re} t - \delta. \tag{3.7}$$

θ_{re} is the instantaneous position where δ is an initial rotor position at $t = 0$.

The voltage equations for the machine in the rotor reference frame can be obtained as follows from (3.1) and (3.2).

$$\vec{v}_s^r = R_s \vec{i}_s^r + \frac{d}{dt}\vec{\lambda}_s^r + \omega_{re}\mathbf{J}\vec{\lambda}_s^r, \tag{3.8}$$

$$\mathbf{0} = [R_r]\vec{i}_r^r + \frac{d}{dt}\vec{\lambda}_r^r, \tag{3.9}$$

where

$$\vec{\lambda}_s^r = [L_s]\vec{i}_s^r + [M]\vec{i}_r^r, \tag{3.10}$$

$$\vec{\lambda}_r^r = [L_r]\vec{i}_r^r + [M]\vec{i}_s^r, \tag{3.11}$$

$$[L_s] = [M] + [L_{\ell s}]\,, \tag{3.12}$$

$$[L_r] = [M] + [L_{\ell r}]\,, \tag{3.13}$$

and

$$[Z] = \begin{bmatrix} Z_d & 0 \\ 0 & Z_q \end{bmatrix}. \tag{3.14}$$

The converted equivalent circuit is shown in Fig. 3.2.

The rotor currents cannot be measured, hence we represent them in terms of stator currents from (3.11).

$$\vec{i}_r^r = \left[\frac{1}{L_r}\right]\vec{\lambda}_r^r - \left[\frac{M}{L_r}\right]\vec{i}_s^r \tag{3.15}$$

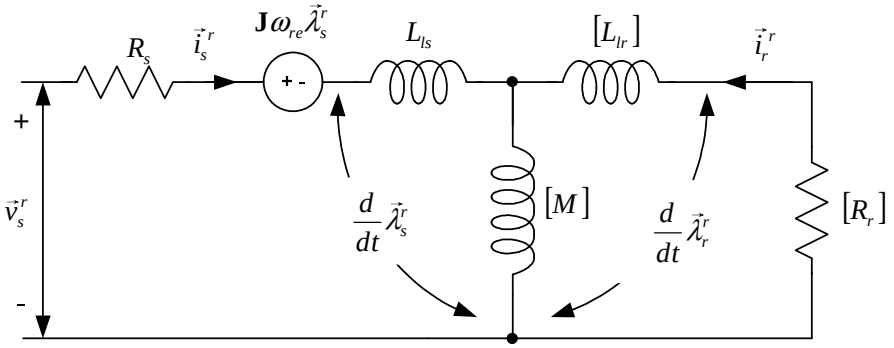

Fig. 3.2. Equivalent circuit model of synchronous reluctance machine in rotor reference frame

$$\vec{\lambda}_s^r = \left[L_s - \frac{M^2}{L_r}\right]\vec{i}_s^r + \left[\frac{M}{L_r}\right]\vec{\lambda}_r^r \tag{3.16}$$

The voltage equations can therefore be rewritten as:

$$\vec{v}_s^r = R_s\vec{i}_s^r + \left[\frac{d}{dt}\mathbf{I} + \omega_{re}\mathbf{J}\right]\left\{\left[L_s - \frac{M^2}{L_r}\right]\vec{i}_s^r + \left[\frac{M}{L_r}\right]\vec{\lambda}_r^r\right\}, \tag{3.17}$$

$$\mathbf{0} = \left(\left[\frac{R_r}{L_r}\right]\left[\frac{M}{L_r}\right] + \frac{d}{dt}\left[\frac{M}{L_r}\right]\right)\vec{\lambda}_r^r - \left[R_r\left(\frac{M}{L_r}\right)^2\right]\vec{i}_s^r. \tag{3.18}$$

By defining a new vector $\vec{\lambda}_a^r$,

$$\vec{\lambda}_a^r = \left[\frac{M}{L_r}\right]\vec{\lambda}_r^r, \tag{3.19}$$

(3.17) and (3.18) can be written as follows:

$$\vec{v}_s^r = R_s\vec{i}_s^r + \omega_{re}\mathbf{J}\left(\left[L_s - \frac{M^2}{L_r}\right]\vec{i}_s^r + \vec{\lambda}_a^r\right) + \frac{d}{dt}\left(\left[L_s - \frac{M^2}{L_r}\right]\vec{i}_s^r + \vec{\lambda}_a^r\right), \tag{3.20}$$

$$\mathbf{0} = \left[\frac{L_r}{R_r}\right]^{-1}\vec{\lambda}_a^r - \left[R_r\left(\frac{M}{L_r}\right)^2\right]\vec{i}_s^r + \frac{d}{dt}\vec{\lambda}_a^r. \tag{3.21}$$

The equivalent circuit that is based on the modified equations is shown in Fig. 3.3.

We will choose the states of the system to be the vectors $\vec{i}_s^r$ and $\vec{\lambda}_a^r$. Hence, the machine dynamics can then be written as follows:

$$\frac{d\vec{\lambda}_a^r}{dt} = -\left[\frac{L_r}{R_r}\right]^{-1}\vec{\lambda}_a^r + \left[R_r\left(\frac{M}{L_r}\right)^2\right]\vec{i}_s^r\,, \tag{3.22}$$

$$\begin{aligned}\frac{d\vec{i}_s^r}{dt} = &\left[L_s - \frac{M^2}{L_r}\right]^{-1}\left\{\vec{v}_s^r - \left[R_s + R_r\left(\frac{M}{L_r}\right)^2\right]\vec{i}_s^r\right.\\ &\left. - \omega_{re}\mathbf{J}\left(\left[L_s - \frac{M^2}{L_r}\right]\vec{i}_s^r + \vec{\lambda}_a^r\right) + \left[\frac{L_r}{R_r}\right]^{-1}\vec{\lambda}_a^r\right\}\end{aligned} \tag{3.23}$$

With this formulation, the dynamics can be expressed in terms of three sets of direct and quadrature parameters, and a scalar parameter:

- Rotor time constants $\left[\frac{L_r}{R_r}\right]$,
- Rotor "excitation" resistance $\left[R_r\left(\frac{M}{L_r}\right)^2\right]$,
- "Leakage" Inductance $\left[L_s - \frac{M^2}{L_r}\right]$, and
- Stator resistance R_s

3.2.3 Parameter Extraction

Both the direct and quadrature values of $\left[L_s - \frac{M^2}{L_r}\right]$ are approximately equal to the stator leakage inductance $L_{\ell s}$, and hence can be estimated, as well as the stator resistance R_s,

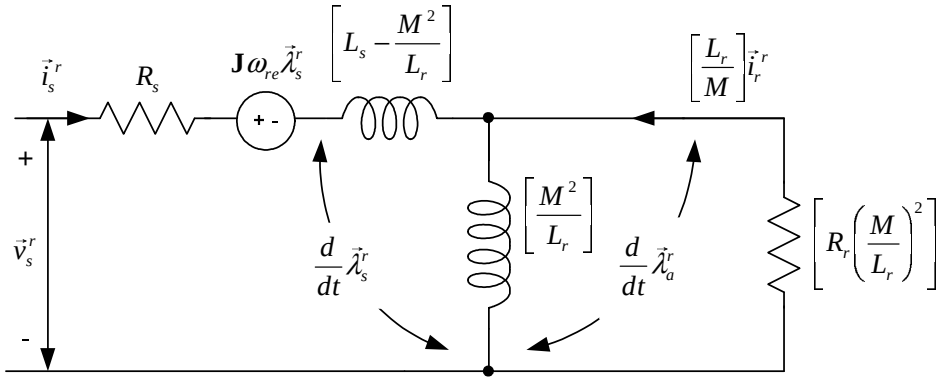

Fig. 3.3. Equivalent circuit in rotor reference frame model of synchronous reluctance machine

through terminal measurements of the stator with the rotor removed. The parameters $\left[\frac{L_r}{R_r}\right]$ and $\left[R_r\left(\frac{M}{L_r}\right)^2\right]$ can be determined from voltage and current measurements using the following procedure:

- Using a feedback current regulator at medium speeds, command either a direct or quadrature current i_{sx}^r to the machine, where the subscript '*x*' stands for the direct or quadrature component.

- Instantaneously turn off all transistors in the 3-phase inverter driving the machine at time $t = 0$. The stator current should quickly (ideally instantaneously) go to zero. In this case the stator voltage of the machine will be due solely to the flux generated by rotor currents:

$$\begin{aligned}\vec{v}_s^{\,r} &= \omega_{re}\mathbf{J}\left[\frac{M}{L_r}\right]\vec{\lambda}_r^r \\ &= \omega_{re}\mathbf{J}\vec{\lambda}_a^r \end{aligned} \tag{3.24}$$

Table 3.1. Synchronous reluctance machine parameters

Stator Resistance R_s	$0.05\ \Omega$
Stator Leakage Inductance $L_{\ell s}$	$9.6\ \mu$H
Direct Rotor Time constant $\frac{L_{rd}}{R_{rd}}$	1.5 msec
Direct Rotor Excitation Constant $R_{rd}\left(\frac{M_d}{L_{rd}}\right)^2$	$0.0013\ \Omega$
Quadrature Rotor Time constant $\frac{L_{rq}}{R_{rq}}$	$300\ \mu$sec
Quadrature Rotor Excitation Constant $R_{rq}\left(\frac{M_q}{L_{rq}}\right)^2$	$0.0003\ \Omega$

From voltage measurements we can therefore easily determine the flux linkage $\vec{\lambda}_a^r$. From the exponential decays of the voltage waveforms we can also estimate the rotor time constants $\left[\frac{L_r}{R_r}\right]$. This can best be done through a curve fitting of the measured data.

We can determine the rotor excitation resistances from the conditions at the turn-off transition ($t = 0$), for both direct and quadrature axes, as follows:

$$\left(\frac{M_x^2}{L_{rx}}\right) = \frac{\lambda_{ax}^r(t=0^+)}{i_{sx}^r(t=0^-)},$$

$$R_{rx}\left(\frac{M_x}{L_{rx}}\right)^2 = \left(\frac{L_{rx}}{R_{rx}}\right)^{-1}\left(\frac{M_x^2}{L_{rx}}\right). \tag{3.25}$$

The resulting parameters of a four-pole, 120 kW, 55,000 rpm solid-rotor synchronous reluctance machine are shown in Table 3.1.

3.2.4 Effect of Solid Rotor on Machine Torque

The effect of the solid-rotor can be seen in the torque expression of the machine. The co-energy of a three-phase solid-rotor synchronous reluctance is derived as follows:

$$W'_{fld}\left(\vec{i}^{s}_{s}, \vec{i}^{r}_{s}\right) = \frac{3}{2}\left[\int_0^{\vec{i}^{s}_{s}} \vec{\lambda}^{s\,T}_{s}\left(\vec{i}^{s\prime}_{s}, 0\right) d\vec{i}^{s\prime}_{s} + \int_0^{\vec{i}^{r}_{r}} \vec{\lambda}^{r\,T}_{r}\left(\vec{i}^{r}_{s}, \vec{i}^{r\prime}_{r}\right) d\vec{i}^{r\prime}_{r}\right] \tag{3.26}$$

$$= \frac{3}{2}\left(\frac{1}{2}\vec{i}^{s\,T}_{s} e^{\mathbf{J}\theta_{re}}[L_s]e^{-\mathbf{J}\theta_{re}}\vec{i}^{s}_{s} + \frac{1}{2}\vec{i}^{r\,T}_{r}[L_r]\vec{i}^{r}_{r} + \vec{i}^{s\,T}_{s} e^{\mathbf{J}\theta_{re}}[M]\vec{i}^{r}_{r}\right) \tag{3.27}$$

The electromagnetic torque is therefore given by:

$$\tau_e = \frac{\partial W'_{fld}}{\partial \theta_{re}} \tag{3.28}$$

$$= \frac{3P}{4}\left[(L_{sd} - L_{sq})i^{r}_{sd}i^{r}_{sq} + Mi^{r}_{rd}i^{r}_{sq} - Mi^{r}_{rq}i^{r}_{sd}\right] \tag{3.29}$$

Under steady-state conditions, the rotor currents are zero, and the torque expression returns to its usual form:

$$\tau = \frac{3P}{4}\left(L_{sd} - L_{sq}\right) i^{r}_{sd}i^{r}_{sq} \tag{3.30}$$

3.3 Control Technique

3.3.1 Model-Based Controller

To validate the proposed model, a model-based controller has been designed to determine the appropriate command voltages to be applied to the machine for a desired current. The controller has been applied to a synchronous reluctance machine in a flywheel energy storage system. Because of the nature of a flywheel energy storage system (i.e., slowly changing rotor

speed), it is straightforward to model the machine dynamics accurately, and hence a model-based controller can be effective. A model-based controller can be an attractive approach for a synchronous reluctance machine, where the voltage is a strong function of current.

Neglecting derivative terms, sufficient accuracy can be achieved by approximating the stator voltage command in (3.21) for a desired current $\vec{i}_s^r$ as follows:

$$\vec{v}_s^r \approx R_s \vec{i}_s^r + \omega_{re} \mathbf{J} \left\{ L_{\ell s} \vec{i}_s^r + \vec{\lambda}_a^r \right\} \tag{3.31}$$

The estimated vector $\vec{\hat{\lambda}}_a^r$ is determined from the desired stator current vector by numerically integrating the following differential equations:

$$\frac{d}{dt} \vec{\hat{\lambda}}_a^r = - \left[\frac{R_r}{L_r} \right] \vec{\hat{\lambda}}_a^r + \left[R_r \left(\frac{M}{L_r} \right)^2 \right] \vec{i}_s^r \tag{3.32}$$

A schematic of this controller is shown in Fig. 3.4. Peak current command i_{spk} is supplied by a feedback controller which regulates DC bus voltage, and the parameter K_d determines the operating point of the synchronous reluctance machine [28]. Figs. 3.5 and 3.6 show the simulated comparison between the conventional and the proposed model. It can be seen that large errors in flux estimation and current regulation are unavoidable if the flux dynamics are not taken into account, especially for fast current command changes. The proposed model estimates the machine flux more accurately than conventional models, which leads to better transient responses for a step command.

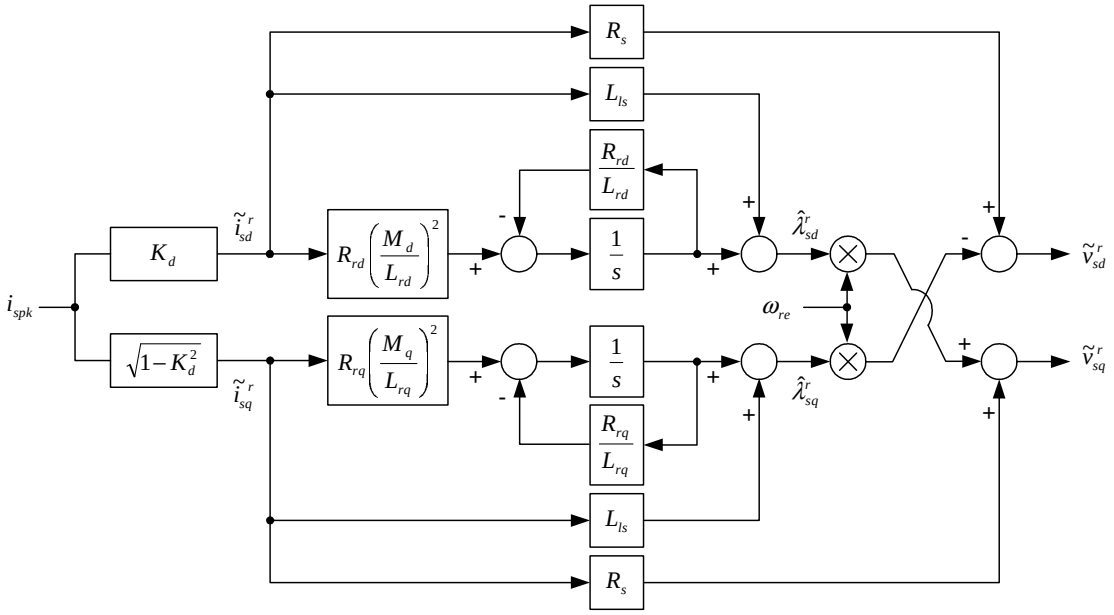

Fig. 3.4. Feedforward current control algorithm in rotor reference frame

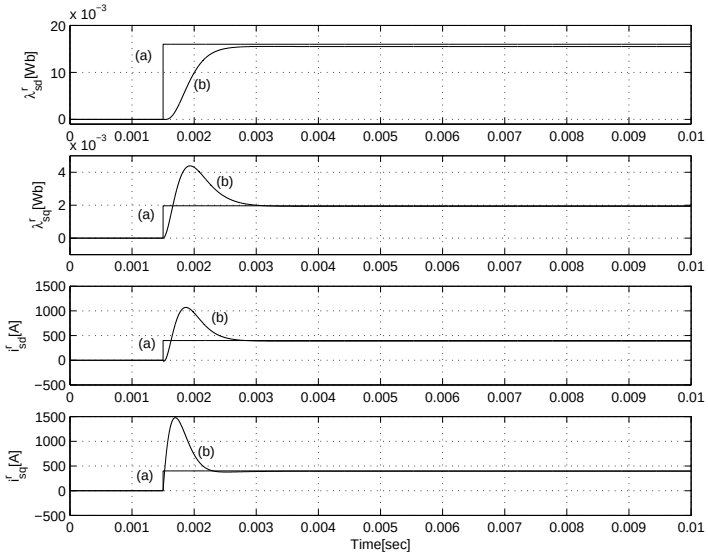

Fig. 3.5. Simulation: Direct and quadrature stator flux estimation and current regulation. Model does not include rotor flux dynamics. 400 A peak current command at 35,000 rpm. λ^r_{sd}, λ^r_{sq}: (a) Estimated (b) Actual, i^r_{sd}, i^r_{sq}: (a) Command (b) Actual (from top)

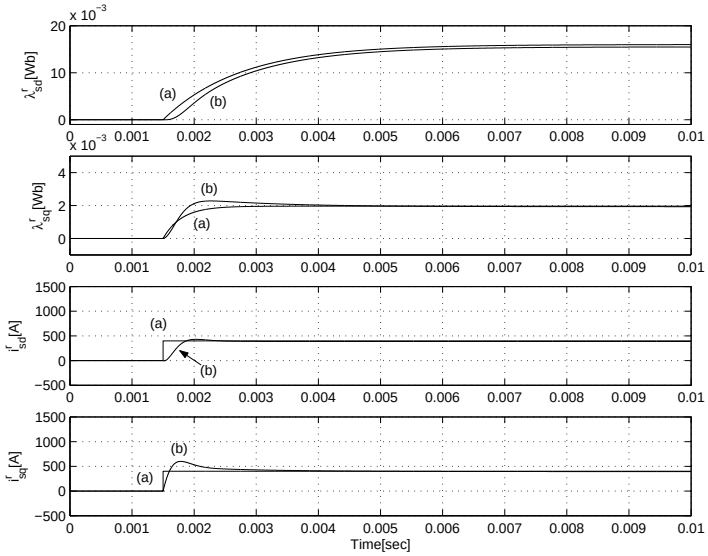

Fig. 3.6. Simulation: Direct and quadrature stator flux estimation and current regulation. Model includes rotor flux dynamics. 400 A peak current command at 35,000 rpm. λ^r_{sd}, λ^r_{sq}: (a) Estimated (b) Actual, i^r_{sd}, i^r_{sq}: (a) Command (b) Actual (from top)

3.3.2 Implementation in Discrete-time Domain

3.3.2.1 Discrete Machine Model

The continuous-time system model above in (3.8) and (3.9) can be represented in state space form as

$$\frac{d}{dt}\vec{x} = A(\omega_{re})\vec{x} + B\vec{u}. \tag{3.33}$$

Assuming essentially constant rotor velocity during a switching period T_s due to large inertia, the system equation can be treated as linear time-invariant for "fast" time scales. To implement a model-based controller in a digital processor, the continuous-time model can therefore be transformed to discrete-time difference equations as follows [44]:

$$\begin{aligned}\vec{x}(k+1) &= e^{AT_s}\vec{x}\,(k) + A^{-1}\left(e^{AT_s} - I\right)B\vec{u}(k) \\ &= F\vec{x}(k) + G\vec{u}(k).\end{aligned} \tag{3.34}$$

The matrix e^{AT_s} can be approximated by using the power series expansion method. Although the accuracy can be improved with a higher order approximation, this requires more processing time and memory space. This can create problems when executing the interrupt service routines, because generally the timing is very tight when it comes to a high-performance drive. Hence a first-order technique (i.e., Forward Euler) is typically used. However, it is appropriate to determine whether first-order techniques will be sufficient in this application.

$$e^{At} = I + At + \frac{(At)^2}{2!} + \frac{(At)^2}{2!} + \cdots = \sum_{n=0}^{\infty}\frac{(At)^n}{n!} \tag{3.35}$$

The system dynamics of a synchronous reluctance machine, as presented in (3.22) and (3.23), can be rewritten in matrix form as follows.

$$\begin{bmatrix} \lambda_{ad}^r(k+1) \\ \lambda_{aq}^r(k+1) \\ i_{sd}^r(k+1) \\ i_{sq}^r(k+1) \end{bmatrix} = \begin{bmatrix} f_{11} & f_{12} & f_{13} & f_{14} \\ f_{21} & f_{22} & f_{23} & f_{24} \\ f_{31} & f_{32} & f_{33} & f_{34} \\ f_{41} & f_{42} & f_{43} & f_{44} \end{bmatrix} \begin{bmatrix} \lambda_{ad}^r(k) \\ \lambda_{aq}^r(k) \\ i_{sd}^r(k) \\ i_{sq}^r(k) \end{bmatrix} + \begin{bmatrix} g_{11} & g_{12} \\ g_{21} & g_{22} \\ g_{31} & g_{32} \\ g_{41} & g_{42} \end{bmatrix} \begin{bmatrix} v_{sd}^r(k) \\ v_{sq}^r(k) \end{bmatrix} \tag{3.36}$$

The discrete-time system equation with the first order approximation of e^{AT_s} is

$$\vec{x}(k+1) = (I + AT_s)\vec{x}(k) + T_s B\vec{u}(k). \tag{3.37}$$

Hence, the matrix items in (3.36) can be given as

$$f_{11} = 1 - \frac{R_{rd}}{L_{rd}} T_s \tag{3.38}$$

$$f_{12} = 0 \tag{3.39}$$

$$f_{13} = \frac{R_{rd} M_d^2}{L_{rd}^2} T_s \tag{3.40}$$

$$f_{14} = 0 \tag{3.41}$$

$$f_{21} = 0 \tag{3.42}$$

$$f_{22} = 1 - \frac{R_{rq}}{L_{rq}} T_s \tag{3.43}$$

$$f_{23} = 0 \tag{3.44}$$

$$f_{24} = \frac{R_{rq} M_d^2}{L_{rq}^2} T_s \tag{3.45}$$

$$f_{31} = \frac{1}{L_{\ell s}} \frac{R_{rd}}{L_{rd}} T_s \tag{3.46}$$

$$f_{32} = \frac{\omega_{re}}{L_{\ell s}} T_s \tag{3.47}$$

$$f_{33} = 1 - \frac{1}{L_{\ell s}} \left(R_s + \frac{R_{rd} M_d^2}{L_{rd}^2} \right) T_s \tag{3.48}$$

$$f_{34} = \omega_{re} T_s \tag{3.49}$$

$$f_{41} = -\frac{\omega_{re}}{L_{\ell s}} T_s \tag{3.50}$$

$$f_{42} = \frac{1}{L_{\ell s}} \frac{R_{rq}}{L_{rq}} T_s \tag{3.51}$$

$$f_{43} = -\omega_{re} T_s \tag{3.52}$$

$$f_{44} = 1 - \frac{1}{L_{\ell s}} \left(R_s + \frac{R_{rq} M_q^2}{L_{rq}^2} \right) T_s \tag{3.53}$$

$$g_{11} = 0 \tag{3.54}$$

$$g_{12} = 0 \tag{3.55}$$

$$g_{21} = 0 \tag{3.56}$$

$$g_{22} = 0 \tag{3.57}$$

$$g_{31} = \frac{T_s}{L_{\ell s}} \tag{3.58}$$

$$g_{32} = 0 \tag{3.59}$$

$$g_{41} = 0 \tag{3.60}$$

$$g_{42} = \frac{T_s}{L_{\ell s}} \tag{3.61}$$

The second order equations are given as follows.

$$\vec{x}(k+1) = \left(I + AT_s + \frac{A^2 {T_s}^2}{2} \right) \vec{x}(k) + \left(T_s + \frac{A {T_s}^2}{2} \right) B\vec{u}(k) \tag{3.62}$$

The matrix items in (3.36) yields

$$f_{11} = \frac{T_s}{2}\frac{R_{rd}}{L_{rd}}\left\{\left(\frac{R_{rd}}{L_{rd}} + \frac{R_{rd}M_d^2}{L_{rd}^2}\frac{1}{L_{\ell s}}\right)T_s - 2\right\} + 1 \tag{3.63}$$

$$f_{12} = \frac{T_s^2}{2}\frac{R_{rd}M_d^2}{L_{rd}^2}\frac{1}{L_{\ell s}}\omega_{re} \tag{3.64}$$

$$f_{13} = -\frac{T_s}{2}\frac{R_{rd}M_d^2}{L_{rd}^2}\left[\left\{\frac{R_{rd}}{L_{rd}} + \left(R_s + \frac{R_{rd}M_d^2}{L_{rd}^2}\right)\frac{1}{L_{\ell s}}\right\}T_s - 2\right] \tag{3.65}$$

$$f_{14} = \frac{T_s^2}{2}\frac{R_{rd}M_d^2}{L_{rd}^2}\omega_{re} \tag{3.66}$$

$$f_{21} = \frac{T_s^2}{2}\frac{R_{rq}M_q^2}{L_{rq}^2}\frac{1}{L_{\ell s}}\omega_{re} \tag{3.67}$$

$$f_{22} = \frac{T_s}{2}\frac{R_{rq}}{L_{rq}}\left\{\left(\frac{R_{rq}}{L_{rq}} + \frac{R_{rq}M_q^2}{L_{rq}^2}\frac{1}{L_{\ell s}}\right)T_s - 2\right\} + 1 \tag{3.68}$$

$$f_{23} = -\frac{T_s^2}{2}\frac{R_{rq}M_q^2}{L_{rq}^2}\omega_{re} \tag{3.69}$$

$$f_{24} = -\frac{T_s}{2}\frac{R_{rq}M_q^2}{L_{rq}^2}\left[\left\{\frac{R_{rq}}{L_{rq}} + \left(R_s + \frac{R_{rq}M_q^2}{L_{rq}^2}\right)\frac{1}{L_{\ell s}}\right\}T_s - 2\right] \tag{3.70}$$

$$f_{31} = -\frac{T_s}{2}\frac{1}{L_{\ell s}}\left[\left\{\left(\frac{R_{rd}}{L_{rd}}\right)^2 + \frac{R_{rd}}{L_{rd}}\frac{1}{L_{ells}}\left(R_s + \frac{R_{rd}}{L_{rd}}\right) + \omega_{re}^2\right\}T_s - \frac{2R_{rd}}{L_{rd}}\right] \tag{3.71}$$

$$f_{32} = -\frac{T_s}{2}\frac{1}{L_{\ell s}}\omega_{re}\left\{\frac{1}{L_{\ell s}}\left(R_s + \frac{R_{rd}M_d^2}{L_{rd}^2}\right)T_s - 2\right\} \tag{3.72}$$

$$\begin{aligned} f_{33} = &\left\{\frac{R_{rd}}{L_{rd}}\frac{R_{rd}M_d^2}{L_{rd}^2}\frac{1}{L_{\ell s}} + \frac{1}{L_{\ell s}^2}\left(R_s + \frac{R_{rd}M_d^2}{L_{rd}^2}\right)^2 - \omega_{re}^2\right\}\frac{T_s^2}{2} \\ &-\frac{T_s}{2}\frac{2}{L_{\ell s}}\left(R_s + \frac{R_{rd}M_d^2}{L_{rd}^2}\right) + 1 \end{aligned} \tag{3.73}$$

$$f_{34} = \frac{T_s}{2}\omega_{re}\left[\left\{\frac{R_{rq}M_q^2}{L_{rq}^2} - \left(R_s + \frac{R_{rd}M_d^2}{L_{rd}^2}\right) - \left(R_s + \frac{R_{rq}M_q^2}{L_{rq}^2}\right)\right\}\frac{1}{L_{\ell s}}T_s + 2\right] \tag{3.74}$$

$$f_{41} = \frac{T_s}{2}\frac{1}{L_{\ell s}}\omega_{re}\left\{\frac{1}{L_{\ell s}}\left(R_s + \frac{R_{rq}M_q^2}{L_{rq}^2}\right)T_s - 2\right\} \tag{3.75}$$

$$f_{42} = -\frac{T_s}{2}\frac{1}{L_{\ell s}}\left[\left\{\left(\frac{R_{rq}}{L_{rq}}\right)^2 + \frac{R_{rq}}{L_{rq}}\frac{1}{L_{ells}}\left(R_s + \frac{R_{rq}}{L_{rq}}\right) + \omega_{re}^2\right\}T_s - \frac{2R_{rq}}{L_{rq}}\right] \tag{3.76}$$

$$f_{43} = -\frac{T_s}{2}\omega_{re}\left[\left\{\frac{R_{rd}M_d^2}{L_{rd}^2} - \left(R_s + \frac{R_{rd}M_d^2}{L_{rd}^2}\right) - \left(R_s + \frac{R_{rq}M_q^2}{L_{rq}^2}\right)\right\}\frac{1}{L_{\ell s}}T_s + 2\right] \tag{3.77}$$

$$f_{44} = \left\{\frac{R_{rq}}{L_{rq}}\frac{R_{rq}M_q^2}{L_{rq}^2}\frac{1}{L_{\ell s}} + \frac{1}{L_{\ell s}^2}\left(R_s + \frac{R_{rq}M_q^2}{L_{rq}^2}\right)^2 - \omega_{re}^2\right\}\frac{T_s^2}{2} - \frac{T_s}{2}\frac{2}{L_{\ell s}}\left(R_s + \frac{R_{rq}M_q^2}{L_{rq}^2}\right) + 1 \tag{3.78}$$

$$g_{11} = \frac{T_s^2}{2}\frac{1}{L_{\ell s}}\frac{R_{rd}M_d^2}{L_{rd}^2} \tag{3.79}$$

$$g_{12} = 0 \tag{3.80}$$

$$g_{21} = 0 \tag{3.81}$$

$$g_{22} = \frac{T_s^2}{2}\frac{1}{L_{\ell s}}\frac{R_{rq}M_d^2}{L_{rq}^2} \tag{3.82}$$

$$g_{31} = -\frac{T_s}{2}\frac{1}{L_{\ell s}}\left\{\frac{1}{L_{\ell s}}\left(R_s + \frac{R_{rd}M_d^2}{L_{rd}^2}\right)T_s - 2\right\} \tag{3.83}$$

$$g_{32} = \frac{T_s^2}{2}\frac{\omega_{re}}{L_{\ell s}} \tag{3.84}$$

$$g_{41} = -\frac{T_s^2}{2}\frac{\omega_{re}}{L_{\ell s}} \tag{3.85}$$

$$g_{42} = -\frac{T_s}{2}\frac{1}{L_{\ell s}}\left\{\frac{1}{L_{\ell s}}\left(R_s + \frac{R_{rq}M_q^2}{L_{rq}^2}\right)T_s - 2\right\} \tag{3.86}$$

3.3.2.2 Discrete Controller Implementation

Equations for discrete controller are derived as follows:

- First-order approximation of e^{AT}

$$\vec{\tilde{v}}_s^r(k) = R_s\vec{\tilde{i}}_s^r(k) - \omega_{re}[L_{\ell s}]\vec{\tilde{i}}_s^r(k) - \omega_{re}\vec{\tilde{\lambda}}_a^r(k-1) \tag{3.87}$$

- First-order flux estimator

$$\vec{\tilde{\lambda}}_a^r(k+1) = \vec{\tilde{\lambda}}_a^r(k) + \left(-\left[\frac{L_r}{R_r}\right]^{-1}\vec{\tilde{\lambda}}_a^r(k) + \left[R_r\left(\frac{M}{L_r}\right)^2\right]\vec{\tilde{i}}_s^r(k)\right)T_s \tag{3.88}$$

- Second-order approximation of e^{AT}

$$\begin{aligned}
\vec{\tilde{v}}_s^r(k) = &\left[\mathbf{I} - \frac{T_s}{2L_{\ell s}}\left[R_s + R_r\left(\frac{M}{L_r}\right)^2\right]\right]^{-1} \\
&\times\left\{R_s\vec{\tilde{i}}_s^r(k) - \frac{T_s}{2}\left(\left[\frac{R_s}{L_{\ell s}}\right]\left[R_s + R_r\left(\frac{M}{L_r}\right)^2\right] - L_{\ell s}\omega_{re}^2\right)\vec{\tilde{i}}_s^r(k) + \frac{T_s}{2}\omega_{re}^2\vec{\tilde{\lambda}}_a^r(k-1)\right. \\
&-\omega_{re}\mathbf{J}[L_{\ell s}]\vec{\tilde{i}}_s^r(k) + \frac{T_s}{2}\omega_{re}\mathbf{J}\left[R_s + R_r\left(\frac{M}{L_r}\right)^2\right]\vec{\tilde{i}}_s^r(k) - \omega_{re}\mathbf{J}\vec{\tilde{\lambda}}_a^r(k-1) \\
&\left.+\frac{T_s}{2}\omega_{re}\mathbf{J}[L_{\ell s}]^{-1}\left[R_s + R_r\left(\frac{M}{L_r}\right)^2\right]\vec{\tilde{\lambda}}_a^r(k-1) - \frac{T}{2}\omega_{re}\mathbf{J}\vec{\tilde{v}}_s^r(k-1)\right\}
\end{aligned} \tag{3.89}$$

- Second-order flux estimator

$$\begin{aligned}
\vec{\tilde{\lambda}}_a^r(k+1) = &\vec{\tilde{\lambda}}_a^r(k) - T_s\left[\frac{R_r}{L_r}\right]\vec{\tilde{\lambda}}_a^r(k) + \frac{T_s^2}{2}\left[\frac{R_r}{L_r}\right]\left(\left[\frac{R_r}{L_r}\right] + \left[\frac{R_r}{L_{\ell s}}\left(\frac{M}{L_r}\right)^2\right]\right)\vec{\tilde{\lambda}}_a^r(k) \\
&+T_s\left[R_r\left(\frac{M}{L_r}\right)^2\right]\vec{\tilde{i}}_s^r(k) - \frac{T_s^2}{2}\left(\left[\frac{R_r}{L_r}\right] + \left[R_s + R_r\left(\frac{M}{L_r}\right)^2\right][L_{\ell s}]^{-1}\right)\vec{\tilde{i}}_s^r(k)
\end{aligned}$$

$$+\frac{T_s^2}{2}\left[R_r\left(\frac{M}{L_r}\right)^2\right][L_{\ell s}]^{-1}\omega_{re}\vec{\hat{\lambda}}_a^r(k)+\frac{T_s^2}{2}\left[R_r\left(\frac{M}{L_r}\right)^2\right]\omega_{re}\vec{i}_s^r(k)$$
$$+\frac{T_s^2}{2}[L_{\ell s}]^{-1}\left[R_r\left(\frac{M}{L_r}\right)^2\right]\vec{v}_s^r(k) \tag{3.90}$$

For all significant operating points (minimum current, minimum flux-linkage and maximum power factor) of a synchronous reluctance machine with parameters shown in Table 3.1 with peak current command i_{spk} ranging from 0 to 1500 A and rotor speed from 25,000 to 50,000 rpm, it can be seen that the difference is less than 5%, thus utilizing the first-order model for this controller is a reasonable choice to conserve system resources with acceptable loss of accuracy.

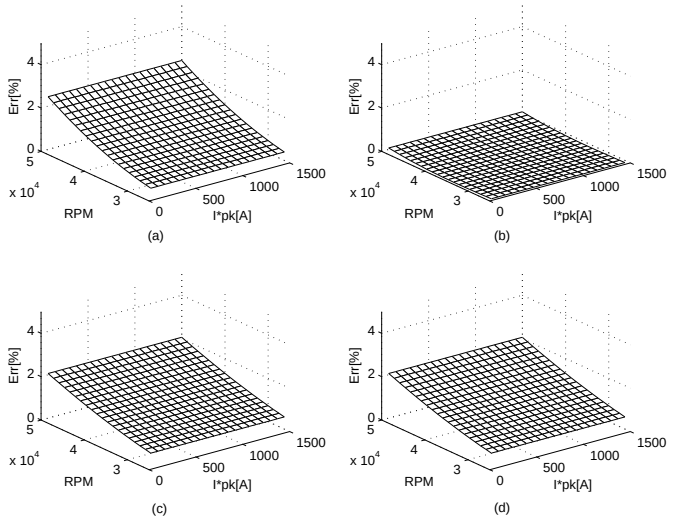

Fig. 3.7. Steady-state percent difference between the state variables of the first- and second-order approximated models when i_{spk} varies from 0 to 1500A and the rotor speed ranges from 25,000 to 50,000 rpm in minimum current operating points. (a) Direct flux estimation (b) Quadrature flux estimation (c) Direct voltage command (d) Quadrature voltage command

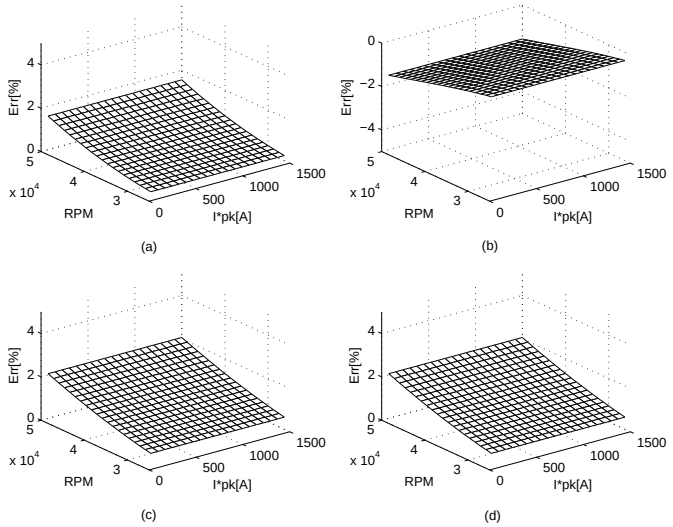

Fig. 3.8. Steady-state percent difference between the state variables of the first- and second-order approximated models when i_{spk} varies from 0 to 1500A and the rotor speed ranges from 25,000 to 50,000 rpm in minimum flux operating points. (a) Direct flux estimation (b) Quadrature flux estimation (c) Direct voltage command (d) Quadrature voltage command

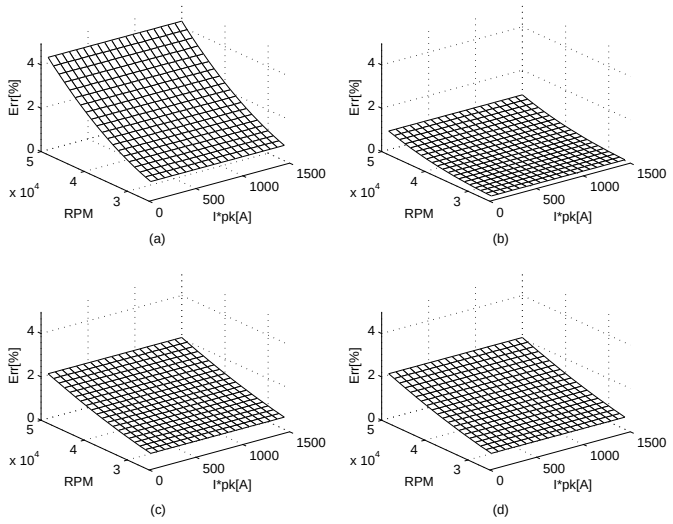

Fig. 3.9. Steady-state percent difference between the state variables of the first- and second-order approximated models when i_{spk} varies from 0 to 1500A and the rotor speed ranges from 25,000 to 50,000 rpm in maximum power factor operating points. (a) Direct flux estimation (b) Quadrature flux estimation (c) Direct voltage command (d) Quadrature voltage command

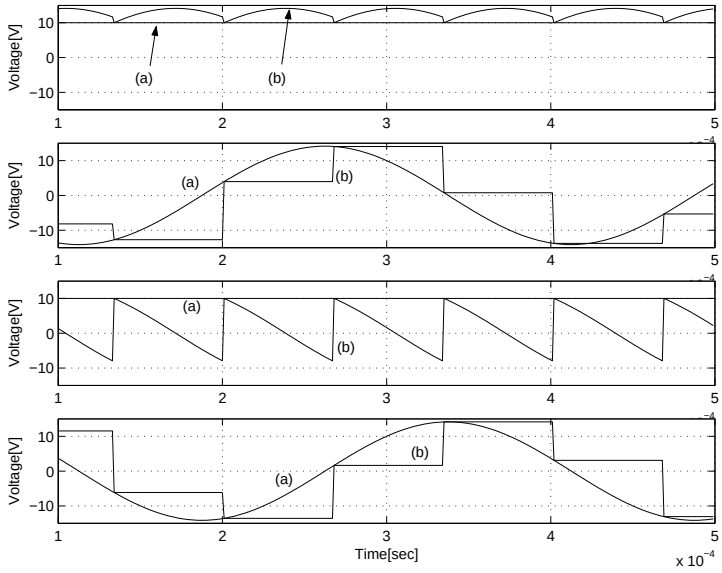

Fig. 3.10. Simulation: Direct- and quadrature-axis voltages at 50,000 rpm, 15 kHz Sampling. (a) Reference (b) Actual. From top: rotor reference frame direct-axis voltages, stator reference frame direct-axis voltages, rotor reference frame quadrature-axis voltages, stator reference frame quadrature-axis voltages

3.3.3 Influence of PWM Inverter

To verify the models, the system has been simulated in an ideal condition. Rotor reference frame voltage commands have been applied to the machine model directly, which means an ideal realization of the voltage commands. The effects of the PWM inverter have been omitted, and there has been no delay between controller and machine model. The current output can be therefore expected to be almost exactly same with the command, because the controller is an exact inverse model of the machine.

Axis and phase transformations are added between controller and machine model, and the effect of the discrete conversion and transformation on the rotor reference frame voltages are shown in Fig. 3.10. This makes the model closer to the real system, and current output will be deformed because the errors which these transformations generate become non-negligible when

the ratio of switching to output frequency ratio is low. Moreover, usually the PWM commands are applied to the inverter with one sampling delay when it is implemented in hardware. This is included in the controller model. However, the simulation has not considered practical factors such as PWM and dead time are not included.

3.3.4 Delay Compensation

Axis- and phase-transformations in the discrete-time domain cannot be ideally performed due to the continuous-time external system. The sample-and-hold effect in the stator reference frame generates disturbances in the rotor reference frame, which can be seen in Fig. 3.11. This disturbance could be neglected when the ratio of switching to fundamental frequency is large enough; however, this ratio cannot be sufficiently large in a high-speed system due to hardware limitations. Moreover, most hardware implementations require at least one sampling time delay to update the actual PWM command values. These delay factors make the estimated flux values and the actual voltage commands received by gate drive circuitry become significantly off from expected values, as shown in Fig. 3.12.

This can be solved by phase-shifting the angular velocity feedback information. By compensating the rotor position by $\frac{3\omega_{re}T_s}{2}$, as shown in Fig. 3.15, the phase angle in the controller can be synchronized to the actual angle. This phase shift corresponds to the average phase for the next sampling period after the update delay of PWM commands. The compensated command voltages and the simulation results with compensated commands are shown in Figs. 3.13 and 3.14, respectively.

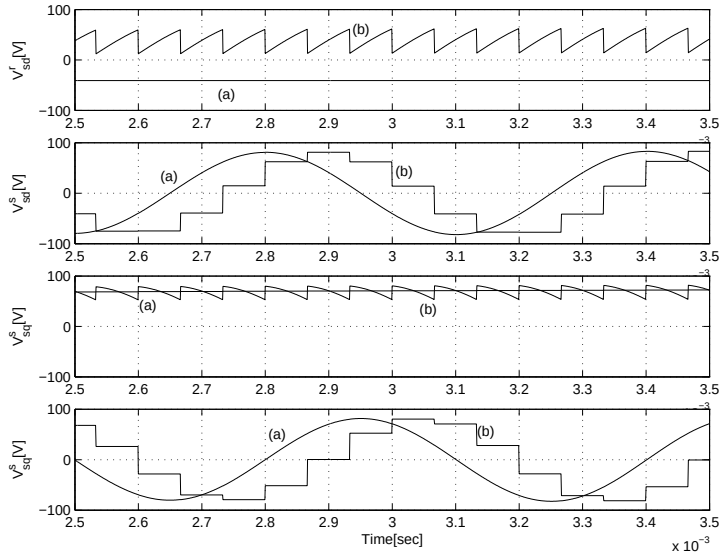

Fig. 3.11. Simulation: Disturbances in voltage commands by delay for the case of 15 kHz sampling and 35,000 rpm rotation with peak current command 400 A. v^r_{sd}, v^s_{sd}, v^r_{sq}, v^s_{sq}. Superscript '*s*' represents stator reference frame. (a) Ideal (b) Actual (from top)

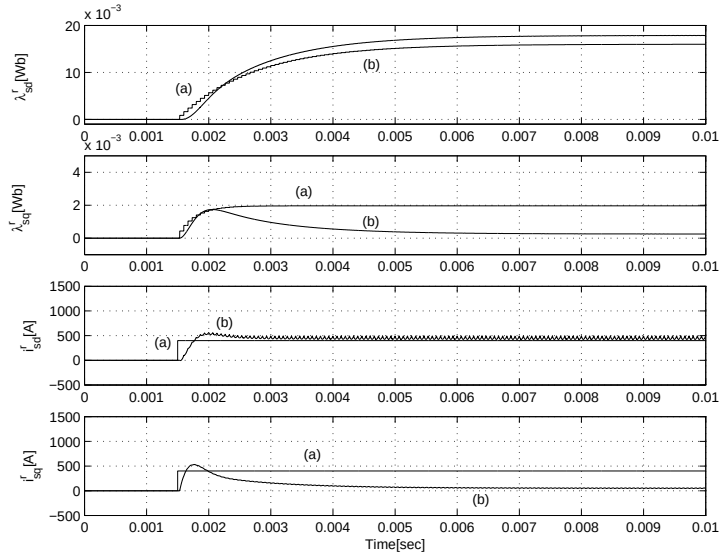

Fig. 3.12. Simulation: Erroneous flux estimation and current regulation by delay for the case of 15 kHz sampling and 35,000 rpm rotation with peak current command 400 A. λ^r_{sd}, λ^r_{sq}: (a) Estimated (b) Actual, i^r_{sd}, i^r_{sq}: (a) Command (b) Actual (from top)

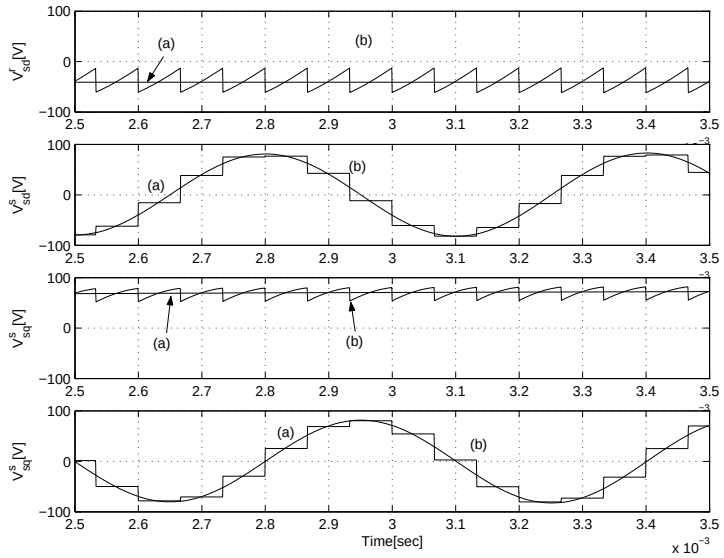

Fig. 3.13. Simulation: Phase-compensated voltage commands for the case of 15 kHz sampling and 35,000 rpm rotation with peak current command 400 A. v^r_{sd}, v^s_{sd}, v^r_{sq}, v^s_{sq}. Superscript '*s*' represents stator reference frame. (a) Ideal (b) Actual (from top)

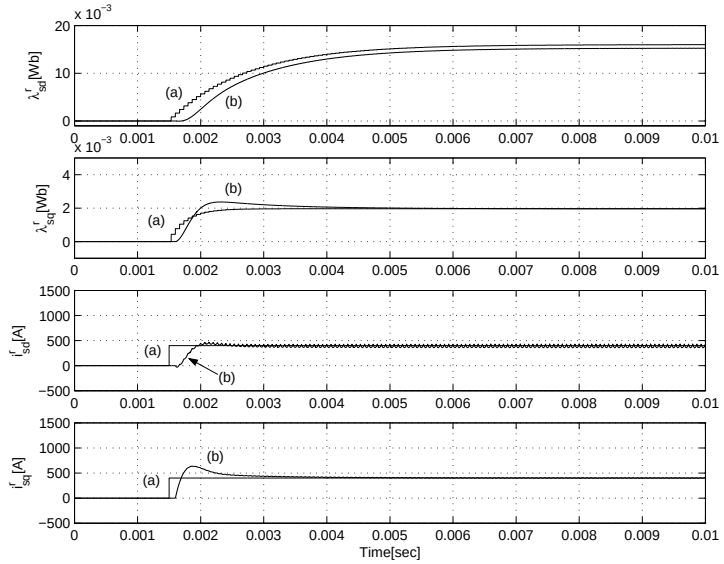

Fig. 3.14. Simulation: Compensated flux estimation and current regulation for the case of 15 kHz sampling and 35,000 rpm rotation with peak current command 400 A. λ^r_{sd}, λ^s_{sq}: (a) Estimated (b) Actual, i^r_{sd}, i^r_{sq}: (a) Command (b) Actual (from top)

3.3.5 Dead-Time Compensation

The model-based controller will be sensitive to any deviations of the system from the model, hence the dead-time effect will be one of those to be compensated. The dead-time associated with a phase leg of a three-phase inverter will alter the desired average-value output voltage of the phase as follows:

$$< v_{out}(t) >=< v_{command}(t) > -\frac{V_{bus} t_d}{T_s} \frac{i_{out}(t)}{|i_{out}(t)|}. \tag{3.91}$$

When calculating the command voltage in the rotor reference frame $\vec{v}_c^r$, we compensate for the fundamental component of the deadtime voltage using the desired current as follows [45]:

$$\vec{v}_c^r = \vec{v}_s^r + \frac{4V_{bus} t_d}{\pi T_s} \frac{\vec{i}_s^r}{i_{spk}}. \tag{3.92}$$

3.3.6 Stationary Feedback Regulator

As the winding resistance of high-speed machines is quite low, asymmetries in the machine and applied voltage, though small, can generate significant low-frequency or DC currents in the stator. This low frequency stationary current in turn will result in torque pulsations which fluctuate at almost synchronous frequency in the rotor reference frame. Additional resistive losses will be generated as well.

It may not be feasible to compensate this disturbance by increasing the bandwidth of the controller due to the practical limitations. An alternative approach would be to run a controller in the stationary frame as well as the field-oriented controller in the rotor reference frame. The

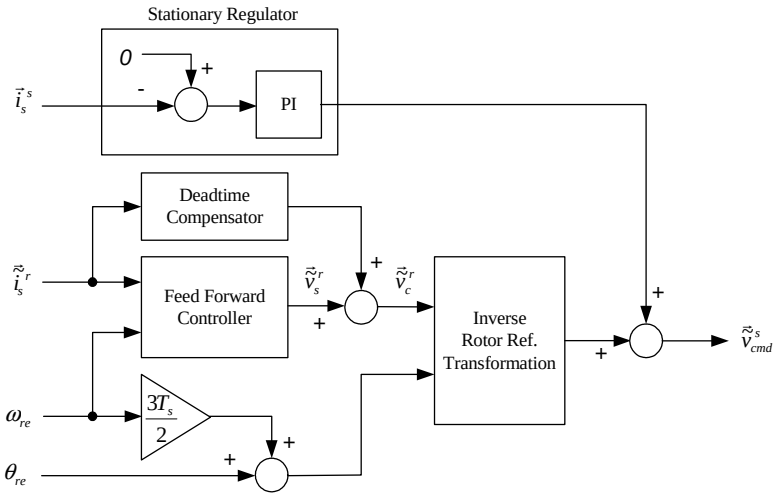

Fig. 3.15. Complete controller, including stationary regulator, dead-time and phase-delay compensation.

purpose of this stationary regulator is to eliminate these currents by generating a feedback response voltage which cancels the low-frequency voltage component mentioned above. A block diagram of the entire current regulator implementation is shown in Fig. 3.15.

Provided the fundamental electrical frequencies generated by the feedforward controller are much higher than the bandwidth of the stationary regulator, the stationary regulator achieves its purpose of eliminating the low frequency currents without interfering with the feedforward controller.

3.3.7 Modeling of Nonlinear Components

To model the machine more precisely, the nonlinear components such as main flux saturation and stator iron loss can be modeled as well. Also there is a cross-coupling between fluxes in the direct and quadrature axes. An equivalent circuit of a model which takes these nonlinear phenomena into consideration is shown in Fig. 3.16.

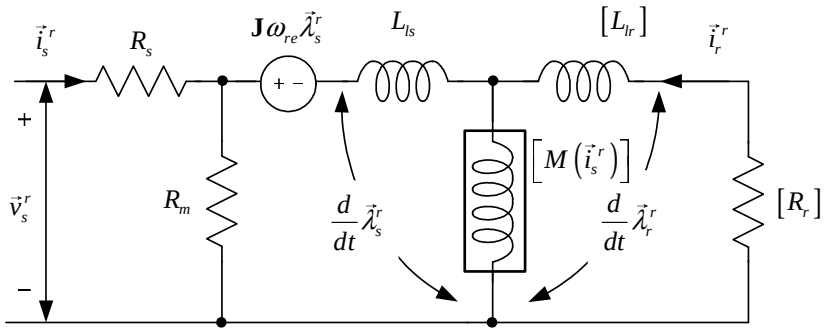

Fig. 3.16. Equivalent circuit of a synchronous reluctance machine, which takes the nonlinear components into consideration.

The resistor R_m represents the stator iron loss which affects amplitude and angle of the actual current vector. Furthermore, the inductance $M(\vec{i}_s^{\,r})$ represents the nonlinear inductance of the main flux path due to the saturation effect. Usually the nonlinear inductance is modeled as a function of stator current. Saturation can deteriorate the optimal performance due to incorrect flux estimation.

These nonlinear phenomena, and the compensation for them, have been studied in numerous researches [39, 40, 42]. The proposed model can easily accommodate the phenomena, as can be seen in Fig. 3.16. However, although consideration of these nonlinear effects into the model and proper compensation will surely improve the accuracy of the machine model and the performance of the controller, it is not uncommon to neglect these phenomena for practical control systems: stator iron loss can be negligible for some machines, the operating current range can result in essentially linear magnetic operation if the air-gap of the machine is relatively large, and measuring and compensating cross-coupling effects over a wide speed and current range can be difficult to implement with the limited computational resources available for real-time control.

3.4 Experimental Validation

The proposed model and controller were validated on a 120 kW, 4-pole synchronous reluctance machine. This machine is part of a flywheel energy storage system manufactured by Pentadyne Power Corporation that is capable of providing 120 kW of DC electrical power for up to 20 seconds. The system block diagram is shown in Fig. 3.20. The flywheel is suspended in vacuum by magnetic bearings. The rotor consists of alternating layers of a ferromagnetic and nonmagnetic material. A picture of the machine rotor and flywheel rim is shown in Fig. 3.17.

Figs. 3.18 and 3.19 show the direct and quadrature current during a 400 A peak current step command using the controller based upon a model without rotor flux dynamics, and the equivalent response using a model-based controller where the rotor flux dynamics has been included. The machine is running at the minimum current operating point, hence the rotor reference frame current commands are 282.84 A for both axes. The actual rotor reference frame currents in the figures are converted in the controller from the measured stator reference frame currents. The approximate rotor speed during these experiments was 35,000 rpm. Current overshoot can be clearly seen in the case where the rotor flux dynamics are neglected.

The current regulator is then used as an inner regulator in a bus voltage control algorithm, similar to that presented in [46]. The control logic initiates the regulation scheme when the DC bus voltage connected to the 3-phase inverter drops below a threshold, which is 500 V in the experiments of this chapter. Fig. 3.21 presents the bus voltage and DC power supplied by the flywheel system when the DC power supply to the system is disconnected and a 120 kW load is connected. The initial rotor speed during this experiment is 53,000 rpm. It can be seen that the voltage regulator responds quite well to the application of an instantaneous load.

Fig. 3.17. 4-pole synchronous reluctance rotor and flywheel rim.

3.5 Conclusion

A model for synchronous reluctance machines with solid conducting rotors has been proposed. It has been shown that the machine can be modeled more accurately if the rotor flux-linkage dynamics associated with the solid conducting rotor are included. Provided the model parameters agree well with the actual system, good performance can be achieved.

The most significant deviation between the system and the model is the saturation of the machine iron at high torque levels, which causes an effective reduction in the machine inductances, particularly the direct inductance. However, this problem can be resolved by the modification of the model to take the saturation into consideration. This will be addressed in a later chapter.

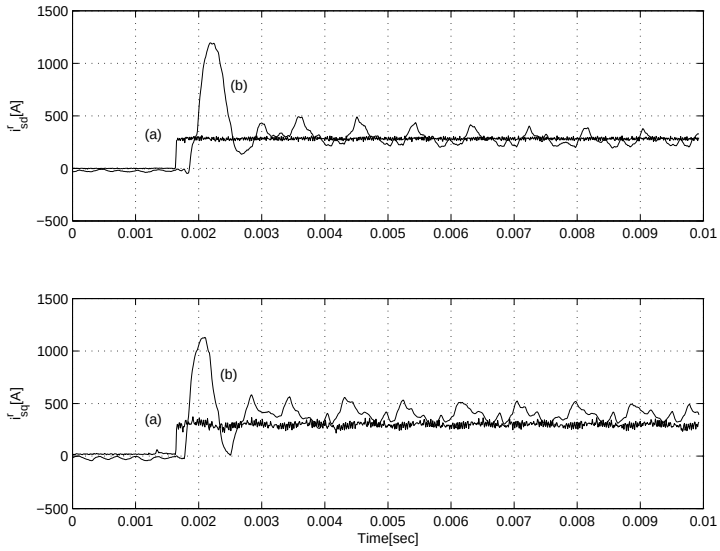

Fig. 3.18. Experiment: Direct and quadrature axis current regulation. Model does not include the rotor flux dynamics. 400 A peak current command at 35,000 rpm. Experiment is at minimum-current operating point of machine. i^r_{sd}, i^r_{sq}: (a) Command (b) Actual (from top)

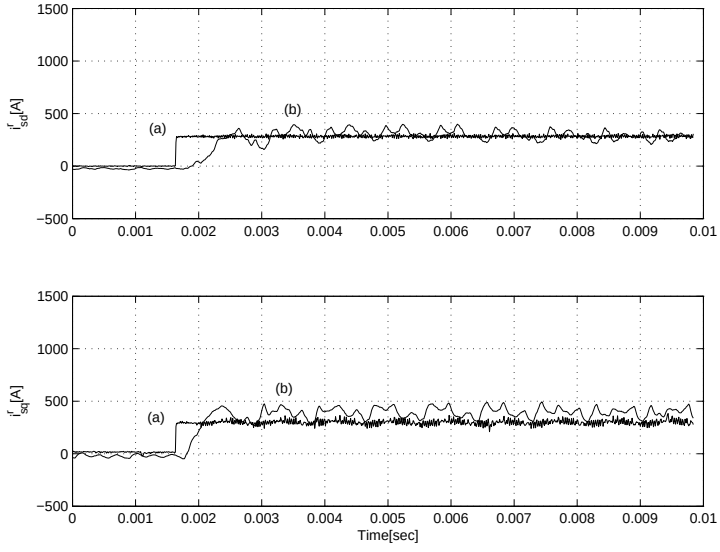

Fig. 3.19. Experiment: Direct and quadrature axis current regulation. Model includes the rotor flux dynamics. 400 A peak current command at 35,000 rpm. Experiment is at minimum-current operating point of machine. i^r_{sd}, i^r_{sq}: (a) Command (b) Actual (from top)

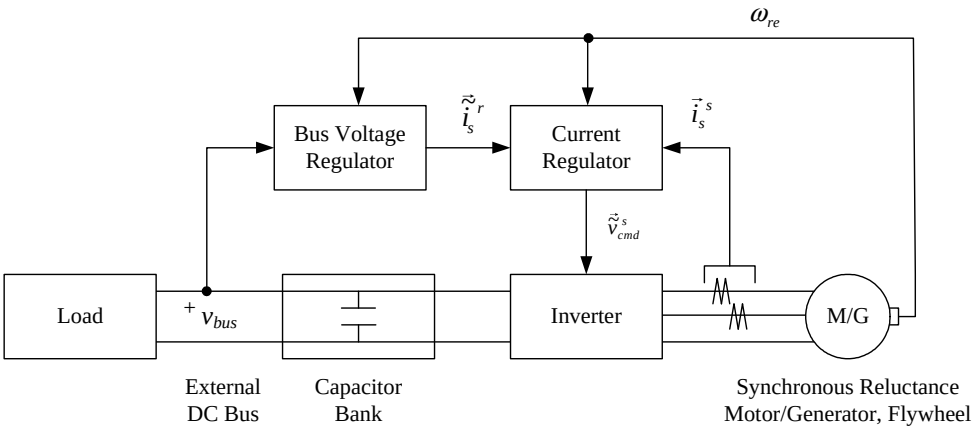

Fig. 3.20. Experimental setup of flywheel energy storage system

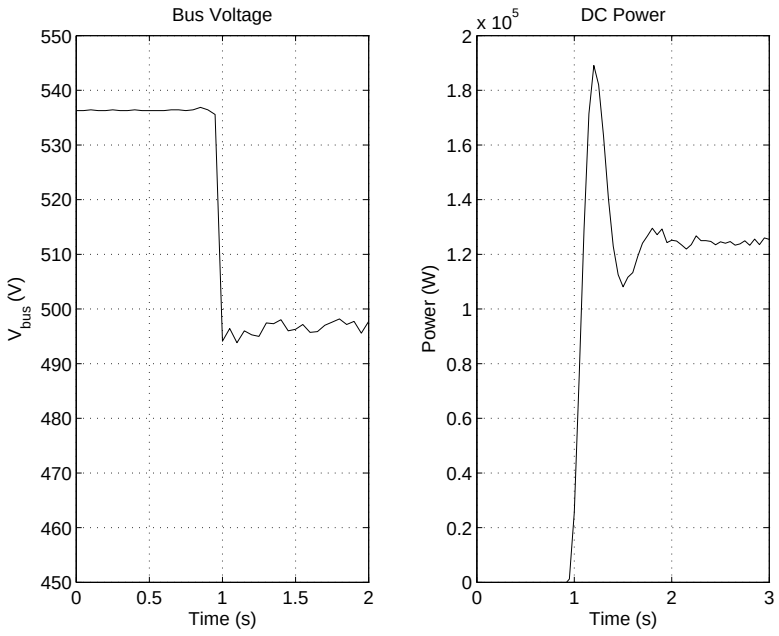

Fig. 3.21. Transient response of flywheel system when DC supply is disconnected and 120 kW load is connected. Left: bus voltage, right: DC power provided by flywheel unit

Chapter 4

Model Improvement Considering Nonlinear Magnetics

4.1 Introduction

The model of the synchronous reluctance machine in Chapter 3 is based on linear magnetic behavior, assuming that the flux linkage in the machine is linearly proportional to the excitation current. However, practical machines do not behave linearly and their nonlinear phenomena cannot be disregarded when dealing with the control of real machines. There are several nonlinear phenomena that make the linear modeling difficult, such as hysteresis, magnetic circuit topology or cross-coupling [47]. However, it is impractical to incorporate all of them in a single model, especially for purposes of control.

For the model-based feedforward controller proposed in Chapter 3, it is critical to estimate flux linkage precisely for accurate command voltage synthesis. The modeling of the nonlinear magnetic behavior becomes more important when an observer or an open-loop controller is adopted. Assuming linear magnetics for all operating conditions will deteriorate control performance, especially in the high- or low-end of the current range, due to flux saturation or remanent magnetization, respectively. A conceptual graph in Fig. 4.1 shows the nonlinear relationship between current and flux linkage with magnetic saturation and remanent magnetization.

In earlier works regarding the synchronous reluctance machine [36, 48], an ideal model, which did not take the nonlinear magnetics into account, was considered. More recent studies have focused on the issues of magnetic saturation [35, 40, 49–51]. As can be seen in Fig. 4.1,

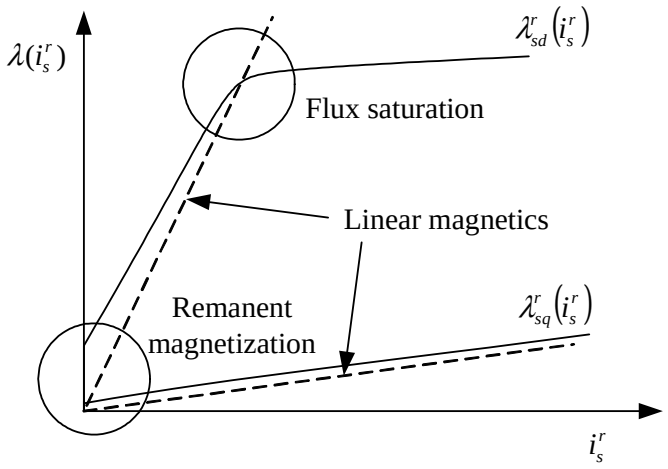

Fig. 4.1. Nonlinear magnetic behavior of direct- and quadrature-axis flux linkages

magnetic saturation decrease the flux linkage/current ratio considerably and consequently affects the performance of the machine. Major influences of the magnetic saturation can be [52]:

- Effects on accurate torque control,
- Effects on motor efficiency,
- Practical limits on available torque, and
- Parameter variations and resulting detuning effects.

For induction machines, it is necessary to keep the magnetizing current at the maximum level to obtain high dynamic performance out of the machine. However, for the synchronous reluctance machines, the level of magnetizing current for a given torque is generally determined by the designated operating point. It has also been reported in previous studies [25, 49, 53–55] that the current angles of operation were substantially different from those obtained for the ideal model if a machine is saturated. It can be clearly seen in Section 2.3 that all significant operating points are determined using direct- and quadrature-axis inductance, L_{sd} and L_{sq}. For a given

torque, the influence of the nonlinear magnetic behavior will become bigger as the portion of the magnetizing current is larger (e.g., the minimum current operating point).

The effect of remanent magnetization in a synchronous reluctance machine has not been a focus of research. Since it is the remaining flux in magnetic circuit when the external excitation is reduced to zero, it has generally been a topic for sensors or small motors. However, this phenomenon can also cause an error in the low current range for a model-based-controller driven machine. Especially it is true if the rotor material's coercive force is not low enough to neglect the effect of remanent magnetization.

When a linear relationship between current and flux-linkage is supposed and iron loss and other second-order effects are disregarded, the steady-state flux linkage expression is given as (2.24).

$$\begin{bmatrix} \lambda_{sd}^{r} \\ \lambda_{sq}^{r} \end{bmatrix} = \begin{bmatrix} L_{sd} & 0 \\ 0 & L_{sq} \end{bmatrix} \begin{bmatrix} i_{sd}^{r} \\ i_{sq}^{r} \end{bmatrix}$$

However, when nonlinear magnetics are considered, the flux-linkage expressions are functions of both direct- and quadrature-axis stator currents, as shown below.

$$\lambda_{sd}^{r} = f_{\lambda d}(i_{sd}^{r}, i_{sq}^{r}) \tag{4.1}$$

$$\lambda_{sq}^{r} = f_{\lambda q}(i_{sd}^{r}, i_{sq}^{r}) \tag{4.2}$$

Practically, the cross-coupling effect can be neglected in the normal load range because taking the cross-coupling into consideration is impractical and usually unnecessary for control purposes. Thus, the flux linkage-current relationship in the controller can be modeled as follows.

$$\begin{aligned} \lambda_{sd}^{r} &= f_{\lambda d}(i_{sd}^{r}) \\ \lambda_{sq}^{r} &= f_{\lambda q}(i_{sq}^{r}) \end{aligned} \tag{4.3}$$

It is possible to model both magnetic saturation and remanent magnetization with the same technique, because they are basically identical in terms of deviation from the linear current/flux linkage relationship. Techniques such as look-up tables [50, 56], rational fractions [57], and first-order models with time-constant [58] have been utilized to incorporate nonlinearities into the model.

For magnetic saturation, the following relationship can be utilized as well because quadrature-axis flux is not easily saturated due to the high reluctance [53].

$$\begin{aligned} \lambda_{sd}^{r} &= f_{\lambda d}(i_{sd}^{r}) \\ \lambda_{sq}^{r} &= L_{sq} i_{sq}^{r} \end{aligned} \tag{4.4}$$

A modified model for the proposed feedforward controller is presented in this chapter, where the effects of nonlinear magnetic behavior have been incorporated by using a nonlinear flux linkage estimator. This has been implemented by utilizing a nonlinear current-flux curve which can be determined from terminal voltage and current measurements on the unloaded synchronous reluctance machine under study. As well as the flux dynamics in the solid-type rotor,

this modification takes the magnetic flux saturation into consideration. The experimental results have shown the effect of magnetic saturation and validated the modified model.

4.2 Effect of Nonlinear Magnetics on Current Regulation

As well as the inaccurate operating point issue, a model-based controller will experience a current tracking problem if the magnetic nonlinearity is not considered, because the flux linkage estimation will become inaccurate.

The voltage equation of the synchronous reluctance machine has been given as (3.20).

$$\vec{v}_s^r = R_s\vec{i}_s^r + \omega_{re}\mathbf{J}\left(\left[L_s - \frac{M^2}{L_r}\right]\vec{i}_s^r + \vec{\lambda}_a^r\right) + \frac{d}{dt}\left(\left[L_s - \frac{M^2}{L_r}\right]\vec{i}_s^r + \vec{\lambda}_a^r\right)$$

Assuming a steady-state condition, the machine terminal voltage will be

$$\vec{v}_s^r = R_s\vec{i}_s^r + \omega_{re}\mathbf{J}\left(\left[L_s - \frac{M^2}{L_r}\right]\vec{i}_s^r + \vec{\lambda}_a^r\right). \tag{4.5}$$

Note that the rotor flux dynamics have been neglected here because of the steady-state assumption. We can simplify the expression as follows, because $L_r \gg L_{\ell r}$ in general, and hence $M\vec{i}_s^r \approx \vec{\lambda}_a^r$.

$$\vec{v}_s^r \approx R_s\vec{i}_s^r + \omega_{re}\mathbf{J}[L_s]\vec{i}_s^r \tag{4.6}$$

The proposed feedforward controller generates the command voltage based on (4.6). Hence, the $[L_s]$ values which are varying due to the nonlinear phenomena, will impose an effect on current regulation because the voltage is a function of the estimated flux.

The voltage command equation is determined as (4.8), including errors in the inductance values,

$$\vec{\tilde{v}}_s^r = \vec{v}_s^r + \Delta\vec{v}_s^r \tag{4.7}$$

$$= R_s\vec{\tilde{i}}_s^r + \omega_{re}\mathbf{J}[L_s + \Delta L_s]\vec{\tilde{i}}_s^r \tag{4.8}$$

hence the error of steady-state voltage command will be given as

$$\Delta\vec{v}_s^r = \omega_{re}\mathbf{J}[\Delta L_s]\ \vec{\tilde{i}}_s^r. \tag{4.9}$$

Note that stator resistance is assumed to be accurately measured. The voltage command, including error term, is applied to the machine and the voltage/current relationship at the machine terminal yields as follows from (4.6).

$$(R_s + \omega_{re}\mathbf{J}[L_s])\vec{\tilde{i}}_s^r + \omega_{re}\mathbf{J}[\Delta L_s]\vec{\tilde{i}}_s^r = (R_s + \omega_{re}\mathbf{J}[L_s])\vec{i}_s^r \tag{4.10}$$

Hence, the current regulation error will become

$$\Delta\vec{i}_s^r = -(R_s + \omega_{re}\mathbf{J}[L_s])^{-1}\omega_{re}\mathbf{J}[\Delta L_s]\vec{\tilde{i}}_s^r. \tag{4.11}$$

As can be seen in (4.11), the current tracking error is proportional to the inductance deviation. Considering the stator resistance is straightforward to measure from the machine terminal, the inaccurate flux linkage estimation due to the nonlinear magnetics will become a major source of the current tracking error.

4.3 Incorporating Nonlinear Magnetics into the Controller Model

4.3.1 Measurement of Flux Linkage

From the simplified voltage equation (4.6), flux linkages can be expressed as follows. They can be experimentally obtained by applying a series of voltages on one axis while zero voltage is applied to the other.

$$\lambda_{ad}^{r} = \frac{v_{sq}^{r} - R_s i_{sq}^{r}}{\omega_{re}} \tag{4.12}$$

$$\lambda_{aq}^{r} = \frac{v_{sd}^{r} - R_s i_{sd}^{r}}{-\omega_{re}} \tag{4.13}$$

Figs. 4.2 and 4.3 show the experimentally measured λ_{ad}^{r} and λ_{aq}^{r} of the synchronous reluctance machine that is utilized in the experiment in Section 3.4. Applied voltages (v_{sd}^{r},v_{sq}^{r}) have been (0 V, ± 250 V) and (± 120 V, 0 V), and the resulting currents are $\vec{i}_{sd}^{r} = \pm 400$ A and $\vec{i}_{sq}^{r} = \pm 700$ A for λ_{ad}^{r} and λ_{aq}^{r} measurement, respectively. The command voltages are used to calculated the inductance values, and the rotational speed is around 35,000 rpm.

The synchronous reluctance machine under study has not shown significant magnetic saturation in the tested range, due to its relatively large air gap. However, a remanent magnetization of the iron in the rotor of the machine is present, as can be seen in Figs. 4.2 and 4.3.

4.3.2 Controller Model Modification

In the proposed controller in Section 3.3.1, the flux linkage is estimated by (3.32).

$$\frac{d}{dt}\vec{\hat{\lambda}}_{a}^{r} = -\left[\frac{R_r}{L_r}\right]\vec{\hat{\lambda}}_{a}^{r} + \left[R_r\left(\frac{M}{L_r}\right)^2\right]\vec{i}_{s}^{r}$$

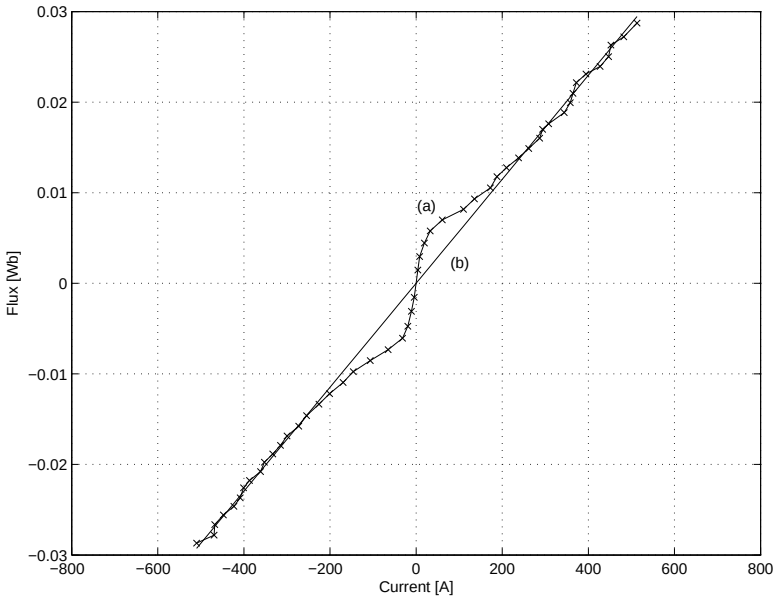

Fig. 4.2. (a) Experimentally measured direct-axis flux-linkage (b) Linear flux linkage

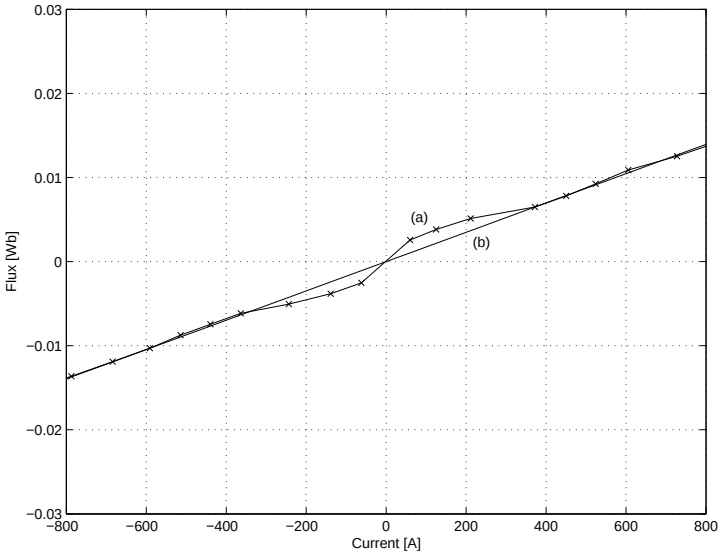

Fig. 4.3. (a) Experimentally measured quadrature-axis flux-linkage (b) Linear flux linkage

This estimated flux linkage has been compared with values determined from the experimentally measured data points in Figs. 4.2 and 4.3. Although the direct- and quadrature-axis flux linkage can be estimated quite well with a single inductance value for the higher current range, the differences are not negligible in the lower current range due to the remanent magnetization. Therefore the flux linkage estimator should be modified to incorporate the nonlinearity.

The rotor leakage inductance can be neglected because of the fact that the mutual inductance is much greater. Hence, (3.19) can be approximated as follows.

$$\vec{\lambda}_a^r = \left[\frac{M}{L_r}\right] \vec{\lambda}_r^r \tag{4.14}$$

$$\approx \vec{\lambda}_r^r \tag{4.15}$$

The rotor voltage equation can be rewritten as

$$\frac{d}{dt}\vec{\lambda}_r^r = -[R_r]\vec{i}_r^r \tag{4.16}$$

$$= [R_r](\vec{i}_s^r - \vec{i}_a^r) \tag{4.17}$$

$$\approx \frac{d}{dt}\vec{\lambda}_a^r \tag{4.18}$$

The flux-linkage estimator can therefore be given as

$$\frac{d}{dt}\hat{\lambda}_{ad}^r \approx R_r \left[\tilde{i}_{sd}^r - F_{id}(\hat{\lambda}_{ad}^r)\right] \tag{4.19}$$

$$\frac{d}{dt}\tilde{\lambda}_{aq}^r \approx R_r \left[\tilde{i}_{sq}^r - F_{iq}(\hat{\lambda}_{aq}^r)\right] \tag{4.20}$$

where,

$$\hat{i}_s^r = F_i(\hat{\lambda}_a^r) \tag{4.21}$$

$$F_i(\cdot) = f_\lambda^{-1}(\cdot) \tag{4.22}$$

The nonlinear flux-linkage equation $f_\lambda(\cdot)$ can be obtained from the experimentally measured flux linkages, which can be seen in Figs. 4.2 and 4.3. The equivalent circuit and block diagram of the modified flux estimator is shown in Figs. 4.4 and 4.5 (b).

Although the rotor leakage inductance is neglected to simplify the expression, this should result in little error, since the inductance is dominated by the mutual inductance for most machines. Also, this modification does not require any additional parameter measurement. Since the proposed model already takes the flux dynamics into consideration, this modification can model the flux behavior in the solid-rotor synchronous reluctance machine accurately with a straightforward procedure.

4.4 Experimental Validation

The proposed modification has been validated on a 120 kW, 4-pole synchronous reluctance machine which was utilized in the experiments of Chapter 3. The machine, and the proposed controller, are part of a flywheel energy storage system manufactured by Pentadyne Power Corporation that is capable of providing 120 kW of DC electrical power for up to 20 seconds over a speed range of 25,000 to 54,000 rpm.

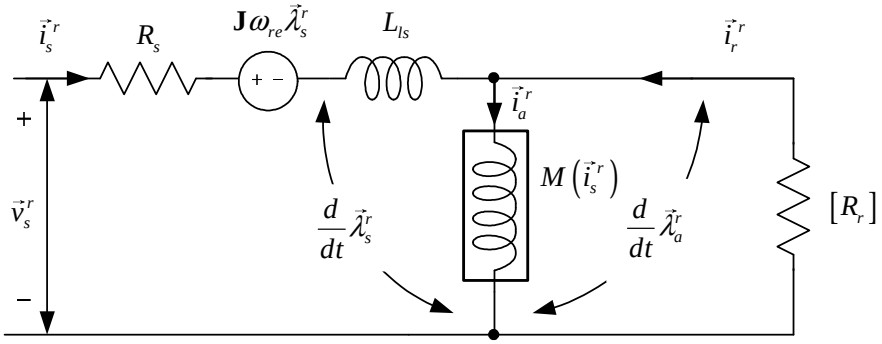

Fig. 4.4. Equivalent circuit model with a nonlinear flux linkage. Boxed inductance is nonlinear.

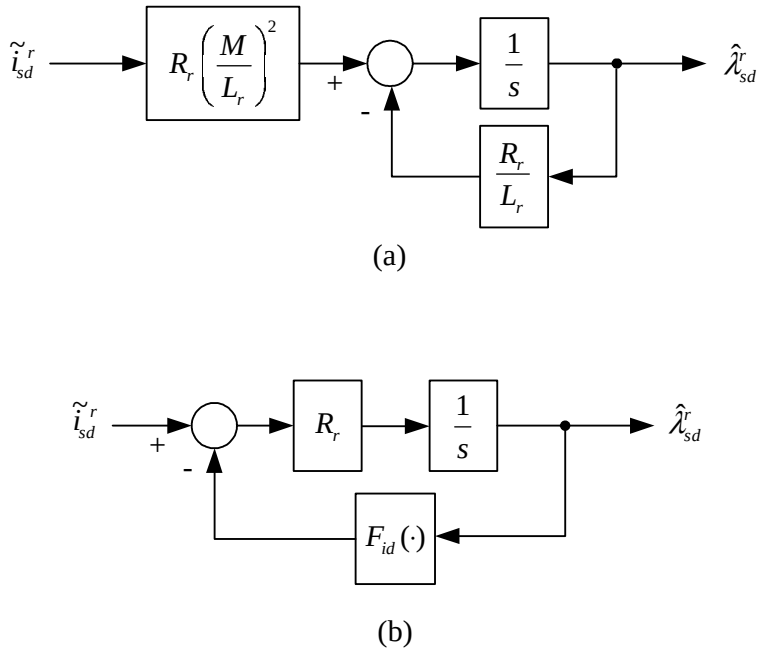

Fig. 4.5. Direct-axis flux estimator with (a) fixed inductance (b) variable inductance

If nonlinear magnetics are not taken into account in the controller, current regulation at low current levels is erroneous, as can be seen in Fig. 4.8, since the linear-magnetics-model-based controller with a fixed inductance fails to generate enough voltage command for the current range of $0 \sim 250$ A. This agrees well with the variation of flux linkage in that current range in Figs. 4.2 and 4.3. The machine currents track the command well when the command is increased to value around 250 A, because the controller parameters have been determined in that range.

Since it was difficult to fit the entire flux-linkage/current relationships with a single polynomial equation, piecewise equations in Table 4.1 have been utilized, and Figs. 4.6 and 4.7 shows the experimentally measured and estimated flux linkages. Although the result in Fig. 4.9 is not perfect because the estimated flux linkage curve that was utilized in the experiment is not precise enough to perfectly fit the experimentally measured one, the result shows that the current error of the $0 \sim 250$ A range is reduced and the remanent magnetization phenomena can be compensated by the proposed modification of the model. A better tracking performance can be expected with more accurate parameter measurement and estimation.

Table 4.1. Piecewise flux linkage equations

IF	$i^r_{sd} < 25A$	$\lambda^r_{sd} = (1.2 \times 10^{-5} \times i^r_{sd} + 4.62 \times 10^{-4}) \times i^r_{sd}$
ELSE IF	$i^r_{sd} < 110A$	$\lambda^r_{sd} = (1.77 \times 10^{-8} \times {i^r_{sd}}^2 - .85 \times 10^{-6} \times i^r_{sd} + 2.84 \times 10^{-4}) \times i^r_{sd}$
ELSE		$\lambda^r_{sd} = (-5.0 \times 10^{-8} \times i^r_{sd} + 7.5 \times 10^{-5}) \times i^r_{sd}$
IF	$i^r_{sq} < 300A$	$\lambda^r_{sq} = (2.93 \times 10^{-10} \times {i^r_{sd}}^2 - 2.05 \times 10^{-7} \times i^r_{sd} + 5.33 \times 10^{-5}) \times i^r_{sq}$
ELSE		$\lambda^r_{sq} = (17.5 \times 10^{-6}) \times i^r_{sq}$

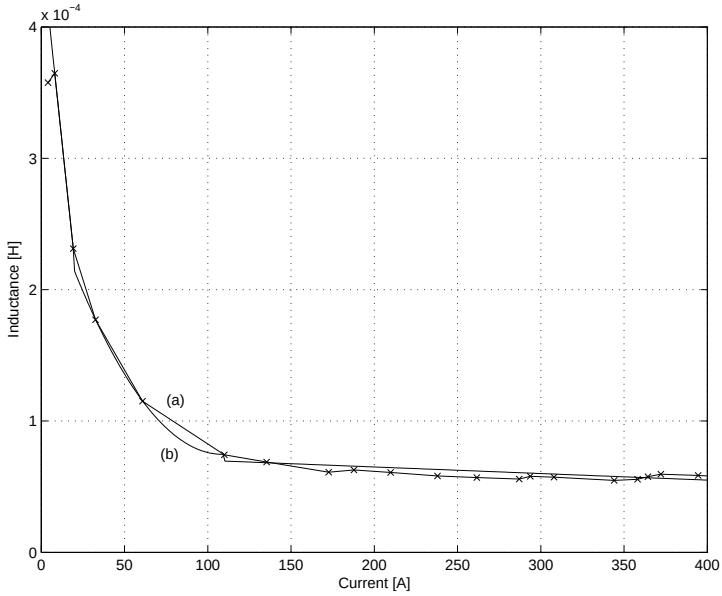

Fig. 4.6. L_{sd} curve: (a) Experimentally measured (data points x) (b) Estimated

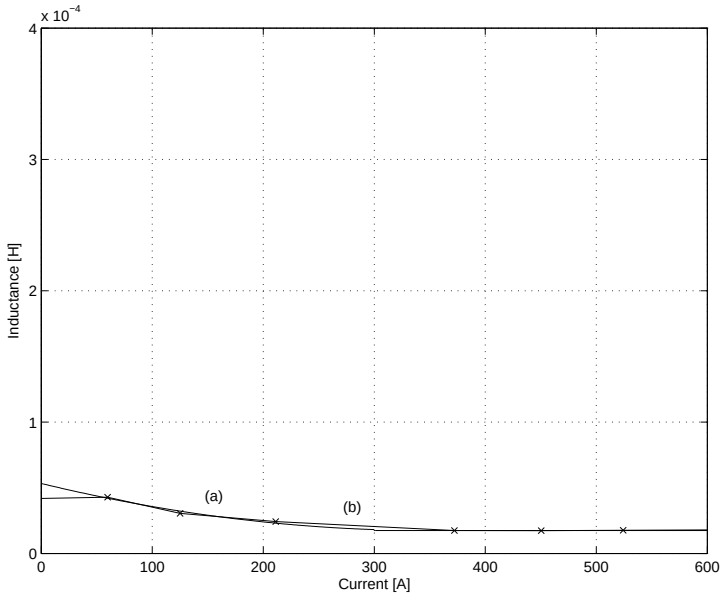

Fig. 4.7. L_{sq} curve: (a) Experimentally measured (data points x) (b) Estimated

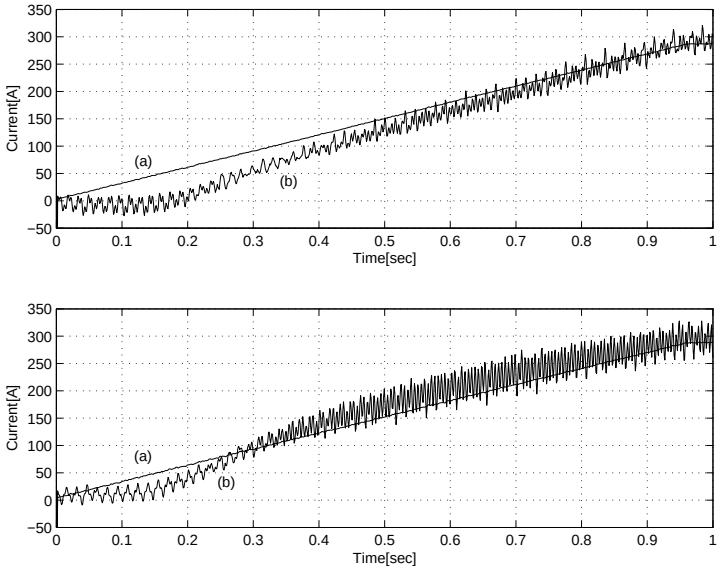

Fig. 4.8. Experiment: $0 \sim 300$ A ramp commands in rotor reference frame at 35,000 rpm. Linear-model-based controller. Upper: direct-axis, lower: quadrature-axis. (a) Command current $\tilde{i}_s^r$ (b) Actual current i_s^r

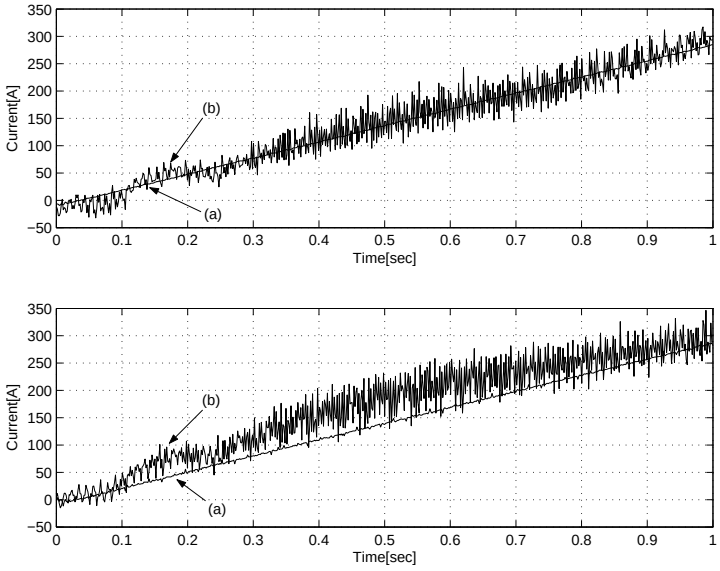

Fig. 4.9. Experiment: $0 \sim 300$ A ramp commands in rotor reference frame at 35,000 rpm. Nonlinear-model-based controller. Upper: direct-axis, lower: quadrature-axis. (a) Command current $\tilde{i}_s^r$ (b) Actual current i_s^r

4.5 Conclusion

A modification of the solid-rotor synchronous reluctance machine model to incorporate the nonlinear magnetic phenomena has been suggested in this chapter. The influence of nonlinear magnetics on the model-based controller has been investigated. Although the machine under study does not experience a significant saturation in its main flux path, it has been validated that the feedforward controller based on the proposed modified model can remove the current tracking error caused by the remanent magnetization. The suggested approach can apparently be applicable to compensate magnetic saturation with extended nonlinear equations including the saturated range.

Chapter 5

Feedback Compensation for Feedforward Control

5.1 Introduction

Feedforward current regulators for electric machines are one solution for high-speed applications, as typical feedback regulators can be problematic in field-oriented control due to the speed-dependence of the machine dynamics. A sufficiently accurate model of the machine can make a feedforward controller a reasonable approach, as the stability issue becomes avoidable due to the inherently stable machine dynamics. It has been shown that the conventional model of the synchronous reluctance machine, which does not consider the rotor flux dynamics, can create a current overshoot during transients when used in a current regulator, as the predicted back-emf is much higher than the actual back-emf of the machine. This makes it problematic to utilize the conventional model to design a model-based controller for a machine with a conducting rotor.

However, even if the model utilized in the feedforward controller describes the machine well, the feedforward controller relies heavily upon accurate knowledge of the parameters for good performance. Practically it is hard to measure all parameters exactly. Some of them may be difficult to measure, and initially-measured parameters can easily vary with operating conditions such as temperature and the nonlinear magnetic properties of the iron in the machine. A feedforward-controlled system generates inaccurate output if the parameters are not correct, and does not take into account unmodeled dynamics or disturbances.

In this chapter, a hybrid controller which incorporates a feedback PI compensator into a feedforward controller to improve the performance and robustness of current regulation for a high-speed solid-rotor synchronous reluctance machine is proposed. The machine current tracking error caused by the parameter mismatch is mathematically analyzed, and is utilized to dynamically compensate the estimated flux linkage to eliminate the steady state error in current regulation. Stability analysis is also performed, and it will be shown that the regulation performance and robustness of the system are improved.

The proposed controller yields an improved performance for a fast-changing torque command with the model, as well as good tracking performance from the PI regulator. This is desirable for applications such as a flywheel energy storage system, because a fast response is an important performance factor of flywheel-based or flywheel-battery hybrid UPS systems. The proposed controller has been experimentally validated with a solid-rotor synchronous reluctance motor/generator based flywheel energy storage system.

5.2 Full-Order Machine Model with Rotor Dynamics

5.2.1 Continuous-time Model and Controller Implementation

The feedforward controller which is utilized in this paper is based on the machine model presented in Section 3.3.1. The machine is modeled in the rotor reference frame by direct and quadrature windings, and is similar to the case of squirrel-cage induction machines, yet includes a magnetic saliency of the rotor. The complete dynamic equations for the system are therefore

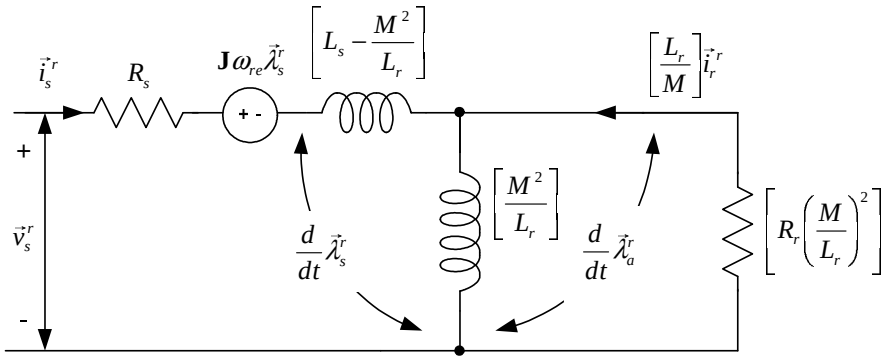

Fig. 5.1. Equivalent circuit model of a synchronous reluctance machine in rotor reference frame

given by:

$$\frac{d\vec{\lambda}_a^r}{dt} = -\left[\frac{L_r}{R_r}\right]^{-1}\vec{\lambda}_a^r + \left[R_r\left(\frac{M}{L_r}\right)^2\right]\vec{i}_s^r \tag{5.1}$$

$$\begin{aligned}\frac{d\vec{i}_s^r}{dt} = &\left[L_s - \frac{M^2}{L_r}\right]^{-1}\left\{\vec{v}_s^r - \left[R_s + R_r\left(\frac{M}{L_r}\right)^2\right]\vec{i}_s^r\right.\\ &\left. - \omega_{re}\mathbf{J}\left(\left[L_s - \frac{M^2}{L_r}\right]\vec{i}_s^r + \vec{\lambda}_a^r\right) + \left[\frac{L_r}{R_r}\right]^{-1}\vec{\lambda}_a^r\right\}\end{aligned} \tag{5.2}$$

where,

$$\vec{\lambda}_a^r = \left[\frac{M}{L_r}\right]\vec{\lambda}_r^r. \tag{5.3}$$

Unlike equivalent-circuit-based models in the previous studies [39–41], this model takes the dynamics of the rotor flux linkage into account, and therefore better represents the flux behavior in the machine.

A feedforward controller has been suggested based on the proposed model in Chapter 3 and it has been shown that sufficient accuracy can be achieved by approximating the steady-state

stator voltage as follows:

$$\vec{\tilde{v}}_s^r \approx R_s \vec{\tilde{i}}_s^r + \omega_{re}\mathbf{J}\left\{L_{\ell s}\vec{\tilde{i}}_s^r + \vec{\hat{\lambda}}_a^r\right\}. \tag{5.4}$$

The estimated flux linkage vector $\vec{\hat{\lambda}}_a^r$ can be determined by numerically integrating (5.1) using command currents.

$$\vec{\hat{\lambda}}_a^r = \int_{-\infty}^{t} -\left[\frac{L_r}{R_r}\right]^{-1}\vec{\hat{\lambda}}_a^r + \left[R_r\left(\frac{M}{L_r}\right)^2\right]\vec{\tilde{i}}_s^r dt \tag{5.5}$$

A block diagram of the feedforward controller is shown in Fig. 3.4. K_d determines the synchronous reluctance machine's operating point [28].

5.2.2 Error Caused by Parameter Mismatch

The performance of the feedforward controller relies on the accuracy of its parameters because it is model-based. For the model used in the controller, three sets of direct and quadrature parameters and a scalar parameter are required:

- Rotor time constants $\left[\frac{L_r}{R_r}\right]$,
- Rotor "excitation" resistance $\left[R_r\left(\frac{M}{L_r}\right)^2\right]$,
- "Leakage" Inductance $\left[L_s - \frac{M^2}{L_r}\right]$, and
- Stator resistance R_s

Among these, it has been assumed that $\left[L_s - \frac{M^2}{L_r}\right]$, which can be approximated by $L_{\ell s}$, and R_s have exact values. However, other parameters require time-consuming procedures to

determine accurately and, moreover, the parameters $[L_r]$, $[M]$ and $[R_r]$ will vary due to magnetic saturation in the flux path and rotor temperature variation, respectively.

(5.5) is used to estimate the flux linkage. If an error exists in the time constant and excitation resistance, the estimated flux linkage will have the additive error term.

$$\vec{\hat{\lambda}}_a^r = \vec{\hat{\lambda}}_{a0}^r - \Delta\vec{\hat{\lambda}}_a^r \tag{5.6}$$

$$= \int_{-\infty}^{t} - \left[\frac{R_r}{L_r} + \Delta_1\right]\left(\vec{\hat{\lambda}}_{a0}^r + \Delta\vec{\lambda}_a^r\right) + \left[R_r\left(\frac{M}{L_r}\right)^2 + \Delta_2\right]\vec{\hat{i}}_s^r\, dt \tag{5.7}$$

where $\vec{\hat{\lambda}}_{a0}^r$ represents the right amount of the flux linkage for the given current command. Then the error in the flux linkage estimation can be separated as

$$\Delta\vec{\hat{\lambda}}_a^r = - \int_{-\infty}^{t} - [\Delta_1]\,\vec{\hat{\lambda}}_{a0}^r - \left[\frac{R_r}{L_r} + \Delta_1\right]\Delta\vec{\lambda}_a^r + [\Delta_2]\,\vec{\hat{i}}_s^r\, dt. \tag{5.8}$$

Differentiating yields:

$$\frac{d}{dt}\Delta\vec{\lambda}_a^r = [\Delta_1]\,\vec{\hat{\lambda}}_{a0}^r + \left[\frac{R_r}{L_r} + \Delta_1\right]\Delta\vec{\lambda}_a^r - [\Delta_2]\,\vec{\hat{i}}_s^r. \tag{5.9}$$

Assuming steady-state operation, the error terms of the flux linkage estimation become dc offsets. However, it is difficult to tell which parameter is wrong from the output because the errors are combination of parameters, current and flux linkage.

$$\Delta\vec{\lambda}_a^r = \left[\frac{R_r}{L_r} + \Delta_1\right]^{-1}\left([\Delta_1]\,\vec{\hat{\lambda}}_{a0}^r - [\Delta_2]\,\vec{\hat{i}}_s^r\right). \tag{5.10}$$

When incorrectly estimated flux linkage values $\hat{\vec{\lambda}}_a^r$ are utilized to calculate command voltage as in (5.4), an erroneous command voltage $\vec{\hat{v}}_s^r$ is generated.

$$\vec{\hat{v}}_s^r = \vec{v}_s^r + \Delta\vec{v}_s^r \tag{5.11}$$

$$= R_s\vec{\hat{i}}_s^r + \omega_{re}\mathbf{J}\left(\left[L_s - \frac{M^2}{L_r}\right]\vec{\hat{i}}_s^r + \hat{\vec{\lambda}}_a^r\right) \tag{5.12}$$

This voltage error will result in a stator current error. The relationship between flux linkage estimation and the current can be determined from the command values in (5.12) and the actual values from the command in (5.4), and the steady-state error of the machine current caused by mismatched parameters can be represented as follows.

$$\Delta\vec{i}_s^r = \left(R_s\mathbf{I} + \omega_{re}\mathbf{J}\left[L_s - \frac{M^2}{L_r}\right]\right)^{-1}\omega_{re}\mathbf{J}\Delta\vec{\lambda}_a^r \tag{5.13}$$

The following experimental plots show the effect of the parameter error on current regulation. The time constant $\left[\frac{L_r}{R_r}\right]$ and rotor excitation resistance $\left[R_r\left(\frac{M}{L_r}\right)^2\right]$ has been intentionally changed to have 25% error. It can be seen in Figs. 5.2-5.4 that the actual current magnitude is considerably larger than the controller's calculation due to the erroneous parameters and the error is increased as the generating power gets higher. It should be noted that the required power can be generated even with the tracking error because the bus voltage controller changes the current peak command to maintain the bus voltage. However, inverter trip or controller output saturation will be happening at a lower power command than designed.

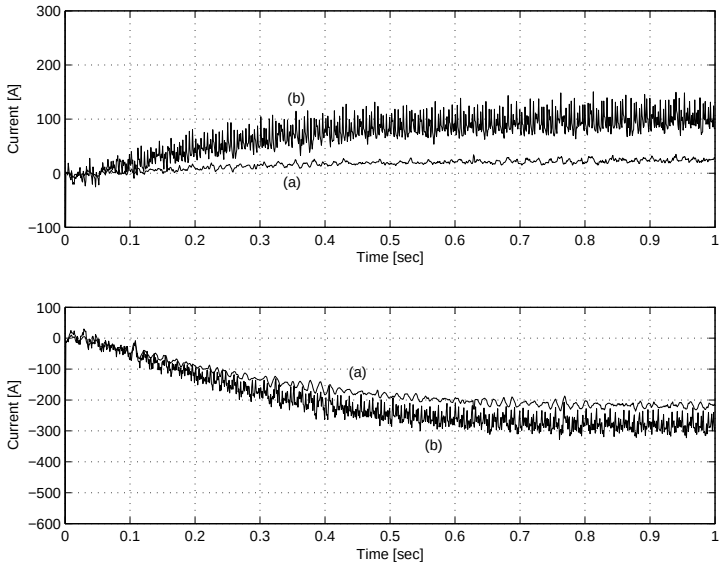

Fig. 5.2. Experiment: 24 kW discharge on minimum flux linkage operating point at 50,000 rpm. Time constant and excitation resistance have 25% error, respectively. Current commands are supplied by bus voltage regulator. (a) Command current $\tilde{i}_s^r$ (b) Actual current i_s^r

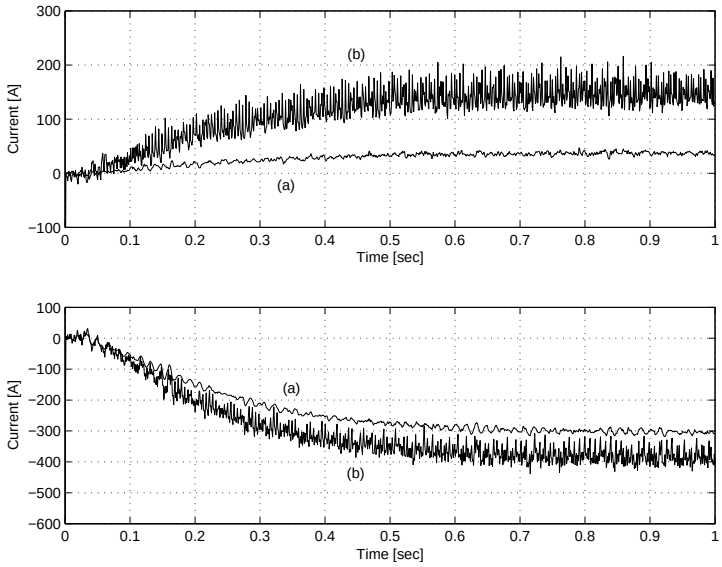

Fig. 5.3. Experiment: 42 kW discharge on minimum flux linkage operating point at 50,000 rpm. Time constant and excitation resistance have 25% error, respectively. Current commands are supplied by bus voltage regulator. (a) Command current $\tilde{i}_s^r$ (b) Actual current i_s^r

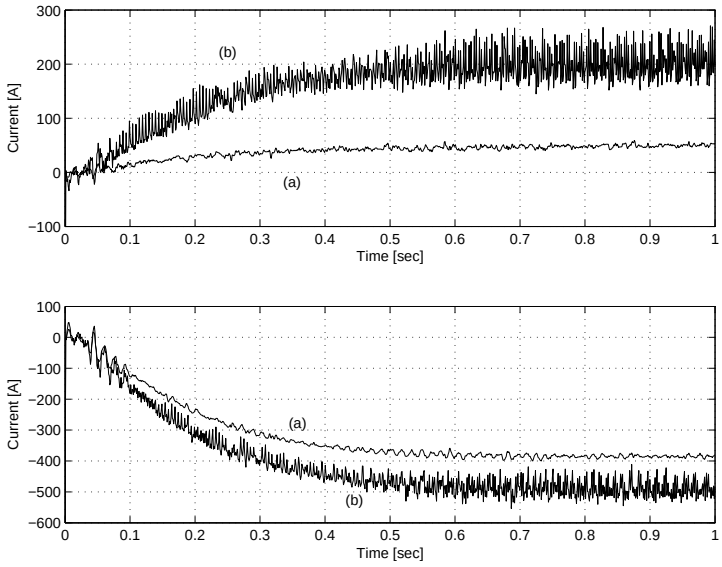

Fig. 5.4. Experiment: 64 kW discharge on minimum flux linkage operating point at 50,000 rpm. Time constant and excitation resistance have 25% error, respectively. Current commands are supplied by bus voltage regulator. (a) Command current $\tilde{i}_s^r$ (b) Actual current i_s^r

5.3 PI Feedback Compensator

In steady state, the error of the current is proportional to that of the estimated flux linkage, which comes in turn from parameter errors, as can be seen in (5.13). Although it is difficult to tune each parameter on-line from the current measurements, due to the fact that the estimated flux linkage is a combination of coupled variables and parameters, this current error can be utilized to correct the erroneous flux linkage.

(5.13) can be rewritten as follows:

$$\Delta\vec{\lambda}_a^r = \left(-R_s {\omega_{re}}^{-1}\mathbf{J} + \left[L_s - \frac{M^2}{L_r} \right] \right) \Delta\vec{i}_s^r \tag{5.14}$$

Therefore, compensation could then be made on the output of the flux linkage estimator based on the current error, as shown in Fig. 5.5. Thus, the compensated command voltages are given

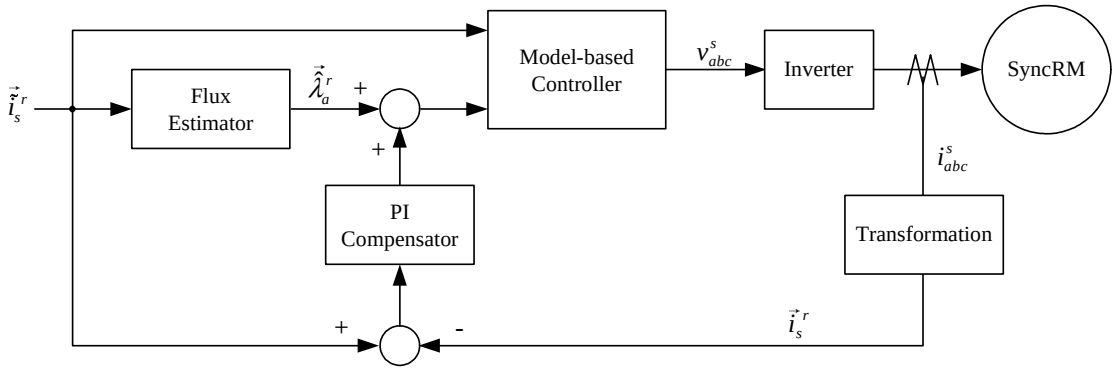

Fig. 5.5. Block diagram of feedback compensated model-based control system

as follows from (5.4).

$$\vec{\tilde{v}}_s^r = R_s \vec{\tilde{i}}_s^r + \omega_{re}\mathbf{J}\left\{\left[L_s - \frac{M^2}{L_r}\right]\vec{\tilde{i}}_s^r + \vec{\tilde{\lambda}}_a^r + \Delta\vec{\lambda}_a^r\right\} \tag{5.15}$$

However, using (5.14) as a compensation term is inappropriate for a few reasons. It will generate a large overshoot during the transient operation for fast changing torque commands, such as a step command, because this simple feedback does not take the flux dynamics into consideration. Also, a purely proportional control scheme cannot completely eliminate the steady-state error. Hence, a legitimate solution would be to implement a PI compensator. The flux linkage compensation will be given as follows,

$$\Delta\vec{\lambda}_a^r = \left(K_p + \frac{K_i}{s}\right)\Delta\vec{i}_s^r - R_s\omega_{re}^{-1}\mathbf{J}\Delta\vec{i}_s^r \tag{5.16}$$

where the term $R_s\omega_{re}^{-1}\mathbf{J}\Delta\vec{i}_s^r$ is included in an attempt to decouple the direct and quadrature dynamics. In order to reduce the number of states in the system, the integral part of the PI

regulator can be integrated into the flux estimator as follows:

$$\vec{\hat{\lambda}}_a^r = \int_{-\infty}^{t} -\left[\frac{L_r}{R_r}\right]^{-1} \vec{\hat{\lambda}}_a^r + \left[R_r\left(\frac{M}{L_r}\right)^2\right] \vec{i}_s^r + K_i \Delta \vec{i}_s^r dt \tag{5.17}$$

5.4 Stability Analysis

5.4.1 Feedforward Control

The state variables of the machine are defined as

$$\vec{x} = \begin{bmatrix} \lambda_{ad}^r & \lambda_{aq}^r & i_{sd}^r & i_{sq}^r \end{bmatrix}^T, \tag{5.18}$$

and the machine dynamics equations of (5.1) and (5.2) can be represented in matrix form, as shown in (5.19), (5.20) and (5.21).

$$\mathbf{A} = \begin{bmatrix} -\left[\frac{L_r}{R_r}\right]^{-1} & \left[Rr\left(\frac{M}{L_r}\right)^2\right] \\ -\left[L_s - \frac{M^2}{L_r}\right]^{-1}\left\{\left[\frac{L_r}{R_r}\right]^{-1} - \omega_{re}\mathbf{J}\right\} & -\left[L_s - \frac{M^2}{L_r}\right]^{-1}\left\{\left[R_s + R_r\left(\frac{M}{L_r}\right)^2\right] - \omega_{re}\mathbf{J}\left[L_s - \frac{M^2}{L_r}\right]\right\} \end{bmatrix} \tag{5.19}$$

$$\mathbf{B} = \begin{bmatrix} \mathbf{0} & \left[L_s - \frac{M^2}{L_r}\right]^{-1} \end{bmatrix}^T \tag{5.20}$$

$$\mathbf{C} = \begin{bmatrix} \mathbf{0} & \mathbf{I} \end{bmatrix} \tag{5.21}$$

From the controller equations represented in (5.4) and(5.5), the following matrix notation has been used:

$$\hat{\mathbf{A}} = -\left[\frac{L_r}{R_r}\right]^{-1} \tag{5.22}$$

$$\hat{\mathbf{B}} = \left[R_r\left(\frac{M}{L_r}\right)^2\right] \tag{5.23}$$

$$\hat{\mathbf{C}} = \omega_{re}\mathbf{J} \tag{5.24}$$

$$\hat{\mathbf{D}} = R_s\mathbf{I} + \omega_{re}\mathbf{J}\left[L_s - \frac{M^2}{L_r}\right] \tag{5.25}$$

Then, the complete system dynamics yields

$$\frac{d}{dt}\begin{bmatrix}\vec{x}\\ \vec{\hat{\lambda}}_a^r\end{bmatrix} = \begin{bmatrix}\mathbf{A} & \mathbf{0}_{4\times2}\\ \mathbf{0}_{2\times4} & \hat{\mathbf{A}}\end{bmatrix}\begin{bmatrix}\vec{x}\\ \vec{\hat{\lambda}}_a^r\end{bmatrix} + \begin{bmatrix}\mathbf{B} & \mathbf{0}_{4\times2}\\ \mathbf{0}_{2\times2} & \hat{\mathbf{B}}\end{bmatrix}\begin{bmatrix}\vec{\tilde{v}}_s^r\\ \vec{\tilde{i}}_s^r\end{bmatrix} \tag{5.26}$$

Because the voltage command vector $\vec{\tilde{v}}_s^r$ is synthesized based on the estimated flux linkage vector $\vec{\hat{\lambda}}_a^r$ and the current command vector $\vec{\tilde{i}}_s^r$,

$$\vec{\tilde{v}}_s^r = \hat{\mathbf{C}}\vec{\hat{\lambda}}_a^r + \hat{\mathbf{D}}\vec{\tilde{i}}_s^r \tag{5.27}$$

(5.26) can be further simplified as follows:

$$\frac{d}{dt}\begin{bmatrix}\vec{x}\\ \vec{\hat{\lambda}}_a^r\end{bmatrix} = \begin{bmatrix}\mathbf{A} & \mathbf{B}\hat{\mathbf{C}}\\ \mathbf{0}_{4\times2} & \hat{\mathbf{A}}\end{bmatrix}\begin{bmatrix}\vec{x}\\ \vec{\hat{\lambda}}_a^r\end{bmatrix} + \begin{bmatrix}\mathbf{B}\hat{\mathbf{D}}\\ \hat{\mathbf{B}}\end{bmatrix}\vec{\tilde{i}}_s^r \tag{5.28}$$

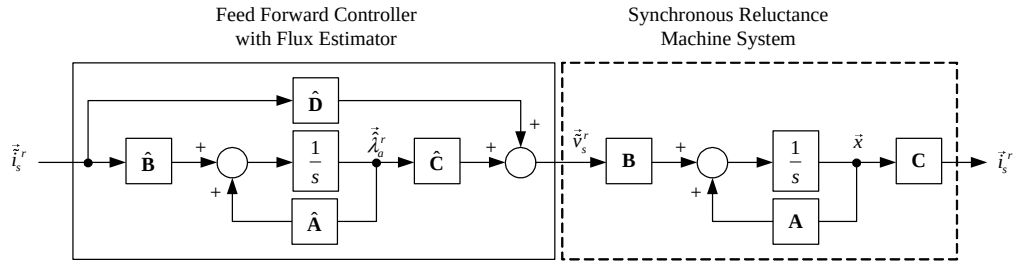

Fig. 5.6. State space diagram of the feedforward control system

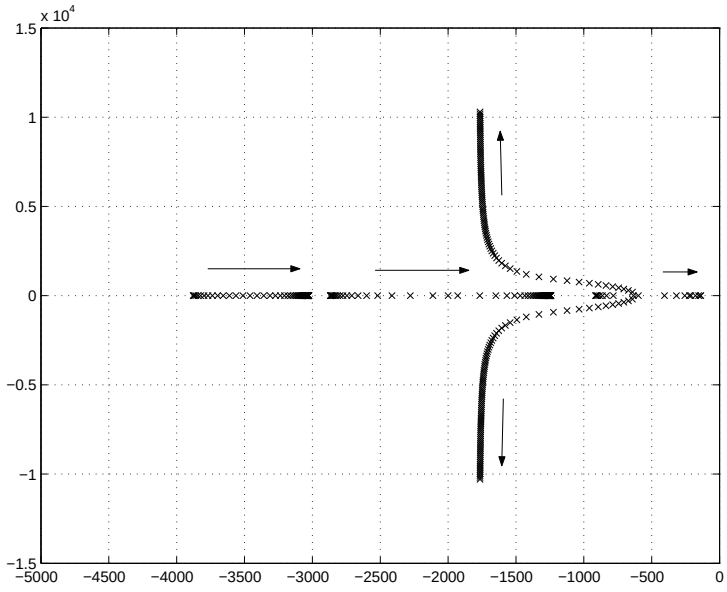

Fig. 5.7. Eigenvalues of the feedforward controlled system (same as machine dynamics) when the speed of the machine is increased from 0 to 50,000 rpm. Arrows denote increasing speed.

The eigenvalues of the (5.28) are shown in Fig. 5.7. The system is stable, but it can be seen that the eigenvalues move toward the origin and higher in the imaginary direction as rotor speed is increased due to the speed term in the model.

5.4.2 Feedback Compensation

Actual measured current values are extracted from the machine state vector $\vec{x}$ by matrix **C**, then current error vector can be given as

$$\Delta\vec{i}_s^r = \vec{\tilde{i}}_s^r - \mathbf{C}\vec{x} \tag{5.29}$$

Taking the PI compensator output and decoupling term into consideration, the system dynamics will be given as

$$\begin{aligned}\frac{d}{dt}\vec{x} &= \mathbf{A}\vec{x} + \mathbf{B}\vec{\tilde{v}}_s^r \\ &= (\mathbf{A} - \mathbf{B}\hat{\mathbf{C}}\mathbf{F}\mathbf{C})\vec{x} + \mathbf{B}\hat{\mathbf{C}}\vec{\tilde{\lambda}}_a^r + \mathbf{B}(\hat{\mathbf{D}} + \hat{\mathbf{C}}\mathbf{F})\vec{\tilde{i}}_s^r\end{aligned} \tag{5.30}$$

where,

$$\vec{\tilde{v}}_s^r = \hat{\mathbf{C}}\vec{\tilde{\lambda}}_a^r + \hat{\mathbf{C}}\mathbf{F}\Delta\vec{i}_s^r + \hat{\mathbf{D}}\vec{\tilde{i}}_s^r, \tag{5.31}$$

$$\mathbf{F} = K_p\mathbf{I} - R_s\omega_{re}^{-1}\mathbf{J} \tag{5.32}$$

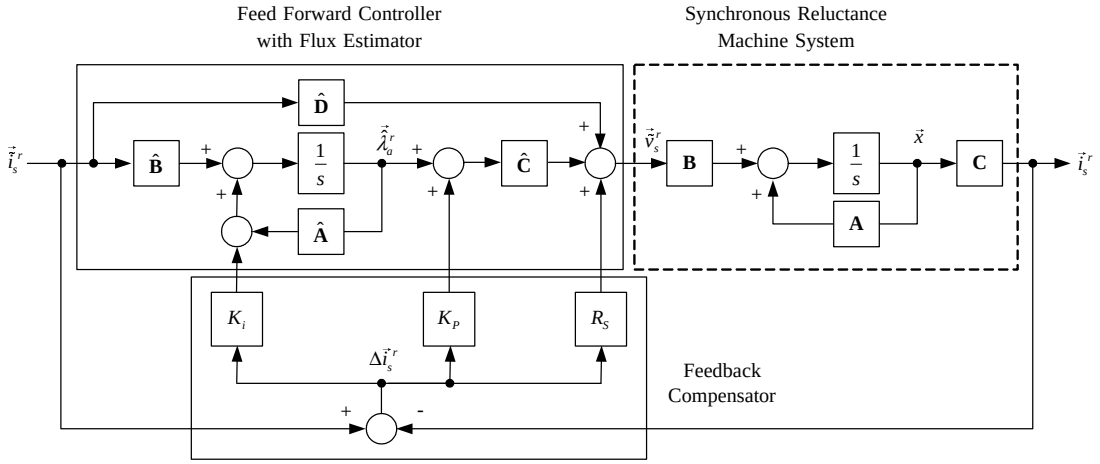

Fig. 5.8. State space diagram of the feedback compensated system

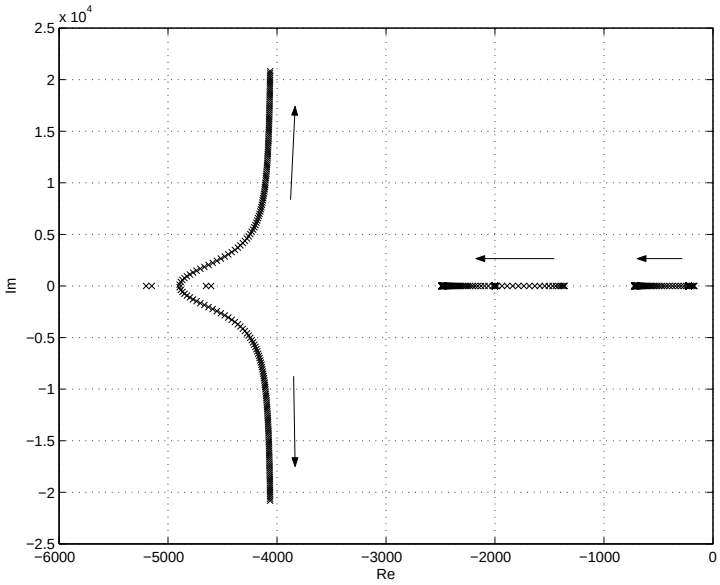

Fig. 5.9. Eigenvalues of the feedforward controlled system with compensator when the speed of the machine is increased from 0 to 50,000 rpm. Case of K_p=$L_{\ell s}$ and K_i=$L_{\ell s}$. Arrows denote increasing speed.

With the integrator part of the controller incorporated with the flux estimator as shown in (5.17), the complete control system with the PI compensator can be represented in matrix form as shown in (5.33).

$$\frac{d}{dt}\begin{bmatrix} \vec{x} \\ \vec{\hat{\lambda}}_a^r \end{bmatrix} = \begin{bmatrix} \mathbf{A} - \mathbf{B}\hat{\mathbf{C}}\mathbf{F}\mathbf{C} & \mathbf{B}\hat{\mathbf{C}} \\ -K_i\mathbf{C} & \hat{\mathbf{A}} \end{bmatrix} \begin{bmatrix} \vec{x} \\ \vec{\hat{\lambda}}_a^r \end{bmatrix} + \begin{bmatrix} \mathbf{B}(\hat{\mathbf{D}} + \hat{\mathbf{C}}\mathbf{F}) \\ \hat{\mathbf{B}} + K_i\mathbf{I} \end{bmatrix} \vec{i}_s^r \tag{5.33}$$

Fig. 5.9 shows the eigenvalues of the compensated system with $K_p = L_{\ell s}$ and $K_i = L_{\ell s}$. It can be seen that the highly-speed-dependent eigenvalues of the system have significantly faster decay rates than the feedforward system.

5.5 Comparison with Voltage Compensation Scheme

The estimated flux linkage, including the PI compensation term, in (5.15) will eventually be utilized to determine the voltage command of the opposite axis through the model in the feedforward controller. By changing the placement of PI regulator and decoupling terms, it is possible to implement a voltage compensated current regulator.

(5.15) can be rewritten as follows:

$$\vec{\hat{v}}_s = R_s\vec{\hat{i}}_s^r + \omega_{re}\mathbf{J}\left\{\left[L_s - \frac{M^2}{L_r}\right]\vec{\hat{i}}_s^r + \vec{\hat{\lambda}}_a^r\right\} + \omega_{re}\mathbf{J}\Delta\vec{\hat{\lambda}}_a^r \tag{5.34}$$

where

$$\Delta\vec{\hat{\lambda}}_a^r = \left(-R_s{\omega_{re}}^{-1}\mathbf{J} + \left[L_s - \frac{M^2}{L_r}\right]\right)\Delta\vec{\hat{i}}_s^r. \tag{5.35}$$

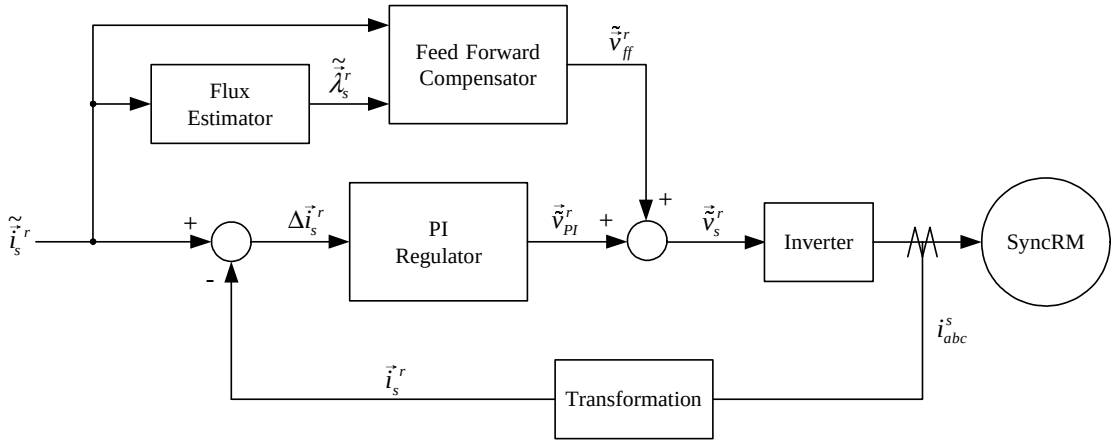

Fig. 5.10. Block diagram of conventional current feedback controller with feedforward compensation

It can be seen that the flux error term $\Delta\vec{\lambda}_a^r$, which can be obtained from the current error, can be utilized to PI compensate the stator voltage command directly, instead of compensating the estimated flux. The output of the PI regulator, which is stator voltage command, will be given as

$$\vec{v}_{PI}^r = \left(K_p + \frac{K_i}{s}\right)\Delta\vec{i}_s^r + \omega_{re}\mathbf{J}\left[L_s - \frac{M^2}{L_r}\right]\Delta\vec{i}_s^r, \tag{5.36}$$

where the term $\omega_{re}\mathbf{J}\left[L_s - \frac{M^2}{L_r}\right]\Delta\vec{i}_s^r$ is included in an attempt to decouple the direct and quadrature dynamics. As well as this PI regulator output, the feedforward compensation voltage calculated from the model is added to the command.

$$\vec{v}_{ff}^r = R_s\vec{i}_s^r + \omega_{re}\mathbf{J}\left\{\left[L_s - \frac{M^2}{L_r}\right]\vec{i}_s^r + \vec{\lambda}_a^r\right\} \tag{5.37}$$

This configuration becomes a conventional feedback current regulator and additive feedforward compensation, which can be seen in Fig. 5.10.

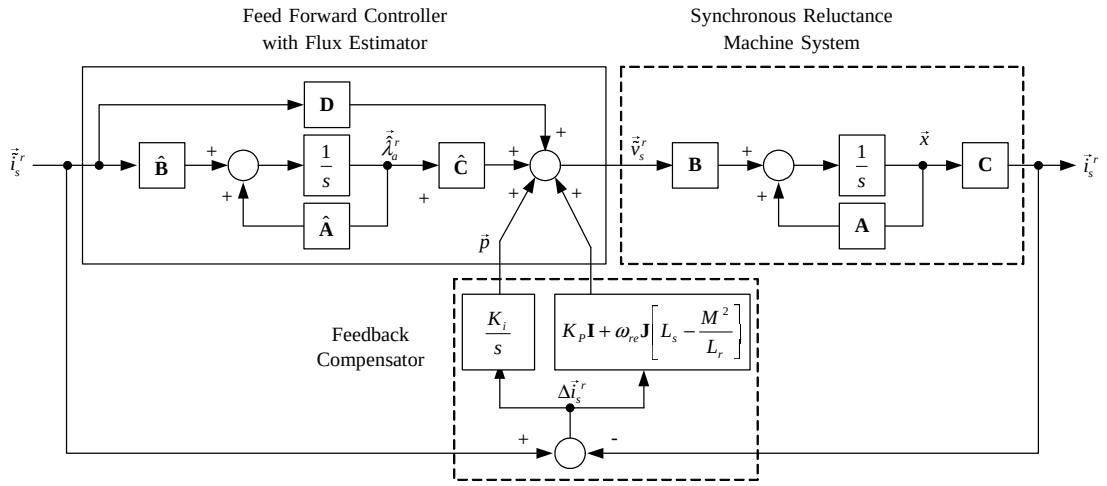

Fig. 5.11. State space diagram of the feedback compensated system: voltage compensation

The state space diagram is shown in Fig. 5.11. Taking the PI regulator output and decoupling term into consideration, the system dynamics will be given as

$$\begin{aligned}\frac{d}{dt}\vec{x} &= \mathbf{A}\vec{x} + \mathbf{B}\vec{\tilde{v}}_s^r \\ &= (\mathbf{A} - \mathbf{BFC})\vec{x} + \mathbf{B}\hat{\mathbf{C}}\vec{\hat{\lambda}}_a^r + \mathbf{B}\vec{p} + \mathbf{B}(\hat{\mathbf{D}} + \mathbf{F})\vec{\tilde{i}}_s^r \end{aligned} \tag{5.38}$$

where,

$$\vec{\tilde{v}}_s^r = \hat{\mathbf{C}}\vec{\hat{\lambda}}_a^r + \vec{p} + \mathbf{F}\Delta\vec{i}_s^r + \hat{\mathbf{D}}\vec{\tilde{i}}_s^r \tag{5.39}$$

$$\mathbf{F} = \omega_{re}\mathbf{J}\left[L_s - \frac{M^2}{L_r}\right] + K_p\mathbf{I} \tag{5.40}$$

The dynamics of the compensator can be derived as follows.

$$\begin{aligned}\frac{d}{dt}\vec{p} &= K_i \Delta \vec{i}_s^{\,r} \\ &= -K_i \mathbf{C}\vec{x} + K_i \vec{\tilde{i}}_s^{\,r}\end{aligned} \tag{5.41}$$

Therefore the complete control system with the PI compensator can be represented in matrix form as (5.42).

$$\frac{d}{dt}\begin{bmatrix} \vec{x} \\ \vec{\hat{\lambda}}_a^{\,r} \\ \vec{p} \end{bmatrix} = \begin{bmatrix} \mathbf{A}-\mathbf{BFC} & \mathbf{B}\hat{\mathbf{C}} & \mathbf{B} \\ \mathbf{0}_{2\times 4} & \hat{\mathbf{A}} & \mathbf{0}_{2\times 2} \\ -K_i\mathbf{C} & \mathbf{0}_{2\times 2} & \mathbf{0}_{2\times 2} \end{bmatrix} \begin{bmatrix} \vec{x} \\ \vec{\hat{\lambda}}_a^{\,r} \\ \vec{p} \end{bmatrix} + \begin{bmatrix} \mathbf{B}(\hat{\mathbf{D}}+\mathbf{F}) \\ \hat{\mathbf{B}} \\ K_i\mathbf{I} \end{bmatrix} \vec{\tilde{i}}_s^{\,r} \tag{5.42}$$

Note that the flux compensation scheme has one less integrator. Figs. 5.12 and 5.13 shows the eigenvalues of the flux compensated and voltage compensated system at 50,000 rpm with varying gains. K_p and K_i have been varied from 0 to $L_{\ell s}$ and to R_s for flux and voltage compensator, respectively. Although the difference between these two configurations has not been significant in terms of performance, it can be seen in Figs. 5.14 - 5.17 that the oscillating mode in flux compensation scheme has lower oscillation frequency and faster decay.

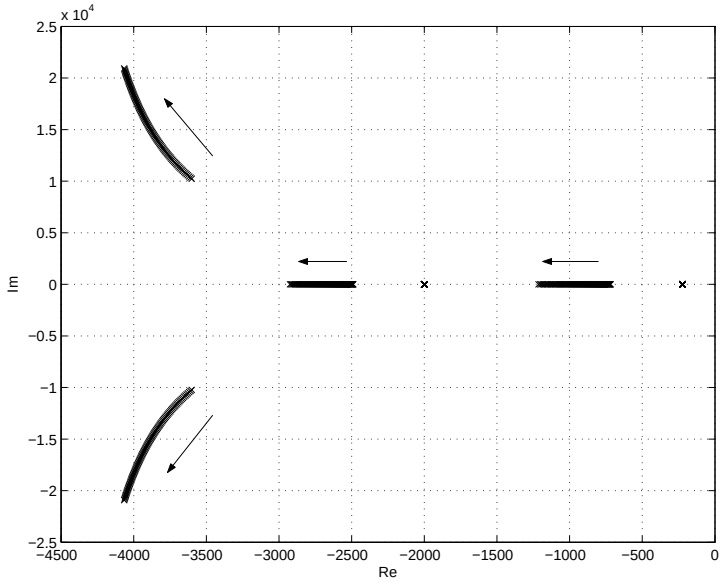

Fig. 5.12. Eigenvalues of the feedforward controlled system with flux compensator when the PI gains are increased from 0 to $L_{\ell s}$ at 50,000 rpm. Arrows denote increasing gain.

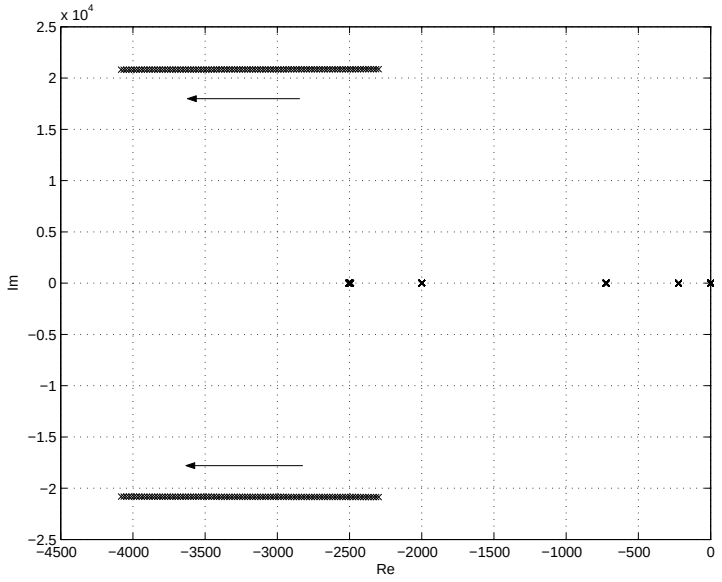

Fig. 5.13. Eigenvalues of the feedforward controlled system with voltage compensator when the PI gains are increased from 0 to R_s at 50,000 rpm. Arrows denote increasing gain.

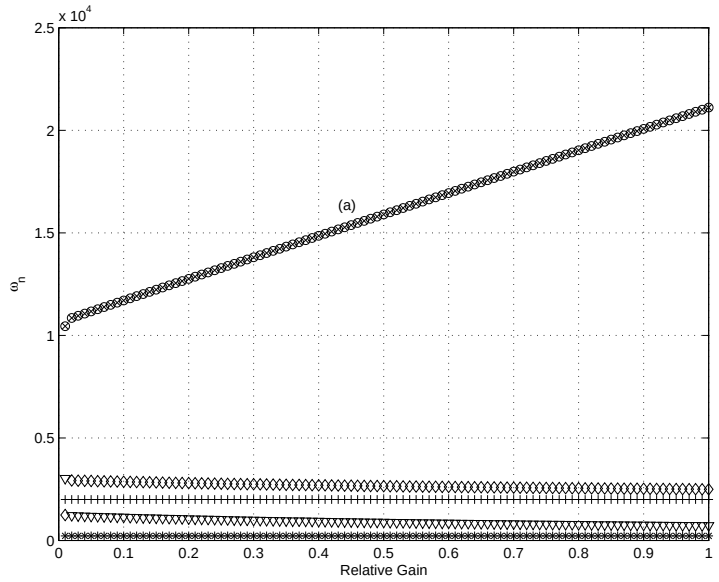

Fig. 5.14. Natural frequency of the flux compensated system poles when the PI gains are increased from 0 to $L_{\ell s}$ at 50,000 rpm. Relative gains represent the scale factor to $L_{\ell s}$.

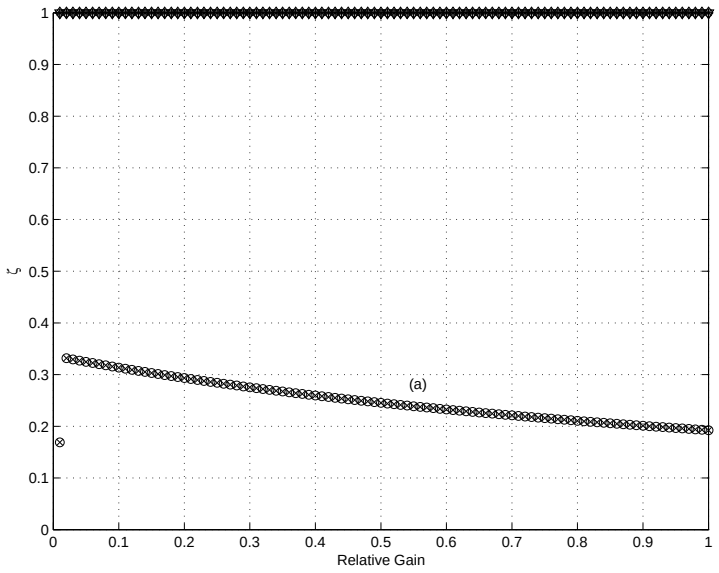

Fig. 5.15. Damping ratio of the flux compensated system poles when the PI gains are increased from 0 to $L_{\ell s}$ at 50,000 rpm. Relative gains represent the scale factor to $L_{\ell s}$.

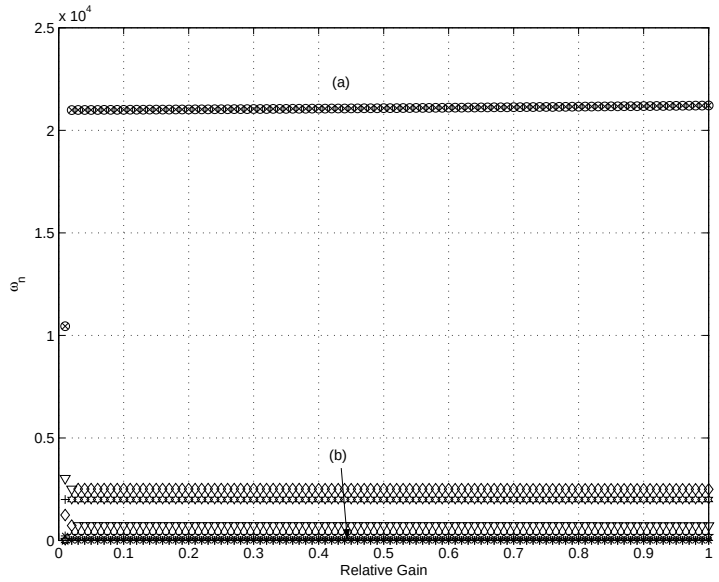

Fig. 5.16. Natural frequency of the voltage compensated system poles when the PI gains are increased from 0 to R_s at 50,000 rpm. Relative gains represent the scale factor to R_s.

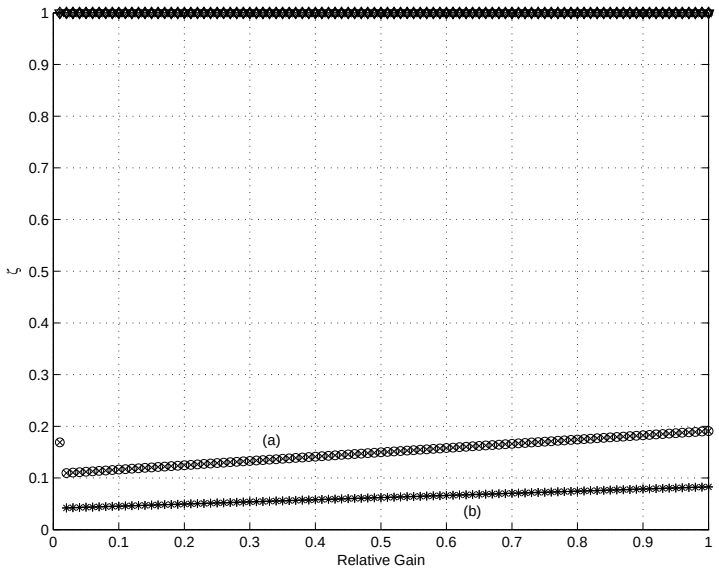

Fig. 5.17. Damping ratio of the voltage compensated system poles when the PI gains are increased from 0 to R_s at 50,000 rpm. Relative gains represent the scale factor to R_s.

5.6 Experimental Validation

To validate the theory, experiments using the proposed current regulator have been performed on a 120 kW, 4-pole solid-rotor synchronous reluctance machine that had been utilized in chapter 3. This machine, and the proposed controller, has been tested as part of a flywheel energy storage system manufactured by Pentadyne Power Corporation that is capable of providing 120 kW of DC electrical power for up to 20 seconds over a speed range of 25,000 to 54,000 rpm. The machine is driven by a 18 kHz-switching three-phase inverter, and the control algorithm is implemented in a DSP processor. The block diagram of the experimental system is shown in Fig. 3.20.

The proposed model-based feedforward controller assumes linear magnetic behavior, meaning that the flux linkages of the machine are linearly related to the currents. In practice, however, this relationship is nonlinear. While saturation of the machine iron is one possible nonlinear effect, in the system under study this effect is not significant in the operating range of the machine, due to its relatively large air gap. Another nonlinear magnetic property which has more of an effect on the system under study is the remanent magnetization of the iron in the rotor of the machine, which can be seen in Fig. 5.18. This creates errors in the current tracking that are particularly important at relatively low power levels. Although the model could possibly be modified to incorporate these nonlinearities, they can also be utilized to validate the performance of the feedback compensator.

Step current commands of 150 A are applied for direct- and quadrature-axis currents in rotor reference frame to feedforward and feedback-compensated controller, respectively. As can be seen in Fig. 5.19, there are offsets in the current tracking in the direct- and quadrature-axis

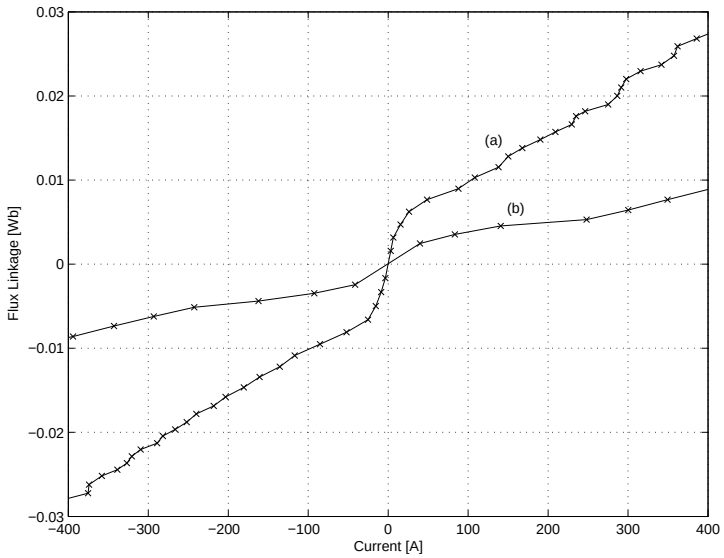

Fig. 5.18. Experimentally measured flux linkages in rotor reference frame. (a) λ_{sd}^{r} (b) λ_{sq}^{r}

when only the feedforward controller is used. Also, for a ramp current command to 300 A, current tracking errors are generated in the low current region, as shown in Fig. 5.20. When PI compensated, it is shown in Figs. 5.21 and 5.22 that the current errors are effectively removed.

In UPS applications, the motor/generator generates the necessary power for the DC bus controller to maintain the bus voltage and support the load even with a feedforward controller with parameter deficiencies, because the voltage controller modifies the current commands to get the required torque to support the load. However, the operating point of the machine will be off from the commanded operating point due to the parameter error, even if the DC bus is properly regulated. Hence, the motor/generator will not be operating in the optimal or designed operating point. Furthermore, if the erroneous operating point requires a higher than necessary current to achieve the desired torque, the inverter would trip. This can cause problems for some critical operating conditions unless the current error is not compensated.

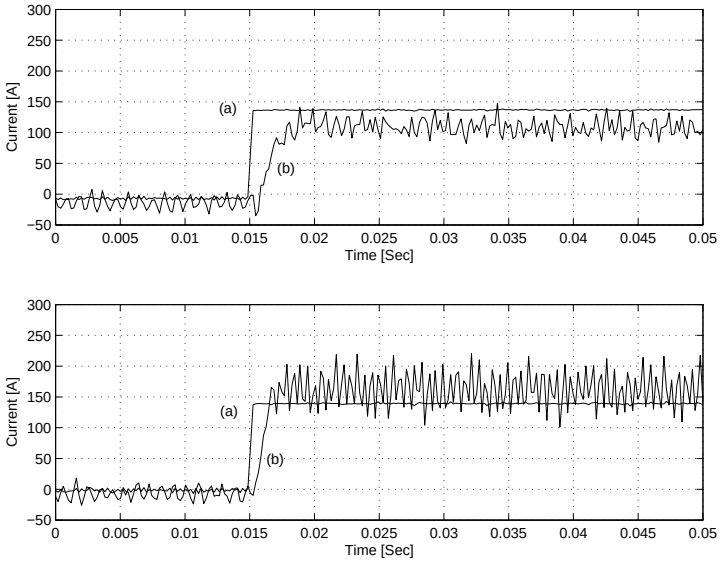

Fig. 5.19. Experiment: 150 A step commands in rotor reference frame at 35,000 rpm. Model-based controller. Upper: direct-axis, lower: quadrature-axis. (a) Command current $\tilde{i}_s^r$ (b) Actual current i_s^r

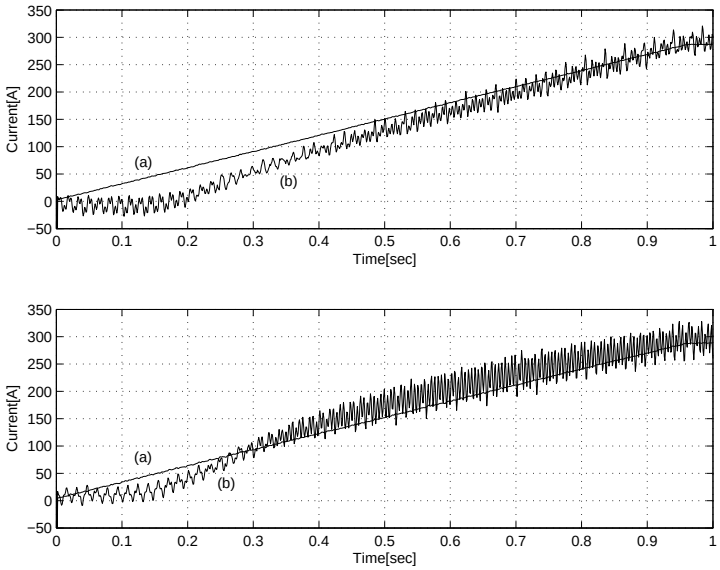

Fig. 5.20. Experiment: $0 \sim 300$ A ramp commands in rotor reference frame at 35,000 rpm. Model-based controller. Upper: direct-axis, lower: quadrature-axis. (a) Command current $\tilde{i}_s^r$ (b) Actual current i_s^r

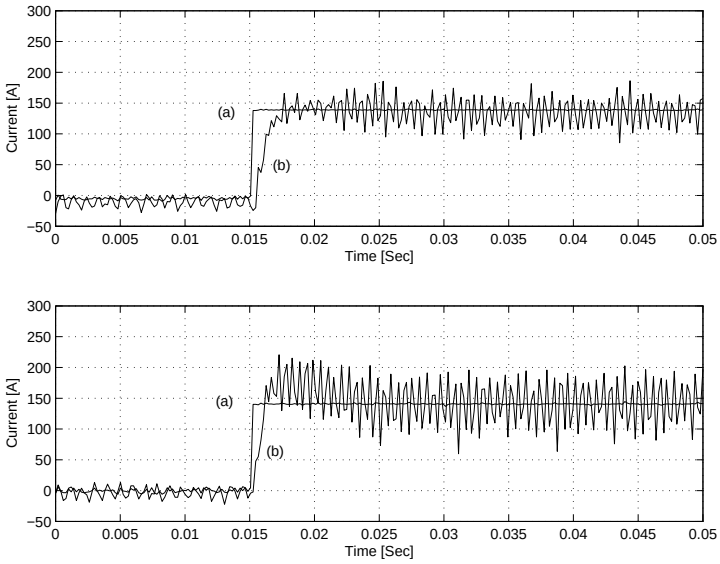

Fig. 5.21. Experiment: 150 A step commands in rotor reference frame at 35,000 rpm. Model-based controller with PI compensator. Upper: direct-axis, lower: quadrature-axis. (a) Command current $\tilde{i}_s^r$ (b) Actual current i_s^r

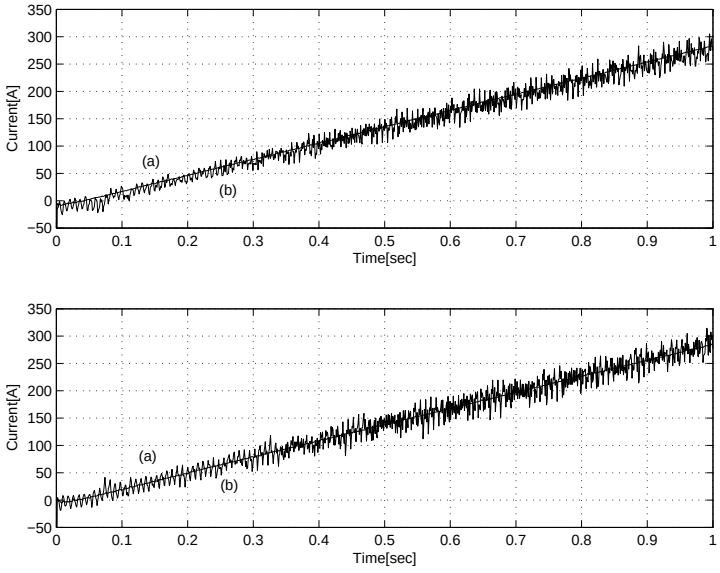

Fig. 5.22. Experiment: $0 \sim 300$ A current commands in rotor reference frame at 35,000 rpm. Model-based controller with PI compensator. Upper: direct-axis, lower: quadrature-axis. (a) Command current $\tilde{i}_s^r$ (b) Actual current i_s^r

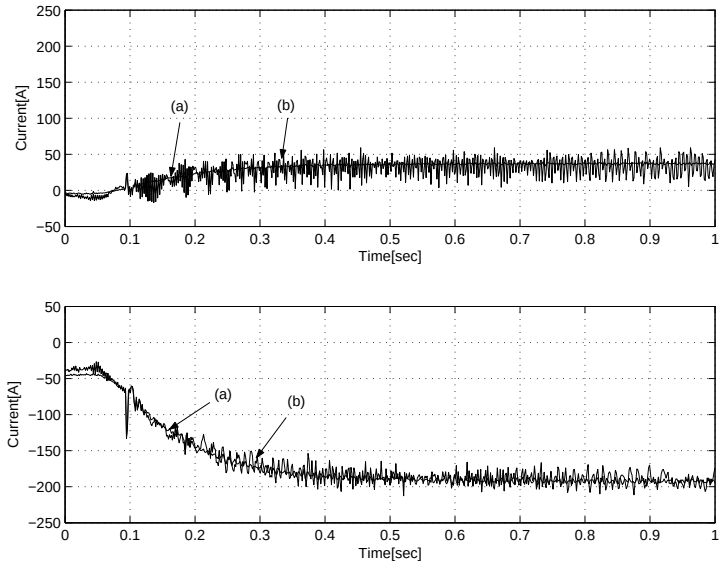

Fig. 5.23. Experiment: 32 kW discharge on minimum flux linkage operating point at 35,000 rpm. Conventional current regulator and additive feedforward compensation configuration. Current commands are supplied by bus voltage regulator. (a) Command current $\tilde{i}_s^r$ (b) Actual current i_s^r

5.7 Conclusion

In this chapter, a hybrid controller consisting of a model-based feedforward controller and a PI feedback compensator for a solid-rotor synchronous reluctance motor/generator has been proposed. The proposed control scheme has been applied to a motor/generator in a high-speed, flywheel-based UPS system. It has been shown that the proposed hybrid controller with PI feedback compensator in addition to the model-based controller considering flux dynamics in the solid-rotor scheme easily compensates errors in the flux linkage estimator caused by inaccurate parameters, as well as improves the regulation performance for the current commands and the stability of the system.

Chapter 6

Analysis and Reduction of Time Harmonic Loss using LC Filter

6.1 Introduction

It has been shown that a solid rotor of synchronous reluctance machine has good structural integrity for high speed operation, but a non-laminated rotor has eddy current issue. As well as the flux dynamics in the rotor, another concern with these eddy currents is the resulting heat generation in the rotor [27]. A flywheel which is supported by magnetic bearings and spinning in vacuum has only blackbody radiation to remove the heat from the rotor, a relatively poor heat transfer mechanism. As a result, heat generated by the rotor eddy currents must be minimized. These eddy currents can be generated by switching harmonics in the stator voltage/current waveforms, winding harmonics due to the non-sinusoidal winding construction, and slot harmonics due to the use of a slotted stator.

A three-phase LC filter, as shown in Fig. 6.1, can be used to reduce switching harmonics, and hence rotor conduction losses, in the synchronous reluctance machine. However, due to the relatively low ratio between the fundamental and switching frequencies in high-speed applications, the design of such an LC filter, and the control of the resulting system, can be challenging despite its simplicity. Although usage of an LC filter at the output of the PWM inverter has been studied in many previous works [59–62], mostly they were for the reduction of EMI caused by stator leakage current and the relationship with rotor loss reduction has not been studied. A

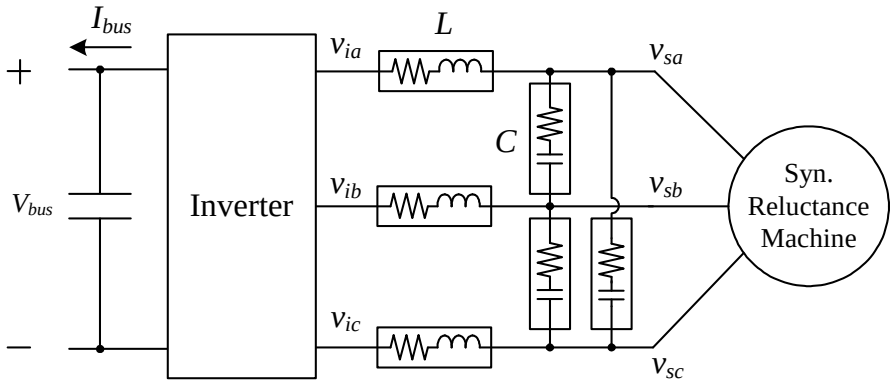

Fig. 6.1. High-speed synchronous reluctance drive with three-phase LC filter

multi-level inverter can be a solution for the time-harmonics in the PWM voltage [63, 64], but the cost is significantly higher due to its complexity.

This chapter performs an analysis for the time-harmonic loss in a solid-rotor synchronous reluctance machine, and investigates design and control issues associated with the inclusion of three-phase LC filter for reduction of the rotor loss in solid rotor. The pertinent issues that affect the selection of the LC filter parameters are also discussed. A technique to estimate the rotor losses in the synchronous reluctance machine is presented. A modified model-based control algorithm which takes the effects of the LC filter into account is utilized. Experiments have been performed on a 120 kW, 54,000 rpm synchronous reluctance drive, and the results are presented.

6.2 Model of Filter-Machine System in Rotor Reference Frame

6.2.1 Synchronous Reluctance Machine Model

Although the rotor of a synchronous reluctance machine in steady-state operation would ideally have zero losses because the spatial flux wave rotates in synchronism with the rotor, in

reality the rotor can be subjected to high-frequency flux oscillations due to various harmonics, such as PWM switching, stator teeth, and winding harmonics. Rotor losses due to winding and tooth harmonics are dictated by the design of the synchronous reluctance machine, as discussed in [27]. These types of losses can be characterized only with the use of sophisticated machine models, such as those generated by finite element analysis. Rotor losses due to time harmonics in the voltage and current waveforms can, however, to a certain extent be characterized with the smooth-airgap models used in the vector control of AC electric machines. In this chapter, we will focus on modeling these time harmonics.

The stator and rotor fluxes in the machine can be represented as

$$\vec{\lambda}_s^r = [L_s]\vec{i}_s^r + [M]\vec{i}_r^r \tag{6.1}$$

$$\vec{\lambda}_r^r = [L_r]\vec{i}_r^r + [M]\vec{i}_s^r. \tag{6.2}$$

where

$$\vec{x} = \begin{bmatrix} x_d \\ \\ x_q \end{bmatrix}, \quad [Y] = \begin{bmatrix} Y_d & 0 \\ \\ 0 & Y_q \end{bmatrix}, \tag{6.3}$$

the superscript 'r' represents the rotor reference frame, and the 'd' and 'q' subscripts represent direct and quadrature values, respectively. We note again that zero rotor current is typically assumed in synchronous reluctance machines, as ideally there is no current in the rotor, which rotates synchronously with the fundamental component of the stator winding excitation. However, in reality rotor currents are generated by the various time harmonics the rotor experiences. Placing an LC filter at the inverter output is one method to mitigate rotor losses due to inverter

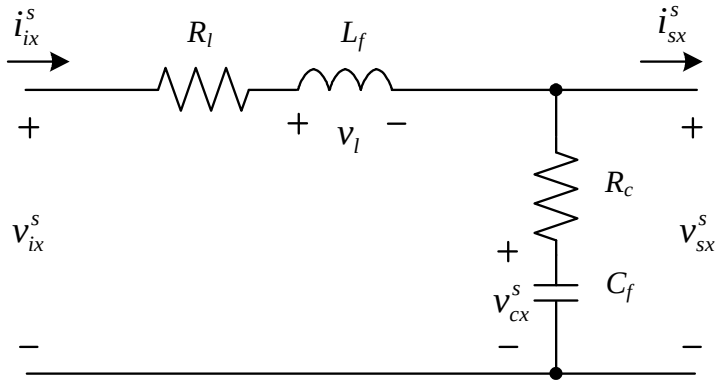

Fig. 6.2. Single phase diagram of three-phase LC filter in stator reference frame

switching harmonics. The effect of the LC filter on the synchronous reluctance machine will be investigated in the following section.

6.2.2 Three-phase LC Filter in Rotor Reference Frame

A single-phase diagram of a three-phase LC filter is shown in Fig. 6.2. By applying the Kirchhoff's current and voltage laws, the circuit equations for the diagram can be written as follows. The subscript '*x*' denotes phase (i.e., '*a*', '*b*', or '*c*'), and the superscript '*s*' denotes the stator reference frame.

$$\frac{d}{dt}i^s_{ix} = \frac{1}{L_f}\left(v^s_{ix} - v^s_{sx} - R_\ell i^s_{ix}\right) \tag{6.4}$$

$$\frac{d}{dt}v^s_{cx} = \frac{1}{C_f}i^s_{cx} \tag{6.5}$$

$$i^s_{cx} = i^s_{ix} - i^s_{sx} \tag{6.6}$$

$$v^s_{sx} = v^s_{cx} + R_c i^s_{cx} \tag{6.7}$$

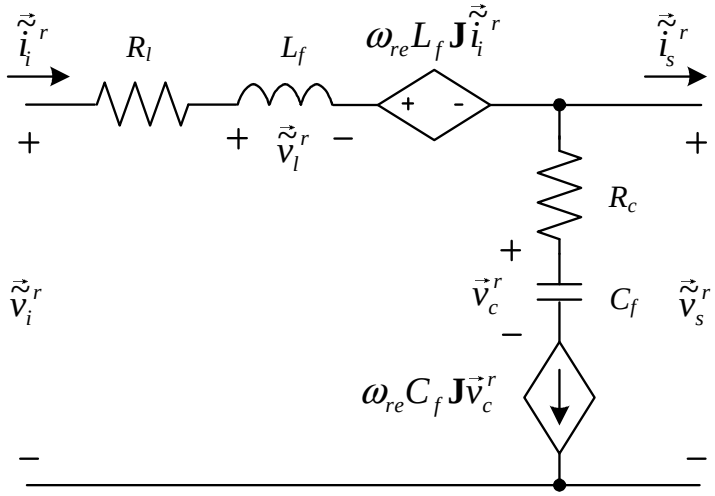

Fig. 6.3. Three-phase LC filter represented in two-phase rotor reference frame

The presence of the LC filter therefore adds additional dynamics associated with the inductor current and capacitor voltage. The synchronous reluctance machine, however, is most easily modeled in the rotor reference frame due to the saliency of the rotor structure. The above dynamics, which are represented in the stator reference frame, should therefore be transformed to the rotor reference frame in order to be analyzed with the synchronous reluctance machine dynamics. By applying 3-2 phase conversions and rotor reference frame transformations, the following rotor reference frame representation of the three-phase LC filter dynamics can be obtained.

$$\frac{d}{dt}\vec{i}_i^{\,r} = \frac{1}{L_f}\left(\vec{v}_i^{\,r} - \vec{v}_s^{\,r} - R_\ell \vec{i}_i^{\,r}\right) - \omega_{re}\mathbf{J}\vec{i}_i^{\,r} \tag{6.8}$$

$$\frac{d}{dt}\vec{v}_c^{\,r} = \frac{1}{C_f}\vec{i}_c^{\,r} - \omega_{re}\mathbf{J}\vec{v}_c^{\,r} \tag{6.9}$$

$$\vec{i}_c^{\,r} = \vec{i}_i^{\,r} - \vec{i}_s^{\,r} \tag{6.10}$$

$$\vec{v}_s^{\,r} = \vec{v}_c^{\,r} + R_c\vec{i}_c^{\,r} \tag{6.11}$$

Table 6.1. Machine, filter, and inverter parameters

Number of Poles P	4
Stator Resistance R_s	17 mΩ
Direct Stator Inductance L_{sd}	54.4 μH
Quadrature Stator Inductance L_{sq}	15.6 μH
Direct Mutual Inductance M_d	44.8 μH
Quadrature Mutual Inductance M_q	6.0 μH
Direct Rotor Inductance L_{rd}	45.6 μH
Quadrature Rotor Inductance L_{rq}	7.7 μH
Direct Rotor Resistance R_{rd}	11.4 mΩ
Quadrature Rotor Resistance R_{rq}	15.4 mΩ
Filler Capacitor C_f	75 μF
Filter Inductance L_f	5.5 μH
Capacitor ESR R_c	2 $\mu\Omega$
Inductor Resistance R_l	5 $\mu\Omega$
Inverter DC Bus Voltage V_{bus}	540 V

The resulting model of the LC filter can now be incorporated with the synchronous reluctance machine model in the previous section and combined filter-machine dynamics can be written in matrix form, as shown in (6.12). The machine and filter parameters and variables used in the analysis presented in this chapter are provided in Table 6.1.

$$\begin{bmatrix} -\mathbf{I} & (\mathbf{J}\omega_{re} + \frac{d}{dt}\mathbf{I})\,[M] & R_s\mathbf{I} + (\mathbf{J}\omega_{re} + \frac{d}{dt}\mathbf{I})[L_s] & 0 \\ 0 & [R_r] + \frac{d}{dt}[L_r] & \frac{d}{dt}[M] & 0 \\ \mathbf{I} & 0 & 0 & R_\ell\mathbf{I} + (\mathbf{J}\omega_{re} + \frac{d}{dt}\mathbf{I})L_f \\ (\mathbf{J}\omega_{re} + \frac{d}{dt}\mathbf{I})C_f & 0 & \mathbf{I} + R_cC_f(\mathbf{J}\omega_{re} + \frac{d}{dt}\mathbf{I}) & -\mathbf{I} - R_cC_f(\mathbf{J}\omega_{re} + \frac{d}{dt}\mathbf{I}) \end{bmatrix} \begin{bmatrix} \vec{v}_s^{\,r} \\ \vec{i}_r^{\,r} \\ \vec{i}_s^{\,r} \\ \vec{i}_i^{\,r} \end{bmatrix} = \begin{bmatrix} 0 \\ 0 \\ \vec{v}_i^{\,r} \\ 0 \end{bmatrix} \tag{6.12}$$

6.3 LC Filter Design

6.3.1 Resonance Frequency

The performance of the LC filter is largely determined by the resulting resonance frequency it introduces into the system. Since these filters typically have little damping due to loss mechanisms, the resonance frequency should be placed so that it is not excited. The resonance frequency of the filter has to be sufficiently below the lowest PWM switching harmonic frequency to ensure good filtering. Furthermore, the resonant frequency should also be sufficiently higher than the fundamental frequency to avoid adverse effects. Also, the presence of the LC filter can slow the transient response of the system to a certain degree. These considerations require that the resonance frequency of the filter not be too low.

6.3.2 Filter Parameters

Once the resonance frequency of the LC filter is determined, theoretically there are a infinite number of combinations of inductance and capacitance for the LC filter. Although each physically possible combination has the same frequency characteristics, they may have different effect on the overall system performance. Increased filter inductance will achieve more sinusoidal inverter current waveforms, but it also results in a larger voltage drop across the filter inductor, thereby reducing the voltage that can applied to the machine and hence reducing the power rating of the drive.

Higher capacitance for a given resonance frequency achieves smaller inductor voltage drop, and will also improve the power factor of the inverter load due to the compensation of reactive power by the filter capacitor. However, a large capacitance could be problematic due to

Fig. 6.4. Filter inductor and capacitor utilized in the three-phase LC filter for 120 kW, 54,000 rpm synchronous reluctance motor/generator system under study.

the larger inverter currents required to charge and discharge the capacitors. Furthermore, the iron in the rotor of the synchronous reluctance machine can have a (small) remanent magnetization, and hence the machine behaves slightly like a permanent magnet machine. In certain flywheel applications, such as uninterruptible power supplies, the system spends most of its time spinning at top speed with the inverter disabled. The presence of the capacitors in the LC filter in such a situation present a path for circulating currents to flow due to the voltage produced by this remanent magnetization, thereby creating a ”spinning loss” in the system. Furthermore, care must be taken that a resonant frequency generated by the capacitor and the machine inductances is not excited by the excitation, which requires placing this resonant frequency well above the fundamental operating range.

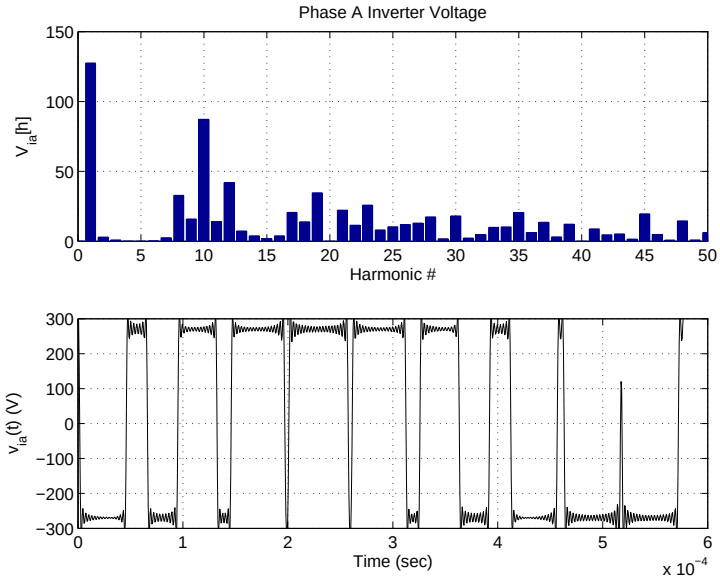

Fig. 6.5. Top: Simulated magnitude of complex Fourier series coefficients of representative phase '*A*' inverter voltage. Bottom: Time waveform of phase '*A*' inverter voltage reconstructed from above harmonics.

6.4 Estimation of Rotor Losses

6.4.1 Rotor Losses in Synchronous Reluctance Machines

Inverter output voltages are generated by pulse-width-modulation techniques and hence they contain harmonic voltage components, as shown in Fig. 6.5. The harmonics presented here are in the stator reference frame. In order to incorporate these time harmonics into the model, a method of transforming these harmonics into the rotor reference frame is necessary. Such an approach is outlined below.

6.4.2 Transformation of Stationary Time Harmonics into Rotor Reference Frame

In order to determine how time harmonics in the stator reference frame are transferred into the rotor reference frame, we consider the case of a time-varying, periodic, two-phase vector $\vec{x}^s$ in the stator reference frame.

$$\vec{x}^s(t) = \sum_{n=-\infty}^{\infty} e^{jn\omega_0 t} \vec{\vec{X}}^s[n], \tag{6.13}$$

where the superscript '*s*' corresponds to the stator reference frame, $\vec{\vec{X}}^s[n]$ are the (complex) Fourier coefficients of $\vec{x}^s$, and ω_0 is a fundamental frequency, of which all frequencies of interest are integral multiples. The resulting fundamental period is therefore given by:

$$T_0 = \frac{2\pi}{\omega_0} \tag{6.14}$$

We note that the harmonics of two-phase variables can be determined simply by performing the 3-2 phase conversion on the harmonics of three-phase variables. This two-phase vector is transformed into the rotor reference frame as follows:

$$\vec{x}^r(t) = e^{-\mathbf{J}\theta_{re}} \vec{x}^s(t), \tag{6.15}$$

where θ_{re} is the (electrical) rotor position. Assuming that the rotor is spinning at a constant electrical speed ω_{re}, the reference frame transformation can be represented as,

$$\vec{x}^r(t) = e^{-\mathbf{J}(\omega_{re}t + \theta_{r0})} \vec{x}^s(t) \tag{6.16}$$

The vector in the rotor reference frame is therefore given by:

$$\begin{aligned}\vec{x}^{r}(t) &= \sum_{n=-\infty}^{\infty} e^{-\mathbf{J}(\omega_{re}t+\theta_{r0})} e^{jn\omega_0 t} \vec{\bar{X}}^{s}[n] \\ &= \sum_{n=-\infty}^{\infty} e^{[jn\omega_0 t\mathbf{I}-(\omega_{re}t+\theta_{r0})\mathbf{J}]} \vec{\bar{X}}^{s}[n]\end{aligned} \tag{6.17}$$

Assuming that the rotor electrical speed is an integral multiple of ω_0 (i.e., $\omega_{re} = m\omega_0$), the harmonics in the rotor reference frame are given by:

$$\begin{aligned}\vec{\bar{X}}^{r}[n'] &= \frac{1}{T_0}\int_0^{T_0} e^{-jn'\omega_0 t}\vec{x}^{r}(t)dt \\ &= \frac{1}{T_0}\sum_{n=-\infty}^{\infty}\left\{\int_0^{T_0} e^{\left[j(n-n')\mathbf{I}-m\mathbf{J}\right]\omega_0 t}dt\right\} e^{-\mathbf{J}\theta_{r0}}\vec{\bar{X}}^{s}[n]\end{aligned} \tag{6.18}$$

If we assume the exponent of the natural matrix exponential in the integral is nonsingular, the integral is evaluated as:

$$\int_0^{T_0} e^{\left[j(n-n')\mathbf{I}-m\mathbf{J}\right]\omega_0 t}dt = 0 \tag{6.19}$$

Hence the only nonzero harmonics of the voltage in the rotor reference frame occur when the matrix component of the exponent is singular. The determinant of this matrix is given by:

$$det\left(j(n-n')\mathbf{I}-m\mathbf{J}\right) = -(n-n')^2 + m^2 \tag{6.20}$$

The determinant is therefore zero, and hence the matrix is singular, in the cases $n' = n - m$ and $n' = n + m$. We now examine these two specific cases.

1) Case 1: $n' = n - m$

$$\int_0^{T_0} e^{\left[j(n-n')\mathbf{I}-m\mathbf{J}\right]\omega_0 t} dt = \frac{T_0}{2}\left(\mathbf{I} - j\mathbf{J}\right) \tag{6.21}$$

2) Case 2: $n' = n + m$

$$\int_0^{T_0} e^{\left[j(n-n')\mathbf{I}-m\mathbf{J}\right]\omega_0 t} dt = \frac{T_0}{2}\left(\mathbf{I} + j\mathbf{J}\right) \tag{6.22}$$

Hence, a given harmonic n of the voltage in the stationary frame relates to harmonics in the rotor reference frame as follows:

$$\begin{aligned}\vec{\vec{X}}^r[n-m] &= \frac{1}{2}\left(\mathbf{I} - j\mathbf{J}\right) e^{-\mathbf{J}\theta_{r0}} \vec{\vec{X}}^s[n], \\ \vec{\vec{X}}^r[n+m] &= \frac{1}{2}\left(\mathbf{I} + j\mathbf{J}\right) e^{-\mathbf{J}\theta_{r0}} \vec{\vec{X}}^s[n]\end{aligned} \tag{6.23}$$

Therefore, a frequency ω^s in the stator reference frame will generate excitation in the rotor reference frame at frequencies $\omega^s - \omega_{re}$ and $\omega^s + \omega_{re}$:

$$\begin{aligned}\vec{\vec{X}}^r\left(\omega^s - \omega_{re}\right) &= \frac{1}{2}\left(\mathbf{I} - j\mathbf{J}\right) e^{-\mathbf{J}\theta_{r0}} \vec{\vec{X}}^s\left(\omega^s\right), \\ \vec{\vec{X}}^r\left(\omega^s + \omega_{re}\right) &= \frac{1}{2}\left(\mathbf{I} + j\mathbf{J}\right) e^{-\mathbf{J}\theta_{r0}} \vec{\vec{X}}^s\left(\omega^s\right)\end{aligned} \tag{6.24}$$

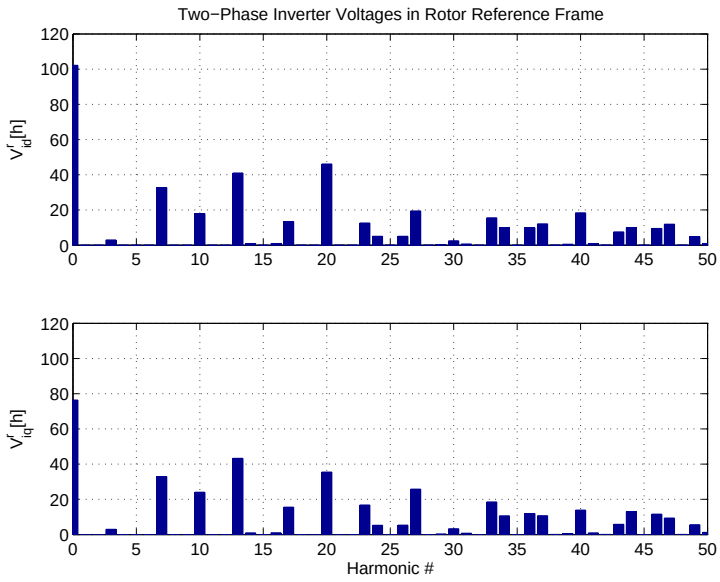

Fig. 6.6. Simulated two-phase inverter voltages in rotor reference frame.

It should be noted that more than one frequency in the stator reference frame can be associated with a specific frequency in the rotor reference frame, and hence the contributions of the two stationary frequencies must be combined. Fig. 6.6 presents the resulting two-phase, rotor reference frame harmonics of the inverter voltage spectrum of Fig. 6.5. The lower harmonic content of these two-phase voltages, as compared to the single-phase content of Fig. 6.5, can be ascribed to the removal of common-mode components in the 3-2 phase conversion process. It can be seen that, due to the close proximity of the fundamental frequency and the switching frequency, non-negligible harmonics exist at fairly low harmonic frequencies. The capacitor current in the LC filter is shown in Fig. 6.8.

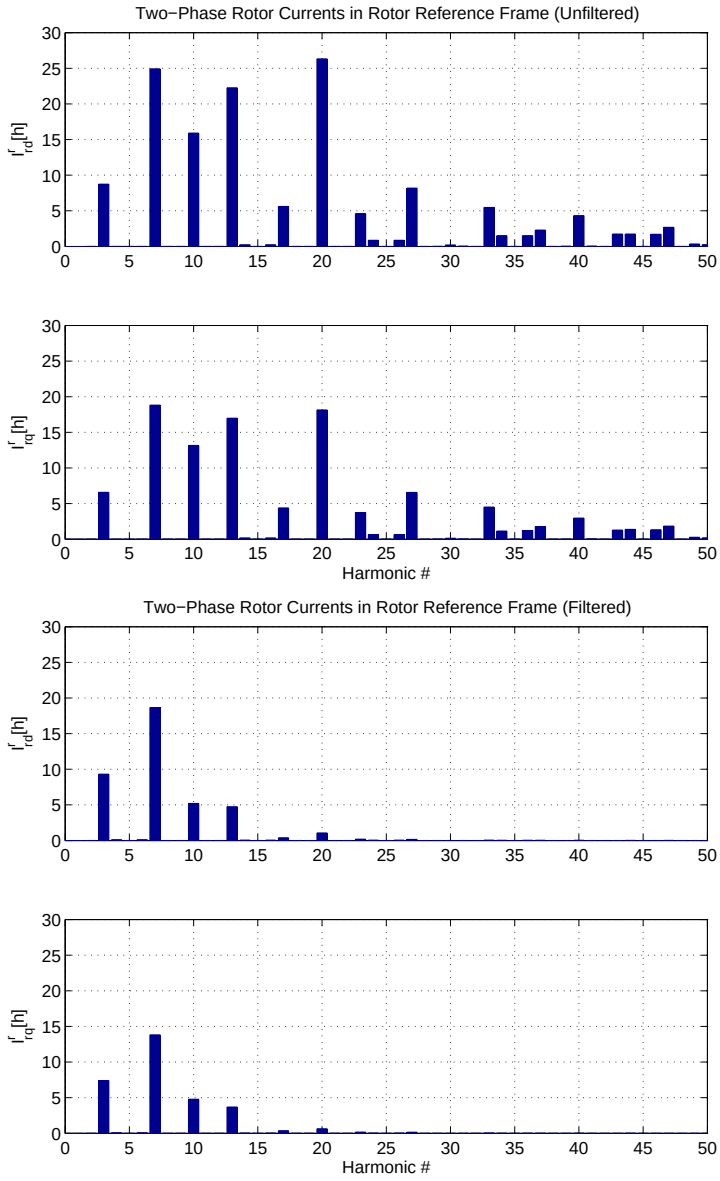

Fig. 6.7. Simulated two-phase rotor currents in rotor reference frame, 130 kW generating, 54,000 rpm, minimum flux linkage operating point. Top: without LC filter, bottom: with LC filter.

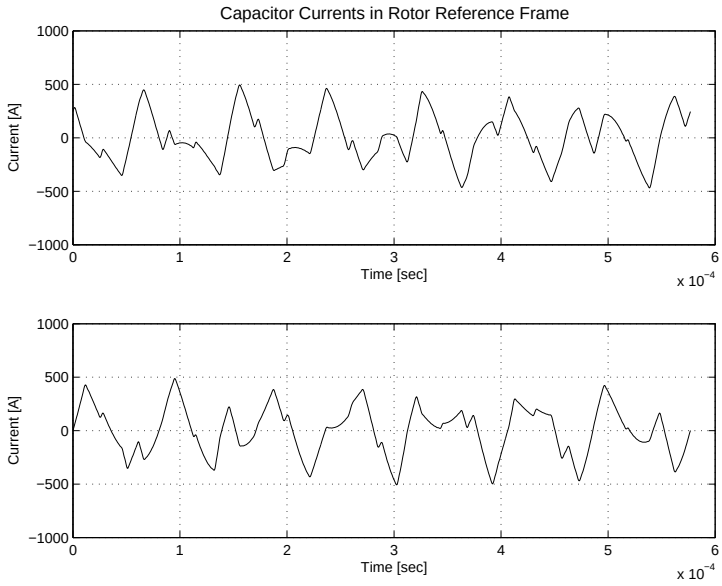

Fig. 6.8. Simulated two-phase capacitor currents of LC filter in rotor reference frame, 130 kW generating, 54,000 rpm, minimum flux linkage operating point.

Once the stationary harmonic components are transformed into the rotor reference frame, a phasor analysis is conducted by substituting $\frac{d}{dt}\vec{x}$ with $j\omega^r\vec{x}$, where ω^r corresponds to a particular harmonic frequency as seen in the rotor reference frame.

$$\begin{bmatrix} -\mathbf{I} & (\mathbf{J}\omega_{re}+j\omega^r\mathbf{I})[M] & R_s\mathbf{I}+(\mathbf{J}\omega_{re}+j\omega^r\mathbf{I})[L_s] & 0 \\ 0 & [R_r]+j\omega^r[L_r] & j\omega^r[M] & 0 \\ \mathbf{I} & 0 & 0 & R_\ell\mathbf{I}+(\mathbf{J}\omega_{re}+j\omega^r\mathbf{I})L_f \\ (\mathbf{J}\omega_{re}+j\omega^r\mathbf{I})C_f & 0 & \mathbf{I}+R_cC_f(\mathbf{J}\omega_{re}+j\omega^r\mathbf{I}) & -\mathbf{I}-R_cC_f(\mathbf{J}\omega_{re}+j\omega^r\mathbf{I}) \end{bmatrix} \begin{bmatrix} \vec{V}_s^r \\ \vec{I}_r^r \\ \vec{I}_s^r \\ \vec{I}_i^r \end{bmatrix} = \begin{bmatrix} 0 \\ 0 \\ \vec{V}_i^r \\ 0 \end{bmatrix} \tag{6.25}$$

Applying this theory to the filter-machine system in (6.12), the resulting set of equations are therefore given in (6.25), and harmonic frequency components in the rotor reference frame

can be determined. The resulting rotor current harmonics in the rotor reference frame for a 130 kW generating, 54,000 rpm, minimum flux linkage operating point, both without and with the three-phase LC filter, are shown in Fig. 6.7. The switching frequency in this simulation is 18 kHz.

The rotor speed and switching frequency for the simulation were chosen so that the switching frequency is an integral multiple of the fundamental electrical frequency (1.8 kHz), thus simplifying the computation of the harmonic spectrum. It can be seen that, with the exception of the 3^{rd} harmonic, the harmonics are decreased by the LC filter, significantly so at the higher harmonics. The reason for the increase in the 3^{rd} harmonic is its proximity to the resonance frequency created by the LC filter.

6.4.3 Rotor Loss Calculation

From the phasor analysis of the preceding section, the copper losses in the rotor can be calculated as follows by summing the losses due to each rotor reference frame harmonic:

$$P_r = \sum_n \frac{3}{2}[R_r]|\vec{I}_r^r[n]|^2 \tag{6.26}$$

From the preceding simulations, a rotor loss of 283 W is estimated without the LC filter. Introduction of the LC filter reduces the rotor losses to 59 W, or by roughly a factor of 5. It should be noted, however, that these losses are rough estimates, as they do not take into account effects such as the temperature and frequency dependence of the effective rotor resistance. Furthermore, it is worth repeating that rotor losses due to other effects, such as winding and tooth harmonics,

are not represented in this analysis. However, the above loss estimate can serve as a guide in the design of the LC filter.

6.5 Control of the Filter-Machine System

6.5.1 Model-based Controller

The additional dynamics of the LC filter can complicate a feedback control scheme, particularly when the fundamental frequency of operation is close to the resonance frequency of the converter. A model-based controller does not have these limitations, provided the natural dynamics of the system are benign. However, the presence of the LC filter requires modification of the model-based controller presented in Chapter 3 to compensate for the voltage drop and phase shift associated with the LC filter. The model-based feedforward controller was utilized to determine the appropriate command voltages applied to a synchronous reluctance machine with an electrically conducting rotor. It is a reasonable choice for systems which have slowly-varying speed, such as flywheel systems. From the model presented in Chapter 3, reasonably accurate feedforward voltage commands for a desired current $\vec{\tilde{i}}_s^r$ are given by

$$\vec{\tilde{v}}_s = R_s \vec{\tilde{i}}_s^r + \omega_{re} \mathbf{J} \left\{ L_{\ell s} \vec{\tilde{i}}_s^r + \vec{\tilde{\lambda}}_a^r \right\}, \tag{6.27}$$

$$\frac{d}{dt} \vec{\tilde{\lambda}}_a^r = - \left[\frac{R_r}{L_r} \right] \vec{\tilde{\lambda}}_a^r + \left[R_r \left(\frac{M}{L_r} \right)^2 \right] \vec{\tilde{i}}_s^r. \tag{6.28}$$

The model-based controller in this paper takes into account the induced rotor currents in a solid rotor of a synchronous reluctance machine. The block diagram of the controller is shown in Fig. 3.4. The peak current command i_{spk} comes from the outer bus voltage controller, and

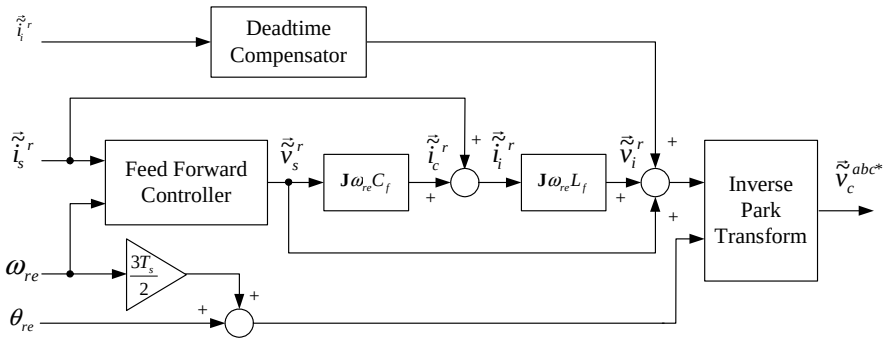

Fig. 6.9. Modification of feedforward controller to include LC filter and deadtime compensation

the parameter K_d determines the operating point (e.g., minimum current, minimum flux-linkage, maximum power factor) of the synchronous reluctance machine [41].

6.5.2 Compensation for LC Filter

When using an LC filter, the feedforward approach presented above must be modified to incorporate the additional voltages and currents associated with the LC filter. This is accomplished as follows:

$$\vec{\tilde{v}}_i^r = \vec{\tilde{v}}_\ell^r + \vec{\tilde{v}}_s^r \tag{6.29}$$

$$= \omega_{re} L_f \mathbf{J}\, \vec{\tilde{i}}_i^r + \vec{\tilde{v}}_s^r \tag{6.30}$$

$$= \omega_{re} L_f \mathbf{J} \left(\omega_{re} C_f \mathbf{J}\, \vec{\tilde{v}}_s^r + \vec{\tilde{i}}_s^r \right) + \vec{\tilde{v}}_s^r \tag{6.31}$$

A block diagram of the overall control system structure, including the LC filter compensator, is shown in Fig. 6.9. Also included in the diagram is dead-time compensation and a rotor position predictor based upon rotor speed, which are discussed in detail in Chapter 3.

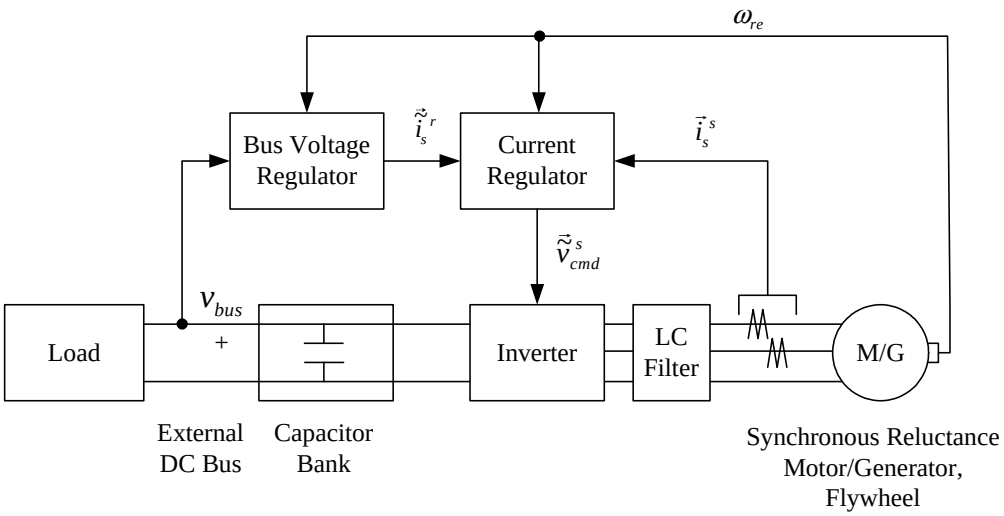

Fig. 6.10. Experimental setup of flywheel energy storage system with LC filter

6.5.3 Experimental Validation

Experimental results were generated on a 54,000 rpm, 120 kW synchronous reluctance drive which is part of a flywheel energy storage system manufactured by Pentadyne Power Corporation, capable of providing 120 kW of DC electrical power for up to 20 seconds [65]. The synchronous reluctance machine is driven by a 18 kHz-switching three-phase PWM inverter, and the control algorithm is implemented in a DSP processor. The system block diagram and a picture of the machine rotor/flywheel rim is shown in Figs. 3.17 and 6.10, respectively.

Fig. 6.11 shows the experimental result of the LC filter compensation. As expected, the current tracking error due to the addition of the LC filter is eliminated when properly compensated.

Inverter and stator phase currents associated with a 120 kW DC load at 48,000 rpm on the flywheel system are shown in Fig. 6.12. It can be seen that the current ripple from the switching harmonics is effectively removed. It has been clearly seen that the filtered stator currents reduced

the stator heating as well, and therefore the LC filter improves the overall thermal performance of the system quite successfully.

6.6 Conclusion

In this chapter, the design and control issues associated with the inclusion of a three-phase LC filter in a high-speed solid-rotor synchronous reluctance machine drive for time-harmonic rotor loss reduction have been discussed. A technique to estimate the rotor losses in the synchronous reluctance machine due to time harmonics associated with inverter switching has been presented, and it shows that a simple three-phase LC filter can reduce the rotor loss significantly. A modified model-based controller, which incorporates compensation for the LC filter, has been utilized experimentally, and has shown a successful result.

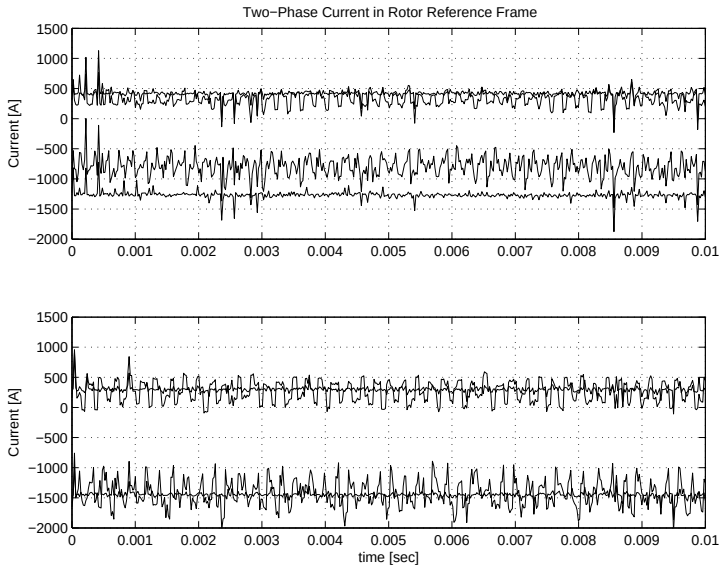

Fig. 6.11. Experiment: Rotor reference frame two-phase stator currents; 120kW generating, minimum flux linkage operating point. Top: Uncompensated direct- and quadrature-axis stator current and command. Bottom: Compensated direct- and quadrature-axis stator current and commands.

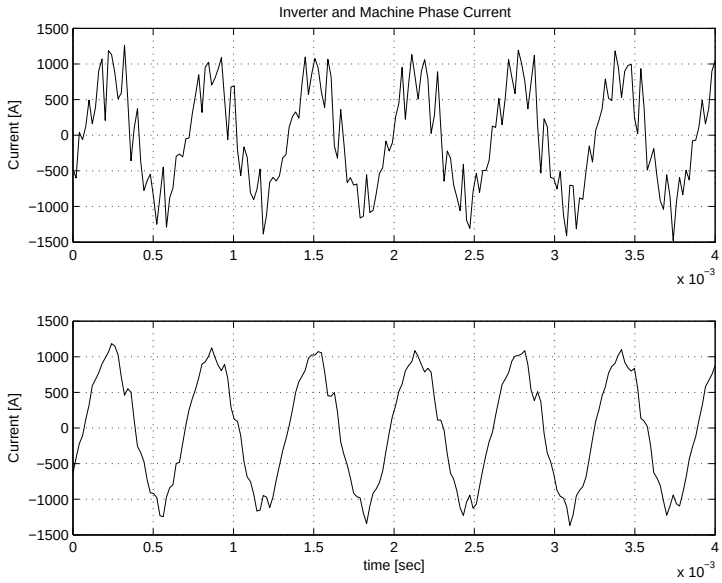

Fig. 6.12. Experiment: 120 kW DC load at 48,000 rpm on flywheel energy storage system with LC filter. Top: Inverter phase current. Bottom: Stator phase current

Chapter 7

Conclusions and Future Work

7.1 Conclusions

In this thesis, a control system for a high-speed solid-rotor synchronous reluctance flywheel motor/generator has been developed. A mathematical model for solid-rotor synchronous reluctance machines has been derived. Based on the suggested model, a model-based current regulator has been implemented and applied to a flywheel energy storage system. Also, practical difficulties such as nonlinear magnetics, rotor temperature variation, and inaccurate parameter measurement have been resolved. This chapter briefly summarizes the contributions.

- **Modeling and control considering rotor flux dynamics**

  Synchronous reluctance machines are an attractive choice for flywheel energy storage systems. A solid rotor can offer good structural properties for high-speed operation. However, eddy currents become non-negligible in the solid synchronous reluctance rotor, hence the resulting flux-linkage dynamics associated with a conducting rotor should be taken into account. Existing models cannot represent the solid-rotor synchronous reluctance machine well enough, especially during fast current transients. A model for solid-rotor synchronous reluctance machines has therefore been proposed. The model takes the rotor flux-linkage dynamics into consideration.

Based upon the proposed model, a current regulator is developed and implemented in a digital controller. It has been shown that the proposed model yields an improved performance for fast-changing torque command when compared to the conventional model. The current regulator based on the proposed model has been successfully applied to regulate the DC bus voltage of a flywheel energy storage system in conjunction with a feedback voltage controller.

- **Model improvement considering nonlinear magnetics**

  A model based on linear magnetic behavior is unable to represent the machine behavior for all operating conditions because the flux linkage in the machine is not linearly proportional to the exciting current amplitude in general. Nonlinear phenomena, such as magnetic saturation and remanent magnetization, cannot be disregarded. The proposed linear model has been modified in this chapter to incorporate the nonlinear flux linkage behavior, which appears as magnetic saturation and remanent magnetization.

  The modification of the linear model is especially beneficial for the model-based controller, where the output is synthesized based on the estimated flux linkage. The measurement of flux linkage/current relationship is only necessary for the suggested model modification. Although the machine under study did not show significant flux saturation, the proposed modification has been proven by compensating current tracking error caused by remanent magnetization in the rotor of the synchronous reluctance machine.

- **Feedback compensation for feedforward control**

  Although a sufficiently accurate model of the machine allow a feedforward controller, it relies heavily upon accurate knowledge of the parameters for good performance.

It is practically hard to measure all parameters exactly, and a feedforward-controlled system generates inaccurate output if the parameters are not correct. Therefore, it is necessary to have a way to take care of deviations such as inaccurate parameters, unmodeled dynamics, or disturbances.

A hybrid controller which incorporates a feedback PI compensator into a model-based feedforward controller to improve the performance and robustness of current regulation has been proposed. The machine current tracking error caused by the parameter mismatch has been mathematically analyzed, and stability analysis has also been performed. The proposed controller yields an improved performance for a fast-changing torque command with the model, as well as good tracking performance from the PI regulator.

- **Analysis and reduction of time harmonic loss using LC filter**

The eddy currents in a solid synchronous reluctance rotor generates heat in the rotor. This becomes an issue, especially to a flywheel energy storage device, because a magnetic-bearing-supported flywheel which is spinning in vacuum has a relatively poor heat transfer mechanism. The eddy currents generated by switching harmonics in the PWM stator voltage has been analyzed. A technique to estimate the rotor losses in the synchronous reluctance machine due to time harmonics associated with inverter switching has also been presented.

To minimize heat generated by the rotor eddy currents, and hence rotor conduction losses, a three-phase LC filter has been applied to the system. The modified model-based controller, which incorporates compensation for the LC filter, has also been suggested. Although the application of the LC filter is challenging due to the relatively low ratio

between the fundamental and switching frequencies in high-speed applications, it has been shown that a simple three-phase LC filter can reduce the rotor loss significantly.

7.2 Future Work

This thesis describes the theoretical and practical research for the control of solid-rotor synchronous reluctance motor/generator, which is utilized in a flywheel energy storage system. The following topics will be worth investigating in the future for more robust and efficient operation of the synchronous reluctance machine based flywheel system.

- **Sensorless control of the synchronous reluctance machine** [66–68]

  A synchronous reluctance machine drive requires the rotor position for starting and running. Although position sensors have issues such as cost and reliability, the flywheel energy storage system is generally controlled with a position sensor. However, it will be beneficial to have a way to control the machine without a position sensor for fault-tolerance and robustness. Based on the model derived for solid-rotor synchronous reluctance machine, a sensorless controller can be developed and applied to the system.

- **Optimal efficiency control for energy storage system** [69–72]

  It is vital to operate an energy storage device with optimal efficiency. Synchronous reluctance machines have a degree of freedom in the choice of current vector for a given torque, and the efficiency can be optimized by selecting different vector according to various conditions. A model-based approach to efficiency improvement for synchronous reluctance machine is viable if a reasonably accurate model has already been established.

References

[1] U.S. Department of Energy. Flywheel energy storage. *DOE/EE-0286*, Sep. 2003.

[2] H. Darrelmann. Comparison of high power short time flywheel storage systems. *INTELEC'99*, pages 6–9, June 1999.

[3] R. Dettmer. Spinning reserve [energy storage system]. *IEE Review*, 43(1):36–37, Jan. 1997.

[4] K. McLallin. The NASA flywheel battery project. *2004 NASA Environment and Energy Conference*, May 2004.

[5] P. P. Acarnley, B. C. Mecrow, J. S. Burdess, J. N. Fawcett, J. G. Kelly, and P. G. Dickinson. Design principles for a flywheel energy store for road vehicles. *IEEE Transactions on Industry Applications*, 32(6):1402–1408, Nov./Dec. 1996.

[6] Seok-Myeong Jang, Sang-Sub Jeong, Dong-Wan Ryu, and Sang-Kyu Choi;. Comparison of three types of PM brushless machines for an electro-mechanical battery. *IEEE Transactions on Magnetics*, 36(5):3540–3543, Sep. 2000.

[7] W. L. Niemeyer, P. Studer, J. A. Kirk, D. K. Anand, and R. B. Zmood. A high efficiency motor/generator for magnetically suspended flywheel energy storage system. *IECEC-89. Proceedings of the 24th Intersociety Energy Conversion Engineering Conference*, 3:1511–1516, Aug. 1989.

[8] D. Johnson, P. Pillay, and M. Malengret. High speed PM motor with hybrid magnetic bearing for kinetic energy storage. *Conference Record of the Industry Applications Conference of the 36th IAS Annual Meeting*, 1:57–63, 30 Sept.-4 Oct. 2001.

[9] B. Sneyer, D. W. Novotny, and T. A. Lipo. Field-weakening in buried permanent magnet AC motor drives. *IEEE Transactions on Industry Applications*, IA-21:398–407, Mar./Apr. 1985.

[10] S. Morimoto, M. Sanada, and Y. Takeda. Wide-speed operation of interior permanent magnet synchronous motors with high-performance current regulator. *IEEE Transactions on Industry Applications*, 30(4):920–926, July/Aug. 1994.

[11] B. K. Bose. A high-performance inverter-fed drive system of an interior permanent magnet synchronous machine. *IEEE Transactions on Industry Applications*, 24(6):987–997, Nov./Dec. 1988.

[12] Z. Q. Zhu and D. Howe. Halbach permanent magnet machines and applications: a review. *IEE Proceedings-Electric Power Applications*, 148(4):299–308, July 2001.

[13] Seok-Myeong Jang, Sang-Sub Jeong, Dong-Wan Ryu, and Sang-Kyu Choi. Design and analysis of high speed slotless PM machine with Halbach array. *IEEE Transactions on Magnetics*, 37(4):2827–2830, July 2001.

[14] M. Hippner and R. G. Harley. High speed synchronous homopolar and permanent magnet machines comparative study. *Conference Record of the 1992 IEEE Industry Applications Society Annual Meeting*, 1:74–78, 4-9 Oct. 1992.

[15] H. Devred, M. Martinez, and J. Huonic. 150 kVA, 56000 rpm, turbo engine integrated homopolar electrical generator. *International Conference of Electric Machines and Drives*, pages 749–751, 9-12 May 1999.

[16] P. Tsao, M. Senesky, and S. R. Sanders. An integrated flywheel energy storage system with homopolar inductor motor/generator and high-frequency drive. *IEEE Transactions on Industry Applications*, 39(6):1710–1725, Nov./Dec. 2003.

[17] B. D. Ingle and C. S. Corcoran. Development of a 1200-Hertz alternator and controls for space power systems. *NASA Technical Note*, NASA TM X-52453, 1968.

[18] Hua Bai, S.D. Pekarek, J. Tichenor, W. Eversman, D. J. Buening, G. R. Holbrook, M.L. Hull, R. J. Krefta, and S. J. Shields. Analytical derivation of a coupled-circuit model of a claw-pole alternator with concentrated stator windings. *IEEE Transactions on Energy Conversion*, 17(1):32–38, March 2002.

[19] N. A. Demerdash, R. Wang, and R. R. Secunde. Three dimensional magnetic fields in extra high speed modified lundell alternators computed by a combined vector-scalar magnetic potential finite element method. *IEEE Transactions on Energy Conversion*, 7(2):353–366, June 1992.

[20] C. Pollock and A. Michaelides. Switched reluctance drives: a comparative evaluation. *Power Engineering Journal*, 9(6):257–266, Dec. 1995.

[21] D. E. Cameron and J. H. Lang. The control of high-speed variable-reluctance generators in electric power systems. *IEEE Transactions on Industry Applications*, 29(6):1106–1109, Nov./Dec. 1993.

[22] R. M. Davis. A comparison of switched reluctance rotor structures. *IEEE Transactions on Industrial Electronics*, 35(4):524–529, Nov. 1988.

[23] T.J.E. Miller, A. Hutton, C. Cossar, and D.A. Staton. Design of a synchronous reluctance motor drive. *IEEE Transactions on Industry Applications*, 27(4):741–749, July/Aug. 1991.

[24] D. A. Staton, T. J. E. Miller, and S. E. Wood. Maximising the saliency ratio of the synchronous reluctance motor. *IEE Proceedings B Electric Power Applications*, 140(4):249–259, July 1993.

[25] A. Vagati, A. Fratta, G. Franceschini, and P. Rosso. AC motors for high-performance drives: a design-based comparison. *IEEE Transactions on Industry Applications*, 32(5):1211–1219, Sept./Oct. 1996.

[26] A. Chiba and T. Fukao. A closed-loop operation of super high-speed reluctance motor for quick torque response. *IEEE Transactions on Industry Applications*, 28(3):600–606, May/June 1992.

[27] H. Hofmann and S. R. Sanders. High speed synchronous reluctance machine with minimized rotor losses. *IEEE Transactions on Industry Applications*, 36(2):531–539, Mar./Apr. 2000.

[28] T. A. Lipo, A. Vagati, L. Malesani, and T. Fukao. Synchronous reluctance motors and drives-a new alternative. *26th IEEE-IAS meeting*, pages 425–431, Oct. 1992.

[29] H. Hofmann, S. R. Sanders, and A. El-Antably. Stator-flux-oriented vector control of synchronous reluctance machines with maximized efficiency. *IEEE Transactions on Industrial Electronics*, 51(5):1066–1072, Oct 2004.

[30] W. Leonhard. *Control of Electrical Drives*. Springer-Verlag, 1991.

[31] D. W. Novotny and T. A. Lipo. *Vector Control and Dynamics of AC Drives*. Oxford, 1996.

[32] B. K. Bose. *Power electronics and AC drives*. Prentice-Hall, 1986.

[33] B. K. Bose. *Power electronics and variable frequency drives: Technology and applications*. IEEE Press, 1997.

[34] D. N. Zmood, D. G. Holmes, and G. H. Bode. Frequency-domain analysis of three-phase linear current regulators. *IEEE Transactions on Industry Applications*, 37(2):601–610, March/April 2001.

[35] A. Vagati, M. Pastorelli, and G. Franceschini. High-performance control of synchronous reluctance motors. *IEEE Transactions on Industry Applications*, 33(4):983–991, July/Aug. 1997.

[36] R. E. Betz. Theoretical aspects of control of synchronous reluctance machines. *IEE Proceedings B - Electric Power Applications*, 139(4):355–364, July 1992.

[37] H. Nagase, Y. Matsusa, K. Ohnishi, H. Ninomiya, and T. Koike. High-performance induction motor drive system using a PWM inverter. *IEEE Transactions on Industry Applications*, 20:1482–1489, Nov./Dec. 1984.

[38] R. D. Lorenz and D. B. Lawson. Performance of feedforward current regulators for field oriented induction machine controllers. *IEEE Transactions on Industry Applications*, 23(4):142–150, Jan./Feb. 1987.

[39] A. Vagati, M. Pastorelli, and G. Franceschini. High-performance control of synchronous reluctance motors. *IEEE Transactions on Industry Applications*, 33(4):983–991, July/Aug. 1997.

[40] L. Xu, X. Xu., T. A. Lipo, and D. W. Novotny. Vector control of a synchronous reluctance motor including saturation and iron loss. *IEEE Transactions on Industry Applications*, 27(5):977–985, Sept./Oct. 1991.

[41] R. E. Betz, R. Lagerquist, M. Jovanovic, T. J. E. Miller, and R. H. Middleton. Control of synchronous reluctance machines. *IEEE Transactions on Industry Applications*, 29(6):1110–1122, Nov./Dec. 1993.

[42] L. Xu and J. Yao. A compensated vector control scheme of a synchronous reluctance motor including saturation and iron losses. *IEEE Transactions on Industry Applications*, 28(6):533–540, Nov./Dec. 1992.

[43] J. Melcher. *Continuum electromechanics*. MIT Press, 1981.

[44] C. T. Chen. *Linear system theory and design*. CBS College Publishing, 1984.

[45] R. S. Colby, A. K. Simlot, and M. A. Hallouda. Simplified model and corrective measures for induction motor instability caused by PWM inverter blanking time. *Recordings of the 21st Annual IEEE Power Electronics Specialists Conference*, pages 678–683, March/April 1990.

[46] B. H. Kenny, P. E. Kascak, R. Jansen, and T. Dever. A flywheel energy storage system demonstration for space applications. *Proceedings of the IEEE International Electric Machines and Drives Conference*, 2:1314–1320, 1-4 June 2003.

[47] M. C. Williams, R. S. Vogelsong, and K. S. Kundert. Simulation and modeling of nonlinear magnetics. *1995 IEEE International Symposium on Circuits and Systems, 1995. ISCAS '95.*, 1:736–739, 28 April - 3 May 1995.

[48] R. E. Betz, R. Lagerquist, M. Jovanovic, T. J. E. Miller, and R. H. Middleton. Control of synchronous reluctance machines. *IEEE Transactions on Industry Applications*, 29(6):1110–1122, Nov./Dec. 1993.

[49] L. Xu, X. Xu, T. A. Lipo, and D. W. Novotny. Vector control of a synchronous reluctance motor including saturation and iron loss. *IEEE Transactions on Industry Applications*, 27(5):977–985, Sept./Oct. 1991.

[50] L. Xu and J. Yao. A compensated vector control scheme of a synchronous reluctance motor including saturation and iron losses. *IEEE Transactions on Industry Applications*, 28(6):1330–1338, Nov./Dec. 1992.

[51] A. Vagati, M. Pastorelli, F. Scapino, and G. Franceschini. Impact of cross saturation in synchronous reluctance motors of the transverse-laminated type. *IEEE Transactions on Industry Applications*, 36(4):1039–1046, July/Aug. 2000.

[52] R. D. Lorenz and D. W. Novotny. Saturation effects in field-oriented induction machines. *IEEE Transactions on Industry Applications*, 26(2):283–289, Mar/Apr 1990.

[53] A. Vagati. The synchronous reluctance solution: a new alternative in AC drives. *20th International Conference on IECON '94*, 1:1–13, 5-9 Sept. 1994.

[54] C. Mademlis. Compensation of magnetic saturation in maximum torque to current vector controlled synchronous reluctance motor drive. *IEEE Transactions on Energy Conversion*, 18(3):379–385, Sept 2003.

[55] R. E. Betz, M. Jovanovic, R. Lagerqist, and T. J. E. Miller. Aspects of the control of synchronous reluctance machines including saturation and iron loss. *Conference Record of the 1992 IEEE Industry Applications Society Annual Meeting*, 1:456–463, Oct 1992.

[56] H. Hofmann. *High-speed synchronous reluctance machine for flywheel applications*. PhD thesis, University of California at Berkeley, 1998.

[57] T. Lubin, H. Razik, and A. Rezzoug. Magnetic saturation effects on the control of a synchronous reluctance machine. *IEEE Transactions on Energy Conversion*, 17(3):356–362, Sept. 2002.

[58] I. T. Wallace, D. W. Novotny, R. D. Lorenz, and D. M. Divan. Verification of enhanced dynamic torque per ampere capability in saturated induction machines. *IEEE Transactions on Industry Applications*, 30(5):1193–1201, Sept./Oct. 1994.

[59] J. Steinke. Use of the LC filter to achieve a motor-friendly performance of the PWM voltage source inverter. *IEEE Transactions of Energy Conversion*, 14(3):649–654, Sept. 1999.

[60] Y. Murai, T. Kubota, and Y. Kawase. Leakage current reduction for a high-frequency carrier inverter feeding an induction motor. *IEEE Transaction on Industry Applications*, 28(4):858–863, Jul./Aug. 1992.

[61] S. Ogasawara and H. Akagi. Modeling and damping of high-frequency leakage currents in PWM inverter-fed AC motor drive systems. *IEEE IAS Conference Recordings*, pages 29–36, 1995.

[62] W. Santiago. Inverter output filter effect on PWM motor drives of a flywheel energy storage system. *Second International Energy Conversion Engineering Conference*, NASA/TM-2004-213301(6):533–540, 16-19 Aug. 2004.

[63] Jih-Sheng Lai and Fang Zheng Peng. Multilevel converters-a new breed of power converters. *IEEE Transactions of Industry Applications*, 32(3):509–517, May/June 1996.

[64] B. P. McGrath, D. G. Homes, and T. Meynard. Reduced PWM harmonic distortion for multilevel inverters operating over a wide modulation range. *IEEE Transactions of Power Electronics*, 21(4):941–949, July 2006.

[65] J. Park, C. Khalizadeh, and H. Hofmann. Feedforward control of high-speed solid-rotor synchronous reluctance machines with rotor dynamics model. *Conference Record of the Industry Applications Conference of the 39th IAS Annual Meeting*, Oct 2004.

[66] S. Bolognani. A torque angle calculator for sensorless reluctance motor drives. *EPE'91*, 4:13–17, 1991.

[67] R. Lagerquist, I. Boldea, and T. J. E. Miller. Sensorless control of the synchronous reluctance motor. *IEEE Transactions on Industrial Applications*, 30(3):673–682, May/June 1994.

[68] M. S. Arefeen, M. Ehsani, and T. A. Lipo. Sensorless position measurement in synchronous reluctance motor. *IEEE Transactions on Power Electronics*, 9(6):624–630, Nov. 1994.

[69] F. Fernández-Bernal, A. García-Cerrada, and R. Faure. Model-based loss minimization for DC and AC vetor-controlled motors including core saturation. *IEEE Transactions on Industry Applications*, 36(3):755–763, May/June 2000.

[70] D. Kirschen, D. W. Novotny, and T. A. Lipo. On-line efficiency optimization of a variable frequency induction motor drive. *IEEE Transactions on Industry Applications*, 21(4):610–616, May/June 1985.

[71] F. Abrahamsen, F. Blaabjerg, J. Pedersen, and P. Thoegersen. Efficiency-optimized control of medium-size induction motor drives. *IEEE Transactions on Industry Applications*, 37(6):1761–1767, Nov./Dec. 2001.

[72] T. Matsuo, A. El-Antably, and T. A. Lipo. A new control strategy for optimum-efficiency operation of a synchronous reluctance motor. *IEEE Transactions on Industry Applications*, 33(5):1146–11153, Sep./Oct. 1997.

[73] R. Hebner, J. Beno, and A. Walls. Flywheel batteries come around again. *IEEE Spectrum*, 39(4):46 – 51, April 2002.

[74] J. G. Bitterly. Flywheel technology: past, present, and 21^{st} century projections. *IEEE Aerospace and Electronic Systems Magazine*, 13(8):13–16, Aug. 1998.

[75] I. Boldea. *Reluctance synchronous machines and drives*. Oxford, 1996.

[76] C. R. Sullivan and S. R. Sanders. Models for induction machines with magnetic saturation of the main flux path. *IEEE Transactions on Industry Applications*, 31(4):907–917, July/August 1995.

[77] T. Matsuo and T.A. Lipo. Field-oriented control of synchronous reluctance machine. *24th Annual IEEE Power Electronics Specialists Conference Record (PESC)*, pages 425–431, June 1993.

[78] J. I. Ha, S. J. Kang, and S. K. Sul. Position-controlled synchronous reluctance motor without rotational transducer. *IEEE Transactions on Industry Applications*, 35(6):1393–1398, Nov./Dec. 1999.

[79] X. Xu, R. W. DeDoncker, and D. W. Novotny. A stator flux oriented induction motor drive. *IEEE PESC Conference Recordings*, 2:870–876, 11-14 April 1988.

[80] G. F. Franklin, J. D. Powell, and A. Emami-Naeini. *Feedback control of dynamic systems, 3^{rd} Ed.* Addison-Wesley, 1994.

[81] H. Hofmann, R. Stroman, and M. Lanagan. Closed-form frequency model of 3-phase inverter drive for DC distribution system analysis. *SAE World Congress 2002*, pages 531–539, Jan 2002.

[82] S. Chen and G. Joos. Transient performance of UPS system with synchronous-frame digital controller. *22nd International Telecommunications Energy Conference (INTELEC)*, pages 1007–1017, 10-14 Sept. 2000.

[83] Y. Sozer, D. Torrey, and S. Reva. New inverter output filter topology for PWM motor drives. *IEEE Transactions on Power Electronics*, 15(6):1007–1017, Nov. 2000.

[84] J. Proakis and D. Manolakis. *Digital signal processing 3^{rd} Ed.* Prentice-Hall, 1996.

[85] J. Fletcher, B. Williams, and T. Green. Efficiency aspects of vector control applied to synchronous reluctance motors. *Thirtieth IAS Annual Meeting, IAS '95*, 1:294–300, 8-12 Oct. 1995.

Vita

Jae-Do Park was born in Seoul, Korea on November 30, 1967. He received the B.S. and M.S. degree in Electrical Engineering from the Hanyang University in Seoul, Korea in 1992 and 1994, respectively. He started his professional career by joining in the R&D Center of the LG Industrial Systems, Anyang, Korea. He had worked for eight years as a research engineer, developing induction machine drive systems such as high-speed elevators drives and general purpose inverters. His work includes subsystems as well as the main drives, such as add-on controllers and communication boards. In 2001, he enrolled in the Ph.D. program in electrical engineering at the Pennsylvania State University. He has participated in various projects such as inverter controller design, smart material actuator and energy harvesting device research. He also has supervised lab sessions for the electric machinery and drives class, EE497D. Since late 2004, he has been employed by the Pentadyne Power Corporation in Chatsworth, California as controls software engineer. He currently takes charge of the control algorithm design and software development for the flywheel energy storage system.